Doctoral Dissertation

High-temperature reliability of ultrasonic bonded metal ribbon wirings for power electronic devices

Semin Park

July 2015

Department of Adaptive Machine System
Graduate School of Engineering
Osaka University

Ph.D. Dissertation

High-temperature reliability of ultrasonic bonded metal ribbon wirings for power electronic devices

by

Semin Park

Department of Adaptive Machine System

Graduate School of Engineering

Osaka University

July 2015

Approved by

Professor Katsuaki Suganuma

Professor Yoritoshi Minamino

Professor Keisuke Uenishi

Except where reference is made to the work of others, the work described in this dissertation is my own or was done in collaboration with my advisory committee. This dissertation includes my own published or submitted articles information.

High-temperature reliability of ultrasonic bonded metal ribbon wirings for power electronic devices

Abstract

Metal string wire bonding technology has been widely used in Si semiconductor electronic devices for many decades because of their excellent formability and rapid process. However, the emerging post-Si wide-bandgap semiconductors like SiC or GaN target operated at higher temperatures over 200 °C have been arising, and thus the thermal stability of wiring has become one of critical issues in power electronics packaging. At such a high temperature, the wirings may severely degrade due to grain coarsening, heel cracking resulting in final failure. This thesis describes the potentials of joint reliability for new wiring structures such as Al ribbon and Cu/Al clad ribbon.

At first, a large rectangular 4N Al ribbon (1500 × 200 μm^2) was applied in wiring structure instead of typical string wires ($d \leq 400$ μm) to secure the high temperature degradation. Use of the ribbons is expected to improve the high temperature degradation as the large area bonding. The ribbon bonding by ultrasonic consolidation was performed at ambient temperature without any heating. High ultrasonic power/frequency, high bonding pressure, and long bonding time are required to get successful ribbon bonding. Therefore, the optimization of ultrasonic ribbon bonding process was preceded to obtain the steady bond interfaces. The suitable bonding parameters were determined by evaluation of the tensile strength. Ultrasonic ribbon bonding mechanisms are investigated.

Next, a Cu/Al clad ribbon was adopted to achieve better thermal/electrical performance together with easy manufacturing. The use of Cu ribbon instead of Al is expected to improve the mechanical degradation at high temperature, though Cu ribbons have inherent difficulties in the ultrasonic bonding process because of the high acoustic impedance and the high hardness. The thermo-mechanical stability of Al have compared to Cu/Al clad ribbons in a practical interconnect bonding structure under harsh environmental tests such as thermal exposure to 200 °C and thermal shock cycling at -40/250 °C. By the optimizing the ultrasonic ribbon bonding parameters, Cu/Al clad ribbons showed higher stability than Al ribbons. Hence, the thermal and mechanical stability of the ribbon wiring structure consist of a Cu/Al clad ribbon is superior to those of Al.

Finally, the mechanism of a failure of Cu/Al clad ribbon was investigated with respective to heel crack propagation. The microstructural evolution was analyzed to understand the mechanical degradation due to grain coarsening. Dynamic recrystallization (DRX) occurred during the high-temperature deformation both of Cu and of Al, for which the mechanism involves both discontinuous dynamic recrystallization (DDRX, i.e., nucleation and grain growth) and continuous dynamic recrystallization (CDRX, i.e., transformation of sub-grains into grains). Sub-grains were formed within the recrystallized grains during harsh tests. Subsequently, dynamic grain coarsening was observed in CDRX with increasing harsh test periods. Heel cracks were frequently formed at boundaries between the bonded zone and non-bonded zone even in the ultrasonic ribbon bonding process. During the harsh tests, the heel cracks propagated deep into the Al layer along recrystallized grain boundaries.

In the thesis, the results confirmed that ribbon bonding technology would contribute to establish a long-term interconnection reliability for high-temperature power electronics packaging.

Table of contents

List of tables

List of figures

Abbreviations

WBG	Wide-bandgap	T	Transmission coefficient
SBD	Schottky barrier diode	W	Ultrasonic power
MOSFET	Metal oxide semiconductor field effect transistor	s	Bonding time
E_g	Bandgap	N	Normal bonding force
n_i	Intrinsic carrier density	kHz	Ultrasonic frequency
ε_r	Relative permittivity	d	Average grain size
μ_n	Electron mobility	DRX	Dynamic recrystallization
E_c	Dielectric constant (Breakdown voltage)	DDRX	Discontinuous dynamic recrystallization
υ_{sat}	Electron saturation velocity	CDRX	Continuous dynamic recrystallization
λ	Thermal conductivity	CI	Confidence index
T_j	Junction temperature	PF	Pole figure
CTE	Coefficient of thermal expansion	ODF	Orientation distribution function
EFO	Electronic-flame-off	$\{\varphi_1, \phi, \varphi_2\}$	Bunge Euler angles
FAB	Free air ball	RD	Rolling direction
IC	Inside chamfer	TD	Transverse direction
IR	Inside radius	ND	Normal direction
F	Pull force	IQ	Image quality
ϕ	Pull angle	θ	Misorientation angle
ENIG	Electroless nickel immersion gold	LAGB	Low-angle grain boundary
IMC	Intermetallic compound	HAGB	High-angle grain boundary
Z	Acoustic impedance	BC	Band contrast
V	Ultrasound velocity	GOS	Grain orientation spread
ρ	Density	KAM	Kernel average misorientation
R	Reflection coefficient	IPF	Inverse pole figure

Chapter 1

Introduction

1.1 Background

1.1.1 Next-generation wide-bandgap power electronic devices

Nowadays, next-generation wide-bandgap (WBG) semiconductors such as silicon carbide (SiC) and gallium nitride (GaN) have been selected as the chip materials for high-power electronic devices to replace conventional silicon (Si). Some of the intrinsic material properties of WBG semiconductors are listed in **Table 1.1**.

The WBG power electronic devices applied to schottky barrier diode (SBD), insulated gate bipolar transistor (IGBT), and metal oxide semiconductor field effect transistor (MOSFET) can be operated in the conditions of higher temperatures, higher current flows, and higher breakdown voltages [1–3]. The application of WBG power devices can also reduce substantial power losses compared to Si power devices.

Table 1.1 Physical semiconductor properties for power electronic devices [4–6]

Material	E_g (eV)	n_i (cm^{-3})	ε_r	μ_n ($cm^2/V\,s$)	E_c (MV/cm)	υ_{sat} (10^7cm/s)	λ (W/cm K)
Si	1.1	1.5×10^{-10}	11.8	1350	0.3	1.0	1.5
SiC	3.26	8.2×10^{-9}	10	720	2.0	2.0	4.5
GaN	3.39	1.9×10^{-10}	9.5	900	3.3	2.5	1.3
Diamond	5.45	1.6×10^{-27}	5.5	1900	5.6	2.7	20

1.1.2 Problem definition and research trend

Applying the WBG semiconductor devices may cause high-temperature joint failures due to increasing the junction temperature (T_j). Hence, innovative packaging solutions such as new interconnect materials and structures are needed to secure the joint stability at high operating temperature.

The typical operating temperature and component life requirements for high power electronics applications have been published by Chin *et al*. and Buttay *et al.* [7, 8]. For Si power electronic modules, the maximal junction temperature (T_{jmax}) is lower than 175 ℃ and the temperature variation becomes 200 degree, as shown in **Fig. 1.1**. Since packaging component of WBG semiconductors can undergo T_{jmax} higher than 200 ℃ and thermal cycles with ΔT > 250 degree, reliability problems become one of the serious issues. At such a high temperature, the thin string metal wirings easily show severe mechanical degradation due to grain coarsening and heel cracks formation resulting in final device failure. Thus, some new wiring structure with a stable function even was subjected to harsh thermal environment.

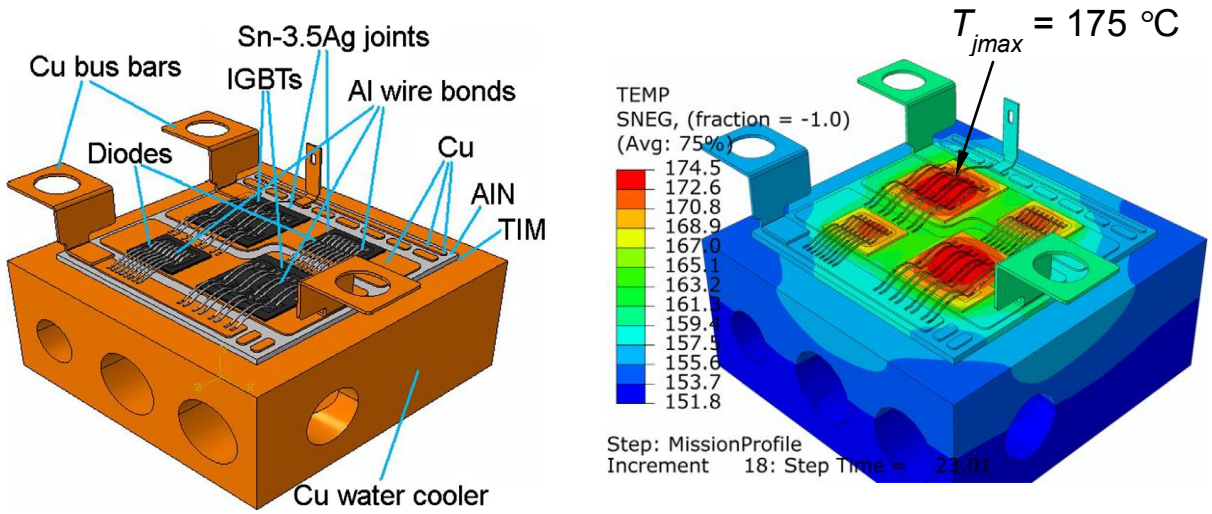

Fig. 1.1 Half-bridge power switches constructed with two IGBTs and two diodes on an AlN-based substrate and an integrated base-plate cooler. The simulated hottest temperature field in the half bridge switch module during the mission profile for a specific thermal resistance of 5 K mm^2 W^{-1} between the substrate and the cooler and a heat exchange coefficient of 15,000 Wm^{-2} k^{-1} applied at the inner wall of the cooler [9].

4N Al wire bonding made by ultrasonic bonding, carrying electrical current between a chip and a substrate, is a typical interconnection technology used in power electronics packages. The increasing power density causes high temperature and stress on devices resulting in early failure [10]. Connection damage stems from both chip self-heating and Joule self-heating caused by high current density crossing

the wire (typically 10 A per 250 μm Al wire diameter [11]). Furthermore, cracks initiate during the bonding process, and propagate during the device operation [12]. The two most frequent failure modes are interfacial cracking (lift-off) and heel cracking (high operating temperatures/currents). The former one is mainly due to the bad bonding condition and coefficient of thermal expansion (CTE) mismatch between silicon and Al wire (α_{Si} = 2.6 ppm K^{-1}, α_{Al} = 23.8 ppm K^{-1} [13]). Under high-temperature operation, accumulated stresses occur at the interface, leading to the degradation [14]. The later one is mainly due to Al grain coarsening under heat transfer through wirings. **Fig. 1.2** shows the two failure modes of wire involving fatigue at the heel area.

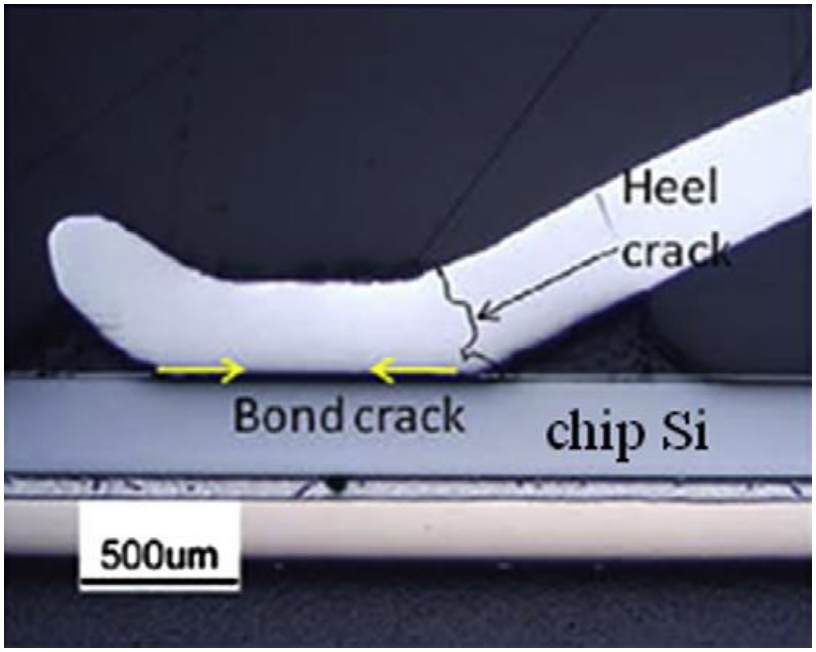

Fig. 1.2 Lift-off and heel crack mechanism of a wire bonding [15].

1.2 Ultrasonic wire bonding

Wire bonding using ultrasonic energy with pressure is one of solid-state joining processes. The ultrasonic energy with pressure induces friction between the mating surfaces to achieve tight metal joints. Ultrasonic bonding has inherent advantages derived from its solid-state bonding characteristics, and has been in use as a versatile joining method in automotive, train, aerospace, power plant, and green and renewable energy industries for several decades to produce the similar or dissimilar materials joints, where the materials are metal sheets [16, 17], thin foils [18], semiconductors [19], ceramics [20], plastics [21], and glasses [22], as shown in **Fig. 1.3**.

Fig. 1.3 Applications of power electronic devices module using ultrasonic wire bonding technology

1.3 Typical wire bonding technology

Metal wire bonding technology using based on heat, pressure, and ultrasonic energy has been generally applied in electronics packaging [23–28]. The process of connecting chips to substrates or lead

frames can be accomplished by metal wirings. The wire bonding techniques consist of ball bonding and wedge bonding. Those bonding methods are used by varying of thermo-sonic, thermo-compression, and ultrasonic. A ball bonding method has higher possession for microelectronic semiconductor packages manufacturing compared to wedge bonding method [29, 30].

1.3.1 Ball bonding

In this technique, a wire is passed through a hollow capillary, and an electronic-flame-off (EFO) system is used to melt a small portion of the wire extending beneath the capillary [31]. The surface tension of the molten metal at a ball, as the wire material solidifies. The ball is pressed to a bonding pad on a die with sufficient force to cause plastic deformation and atomic interdiffusion between the wire and the pad metallization. The plastic deformation and atomic interdiffusion ensure the intimate contact between the two metal surfaces and form the first bond (ball bond). The capillary is then raised and repositioned over the second bond site on the substrate; a precisely shaped wire connection called a wire loop is thus created as the wiring direction. Deforming the wire against the bonding pad makes the second bond (wedge bond or stitch bond), having a crescent or fishtail shape made by the imprint of the capillary's outer geometry. Then the wire clamp is closed, and the capillary ascends once again, breaking the wire just above the wedge, an exact wire length is left for EFO to form a new ball to begin the next bonding. Ball bonding is generally used in thermo-compression or thermos-sonic bonding process. This technique requires a high temperature ranging from 100 to 500 ℃ depending on bonding process. Heat is generated during the manufacturing process either by a heated capillary feeding the wire or by a heated pedestal on which the assembly is placed or by both depending on the bonding purpose and materials. Relatively small Au wire (diameter < 75 μm) is mostly used in this technique because of its easy deformation under pressure at elevated temperature, its resistance to oxide formation, and its ball formability during a flame-off or electronic discharge cutting process. The ball bonding is generally used in the application where a pad pitch is greater than 100 μm.

Prior to bonding, the wire are pre-heated by the bonder heat-stage to make a ball at the wire tip, which aids the welding process. The prior ball bonding process is illustrated in **Fig. 1.4**. The ball formation at the wire tip is melted by the spark that is produced from an electrode. The ball is rapidly solidifies and the free air ball (FAB) consists of large grains after melting, as shown in **Fig. 1.5**. A wire clamp is open to bonding on a bond pad and then bond is formed by ultrasonic vibration. The ball bonding process has an advantage of rapid bonding process but heating procedure in the ball formation causes of damage wire metals and package devices, it can be not applied to thick wire bonding above several hundreds of μm. To solve this problem, recently a wedge shape tool without heating procedure has attracted much attention. This will be discussed in detail at the following chapters.

Capillary bonding tool is made from ceramic, tungsten or ruby materials. The most common material for capillaries is high density fine grain alumina ceramic because of its excellent wear resistance, high oxidation resistance and easy cleaning. A polish finish produces a shiny bond, being used when there is good bondability, whereas a matte finish produces a textured stitch bond, being used for poor bondability. The capillaries are typically 1.585 mm in diameter and 11.1 mm long. They have a large entry hole at the top and then the hole tapers down to a small hole diameter typically between 38-50 μm, depending upon the wire diameter used and the application. At the exit of the small hole, there is normally an inside chamfer (IC) or inside radius (IR). The IC is designed to seat the ball in the tool and to provide good downward force. A 120° chamfer is designed for poor bondable surfaces by providing more downward force. The disadvantage is that it puts more drag on the wire. A 90° chamfer is designed for bondable surfaces giving equal downward and holding forces. There is relatively little drag. The double inside chamfer capillary was introduced to combine the qualities of the 90° and 120° tools. Recently, 70° chamfer is also used for special small ball, fine pitch applications.

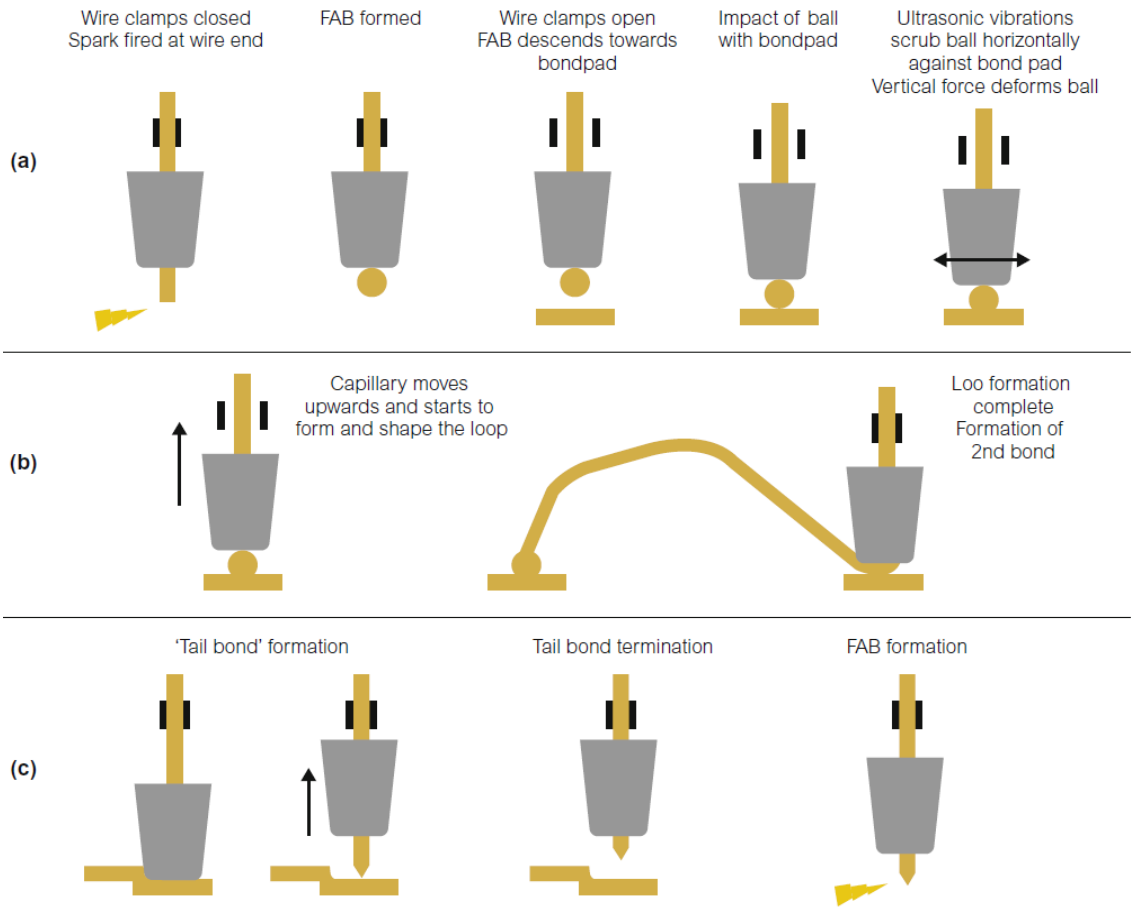

Fig. 1.4 Schematic of the ball wire bonding process (a) from left to right, formation of the end of a wire into a free air ball (FAB), the ball descends to the bond pad, ball impacts the bond pad and ultrasonic vibrations scrub the ball in a shearing action against the pad while simultaneously applying a downward force to deform the ball (b) capillary ascending to start formation of the loop followed start of 2nd bond formation (c) 2nd bond formation and start of tail formation by tensile deformation od the wire, tail bond termination formation of FAB and beginning of new cycle [31].

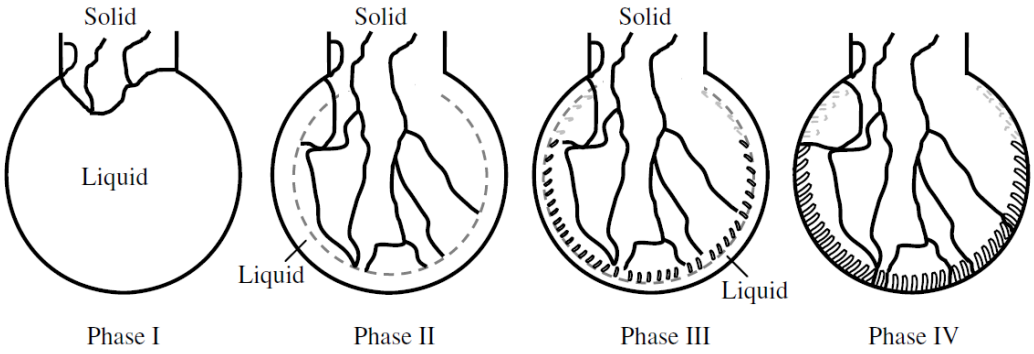

Fig. 1.5 Schematic showing the evolution of solidification process in the Cu FAB [32].

1.3.2 Wedge bonding

Wedge bonding is named based on the shape of its bonding tool [33–39]. In this technique, the wire is fed at an angle usually 30-60° from the horizontal bonding surface through a hole in the back of a bonding wedge. Normally, forward bonding is preferred, i.e. the first bond is made onto a die and the second is made onto a substrate. By descending the wedge onto an IC bond pad, the wire is pinned onto the pad surface and an ultrasonic or thermo-sonic bonding is performed. Next, the wedge rises and executes a motion to create a desired wire loop shape. At the second bond location, the wedge descends, making a second bond. During the loop formation, the movement of the axis of the bonding wedge feed hole must be aligned with the center line of the first bond, so that the wire can be fed freely through the hole in the wedge.

Wedge bonding can be used for both Al wire and Cu wire, and Au wire. The wedge bonding is performed by an ultrasonic energy with tool pressure at ambient temperature. One of the advantages of the wedge bonding is that it can form to very small dimensions compare to large ball bonding, down to the pitch size of 50 μm. However, the factors based on machine rotational movements make the overall speed of the process less than thermo-sonic ball bonding. Al ultrasonic bonding is the most common wedge bonding process because of low cost and the low working temperature. The main advantage for Au wire wedge bonding is the possibility to avoid the need of hermetic packaging after bonding due to the inert properties. In addition, a wedge bond will give a smaller footprint than a ball bond, which specially benefits the microwave devices with small pads that require an Au wire junction.

Low angle ~30° wire feed style gives best placement control and tail consistency under the bond foot. High angle ~60° is only used from the requirement for high package walls or other tall devices in the bonding vicinity. In the case of high angle wire feed, process reproducibility of wirings is less consistent due to the steep feed angle and the action of clamps. This gives the system a limitation on its access for pads close to high walled packages. Foot profile of the wedge can be either flat or concave. Most of the automatic Al wire applications use concave foot to reduce wire positioning errors. The flat foot is mainly

used for Au wire, or for Al wire, to obtain extremely short bonds. For Al wire, the wedge is usually made of tungsten carbide (WC) or ceramic. The ceramic wedges are relatively new and provide improved quality and tool life, although the price is high. For Au wire, the material used is WC as the Au leaches out the Co binder in the WC wedge. The life of W will be greatly shorter.

The parameters of the wedge greatly affect the wire bond characteristics. For the first bond, pull strength is affected by back radius, bond location is influenced by hole size, tail length is controlled by hole shape and surface quality. The main wedge parameters that affect looping are hole size and shape, as well as feed angle. For the second bond, pull strength is defined mainly by front radius and bond length, and tail consistency is affected by back radius.

1.3.3 Wire materials

Au and Ag are the commonly used as thin wire materials of microelectronic packaging, whereas Al and Cu are used in thick wire materials of power electronic devices.

Au and Ag wires are usually processed by thermo-compression bonding and by thermo-sonic bonding. In producing such the bonding wires, surface finish and surface cleanliness are two of the critical issues to ensure the formation of a strong bond and to prevent clogging of bonding capillaries. Pure Au and Ag can usually be drawn to achieve an adequate breaking strength (ultimate tensile strength of wires) and proper elongation.

Pure Al is typically too soft to be drawn into a fine wire. Therefore, Al is often alloyed with 1 mass% Si or 1 mass% Mg to provide enough strength. At room temperature, 1 mass% Si exceeds the solubility of Si in Al by a factor of 50, which leads to Si precipitation. The number and the size of Si precipitates are dependent on cooling rate from bonding temperature. A slower cooling rate results more precipitation and large inhomogeneous Si nodules, while a faster cooling rate does not allow sufficient time for Si precipitation resulting in the formation of uniformly dispersed nodules. Si grain size can affect wire ductility. In contrast, the second phase formation can become a potential nucleation site for fatigue cracks.

Al alloyed with 1 mass% Mg can be drawn into a fine wire that exhibits a breaking strength similar to that of Al-1%Si. The Al-1%Mg alloy wire forms sound bonds and is superior to Al-1%Si with good resistances both to fatigue failure and to degradation of ultimate strength after exposure to elevated temperatures. These advantages of Al-1%Mg wire occur because the equilibrium solid solubility of Mg in Al is about 2 mass% by weight, and thus at 0.5-1%Mg there is no tendency significant second-phase formation as is the case for Al-1%Si.

Recently, Cu wire bonding has received considerable attention because of their cheapness and their excellent stiffness to resist sweeping during plastic encapsulation. The major problem for this system is the bondability. Cu wire bonding is difficult to manufacturing the wirings because Cu is harder than Al. Therefore a harder metallization or wire coating is required. In addition, the Cu ball bonding must be performed in an inert atmosphere as the oxidation readily.

1.3.4 Metallurgical system at wire bond interface

In wire bonding process, different pad metallization are used, depending on the production requirements. Different metallurgical systems can lead to different reliability behaviors. In the present thesis, the metallurgical systems of Au-Al, Cu-Al, and Al-Ni were investigated.

A. Au-Al system

The Au-Al joining system is the most commonly used in wire bonding process [40−45]. However, this bonding system can easily lead to the formation of Au-Al intermetallic compounds with associated Kirkendall voids. These formations can be accelerated with temperature in service. Five intermetallic compounds can be formed between Au and Al in the reaction, which are all colored: Au_8Al_3 (tan), Au_4Al (tan), Au_2Al (metallic gray), AuAl (white), and $AuAl_2$ (deep purple). $AuAl_2$ can be initially formed during bonding process even at room temperature and is transformed to other Au-Al compounds depending on temperature, time and bonding configurations. The Au-Al interface consists of two regions, labeled A

(without Au-Al IMCs) and B (with IMCs), as shows in **Figs. 1.6a**. Region A presents as an approximately 4 nm thick uniform layer between the metals (**Figs. 1.6b**), whose main constituents are aluminum and oxygen (bottom table of **Figs. 1.6**), consistent with the preservation of the amorphous alumina film, that limits interdiffusion and retards the formation of IMCs [40]. When annealed at 175 ℃ for 5 h, IMC layers form between the Au ball and the Al pad, as shows in **Figs. 1.7a**. STEM-EDX of the interface found that near the Al pad an aluminum-rich alloy IMC-1 exists; near the Au ball is found a gold-rich alloy IMC-3; and the latively thick mid-layer IMC-2 is also present (bottom table of **Figs. 1.7**). In addition, there was a region of relatively light contrast, between IMC-2 and IMC-3, confirmed as alumina.

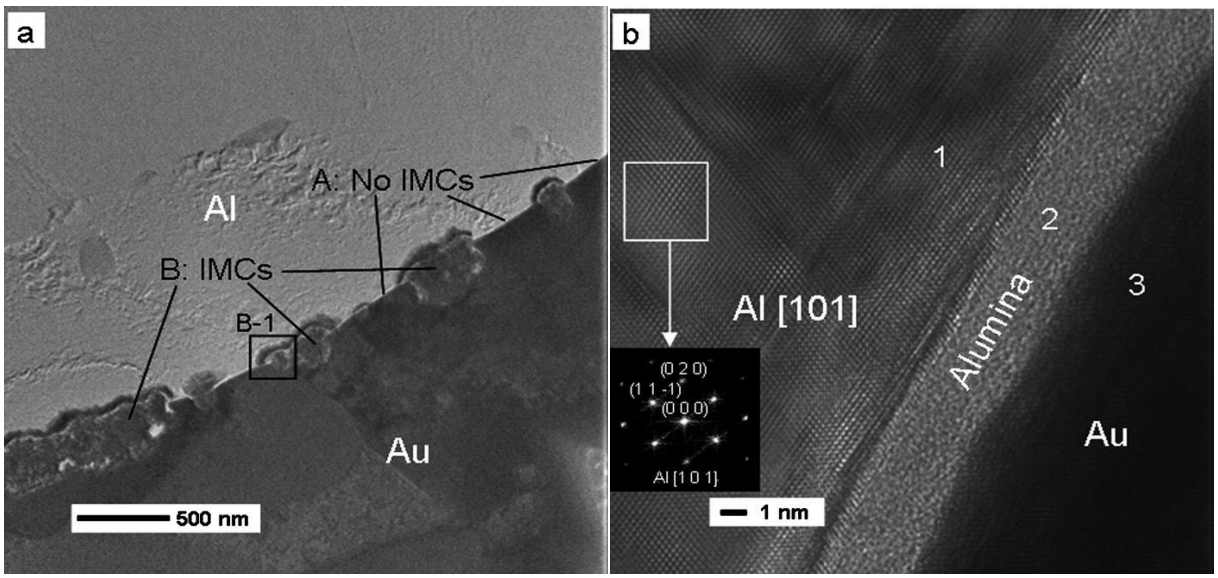

Region	O *K* at.%	Al *K* at.%	Au *L* at.%
1	5	94	1
2	53	45	2
3	2	9	89

Fig. 1.6 (a) Bright field TEM image of the Au–Al interface in the as-bonded state. (b) Details of an A region shows a uniform layer of amorphous alumina remained after ultrasonic bonding, demonstrating lower power thermos-sonic treatment could not completely disrupt the oxide overlayer [40].

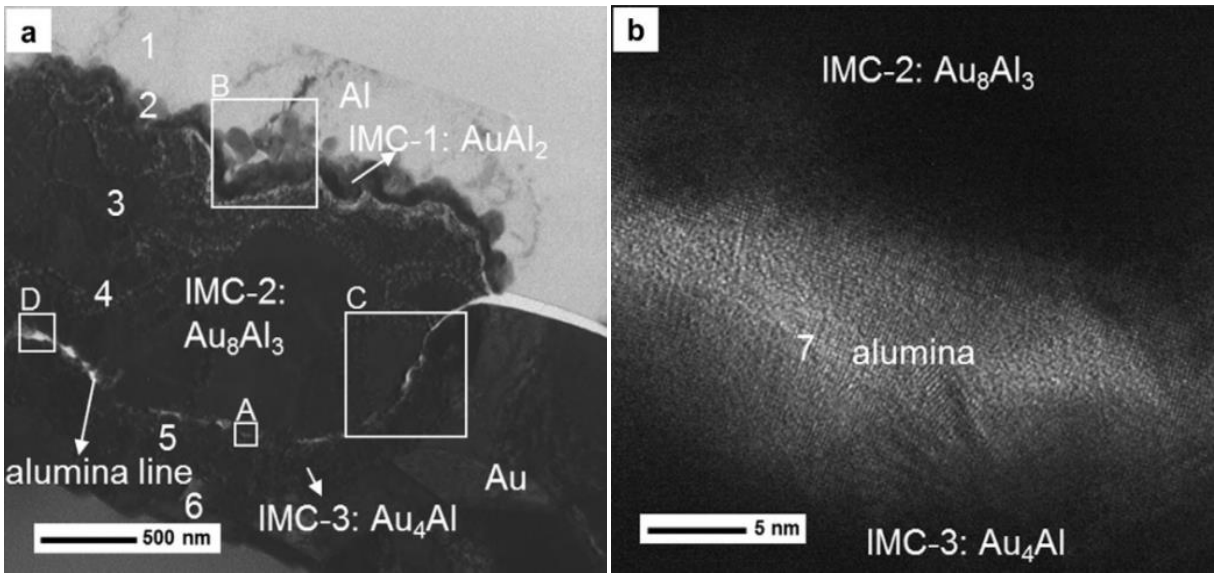

Region	O *K* at.%	Al *K* at.%	Au *L* at.%
1	5	94	1
2	9	63	28
3	12	27	61
4	13	24	63
5	12	18	80
6	5	8	87
7	41	40	19
8	2	89	9

Fig. 1.7 (a) TEM image of Au/Al bond annealed at 175 ℃ for 100 h having only Au_4Al and Au_8Al_3 between Au and SiO2; (b) SAED from a grain indicated by a line in (a) confirms the Au_8Al_3 structure in a [210] zone axis; (c) SAED from a grain indicated by a line in (a) confirms the Au_4Al structure in a [111] zone axis [45].

B. Cu-Al system

Cu wire can be bonded to both Au and Al electrodes. Au-Cu system has been discussed before by many researchers **[**46–49]. For the Cu-Al system, there exist five intermetallic compounds favoring the Cu-rich side. Thus, there are various intermetallic failures similar to those of the Au-Al system. However, intermetallic growth in a Cu-Al bond is slower than in an Au-Al bond. The intermetallic growth in Cu-Al bond does not result in Kirkendall voiding lowers the shear strength at 150-200 ℃ due to the growth of

the brittle $CuAl_2$ phase, as shown in **Fig. 1.8**. In a temperature range 300-500 ℃, bond strength significantly decreases with the increase of the total intermetallic thickness. The rate of Cu-Al intermetallic formation depends on the ambient temperatures. Cu oxide of Cu-Al bond system inhibits the growth of some voids at the interfaces [46]. However, the presence of Cl contamination and water can cause corrosion of an Al metallization containing Cu-Al intermetallics.

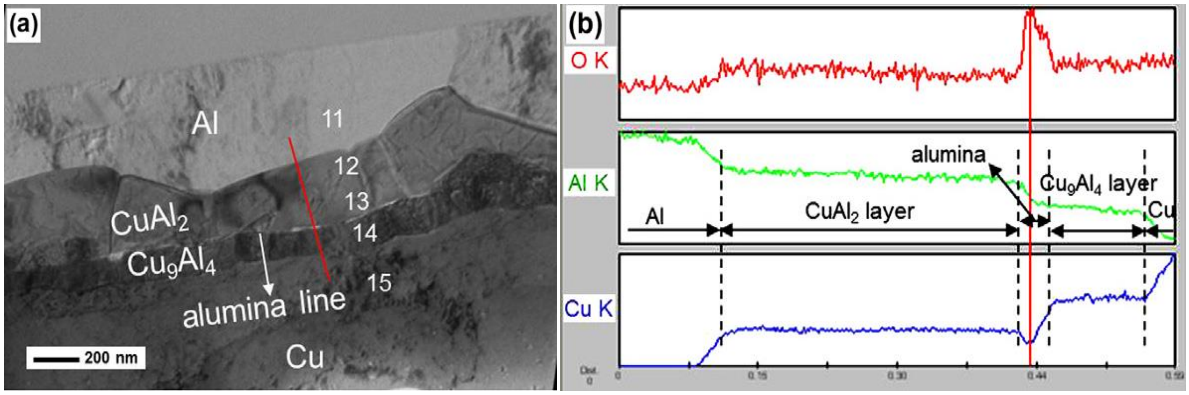

Region	O *K* at.%	Al *K* at.%	Au *L* at.%
11	7	93	0
12	5	59	36
13	6	57	37
14	5	27	68
15	7	0	93

Fig. 1.8 (a) A typical TEM image of the Cu–Al interface after annealing at 175 ℃ for 49 h; (b) EDX line scanning results along the line in (a) [46].

C. Al-Ni system

Al-Ni bonds are less prone to Kirkendall void formation and galvanic corrosion, thus more reliable than Al-Ag or Al-Au bonds under various environments [50, 51]. This system has been used in rapid production power devices and high-temperature applications such as aircraft turbine blades for over fifteen years. In most cases, Ni is deposited with electroless boride or with sulfamate solutions, which results in reliable bonds. However, phosphide electroless nickel solutions that co-deposit more than 6 or 8 mass% of phosphorous can result in both reliability and bondability problems. The main difficulty

encountered when bonding to nickel plating is bondability rather than reliability due to Ni surface oxidation. Thus, packages should be bonded as soon as possible after Ni-plating, protected in an inert atmosphere, or chemically cleaned before bonding. Controlling bonding machine schedules, such as impacting stress at tool wire plating with ultrasonic energy, can improve bondability of slightly oxidized nickel surfaces. Various surface preparation techniques (such as sandblasting) are sometimes applied before or after Ni plating to increase bondability. **Fig. 1.9** shows the SEM image of the bond cross-section interface. There is a large deformation in the wire, especially at the heel of the bond, and the cross-section deformation ratio (the ratio of the wire highness difference after bonding with the original wire diameter before bonding) is even up to 20–50%, so the oxide layer of Al_2O_3 inhibited diffusion [51] on the surface of the Al wire is broken thus exposing the pure metals locally at the interface, and at the same time, the contaminants on surface of the metallization is removed by the ultrasonic vibration. The element Ni diffuses into the Al wire through the Au layer, because there is a small step of Ni scanning line on the right of the gold layer (on the right of dash line). Therefore, the element Ni diffuses steadily into the Al wire, as shown in the right corner of **Fig. 1.9**.

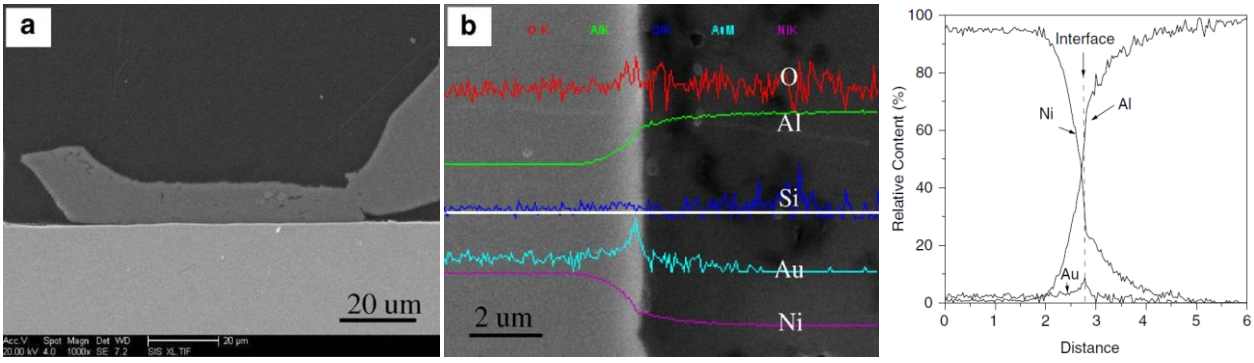

Fig. 1.9 The distribution of elements at the interface of the bond crosssection by EDAX line scan: (a) the cross-section of the bond; (b) the image of EDAX line scan (with ultrasonic power 120 mW, bonding pressure 30 gf and the bonding time 20 ms) [50].

1.4 Advanced ribbon bonding technology

Advanced ribbon bonding technology is attracting much attention for interconnections of next-generation power devices. Such ribbon bonding is expected to the applications to hybrid electric/electric vehicles and power plant electronics. Increasing demands for transmitting high current in the high power electronics industries requires alternative interconnect solutions. Ultimate reliability and extreme robustness together with improved productivity are also always considered to be the main objectives. For fulfilling high electrical load requirements in today's power devices, a single ribbon bond can replace a set of several wire bonds in interconnecting applications. In addition to current-carrying capability of ribbons, which can be adjusted by altering either its width or thickness, the contact area underneath the bond may perform an important role on high power devices. Multiple wires terminating on the same pad sometimes lead to a non-continuous contact area in which high current can flow to semiconductor. This may result in inhomogeneous heat dissipation and electric field strength (breakdown voltage). High power semiconductors can be expected to tolerate greater currents by a large continuous ribbon bond area rather than by multiple wire bonds. The amount of wires fitting on a pad is limited by the geometry of bonding tools (wedge or capillary) and by the deformation of wires. If a single ribbon can be used instead of multiple wires, the geometry of the bond tool does not matter as long as the distance to the next pad, or pitch, is large enough. The effect of deformation can be virtually ignored when ribbon is used since ribbon width increases than wire width. In absolute figures this depends on the ribbon dimensions and the relationship between width and thickness. As an example of bonding area related wiring deformation, a bonding area of typical string wire is deformed about 3 times than the wire diameter, a wedge bonding area is deformed about 1.4 times than the wire diameter, and a ribbon bonding area is deformed about 1.1 times the ribbon width if the width is at least 3 times the thickness, as shown in the **Fig. 1.10**. The lower vertical deformation required to bond the ribbon and in the greater proportion of material displacement occurring in the cross groove and the front and back of the bond foot. As described above, the ribbon bonding provides many advantages such as high electrical performance, high mechanical strength, and

saving stacked space on board compared with typical string wire bonding because the ribbon has larger cross-section and bond area compared to wire.

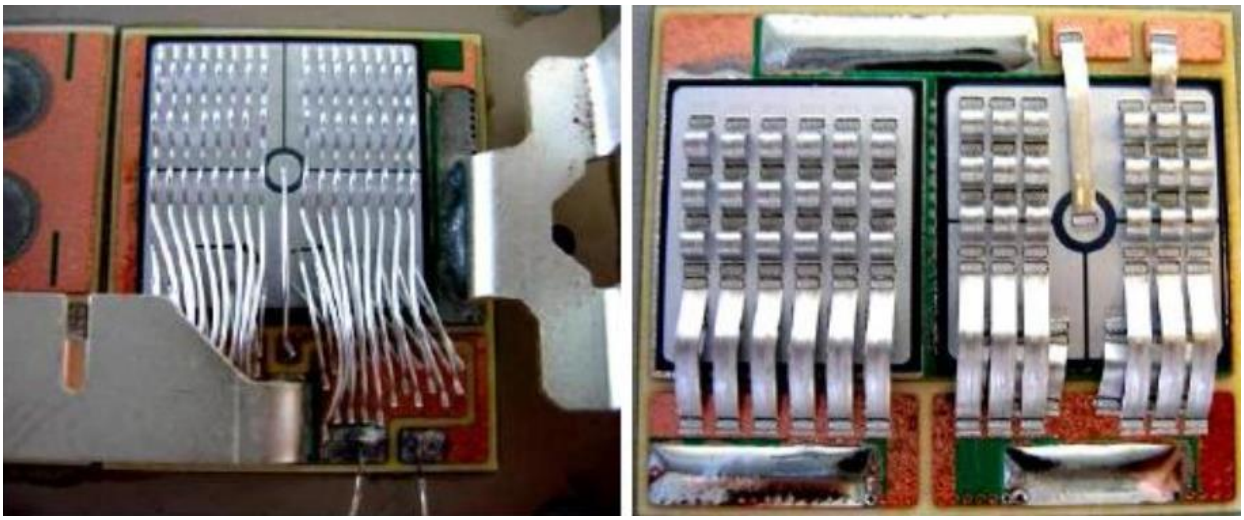

Fig. 1.10 Shows the replacement of thick wire bonds by ribbon bonding [52].

1.4.1 Typical wire bonding and novel ribbon bonding methods

The ribbon bonding process is developed from typical wire bonding process, which is the most popular and dominant interconnecting technology for micro and power electronics due to the fact that it offers a versatile, flexible, and robust connection method with proven performance and reliability. The wire bonding is one of solid state bonding processes. The metallic reaction between wire and substrate occurs due to ultrasonic energy and heat source. The wire bonding technologies can divide three bonding processes such as ultrasonic bonding, thermo-sonic bonding, and thermos-compression bonding [53]. The comparisons of these three technologies of wire bonding are indicated in **Table 1.2**.

Ultrasonic bonding is performed by a combination of ultrasonic power and bonding force at room temperature. The pressure of ultrasonic bonding is lower and bonding time is shorter than that of the thermo-compression bonding. The ultrasonic bonding is primarily used for thick metallic wires on

metallic pads, and has been the dominant technique for large-diameter ribbon in power electronics device applications. Thermo-sonic bonding is performed using a heat, bonding force, and ultrasonic power to bond wire on a substrate. Heat is applied by placing the package on a heated stage. Some bonders also have heated tool, which can improve the wire bonding performance. Force is applied by pressing the bonding tool into the wire to force it in contact with the substrate surface. Ultrasonic energy is applied by vibrating the bonding tool while it is contact with the wire. Thermo-sonic process is typically used for thin wire bonding. Thermo-compression is performed using heat and bonding force to deform the wire and make bonds. The main process parameters are temperature, bonding force, and bonding time. The diffusion reactions progress exponentially with temperature based on a diffusion welding theory [13]. In general, thermo-compression requires high temperature (normally above 300℃), and long bonding time to make bonds. That high temperature can damage some sensitive devices. In addition, the process is very sensitive to bonding surface contaminants. That is why the technology is seldom used now.

Table 1.2 Comparisons of wire bonding technologies

	Ultrasonic	Thermo-sonic	Thermo-compression
Ultrasonic power	High	Low	N/A
Bonding force	Low	Low	High
Temperature	Low (room temperature)	Middle (120~220℃)	High (300~500℃)
Bonding time	Short	Short	Long
Contamination	Middle	Middle	Strongly affected
Application	Thick wire or ribbon	Thin or thick wire	Thin wire

On the wire bond interface, related motion occurs due to the progressive tool vibration with dispersing oxidation layer at the adjacent bond surfaces. **Fig. 1.11** shows the metal ribbon bonding procedure with ultrasonic bonding. First step, the bonding system sets a bond position and bonded on substrates using friction energy with dispersing oxidation layer. And then, the bonding system is move to manufacturing the second bonds. The second bonding mechanism is same of the first bonding. Finally, the manufacturing of ultrasonic ribbon bonding is completed by ribbon cut.

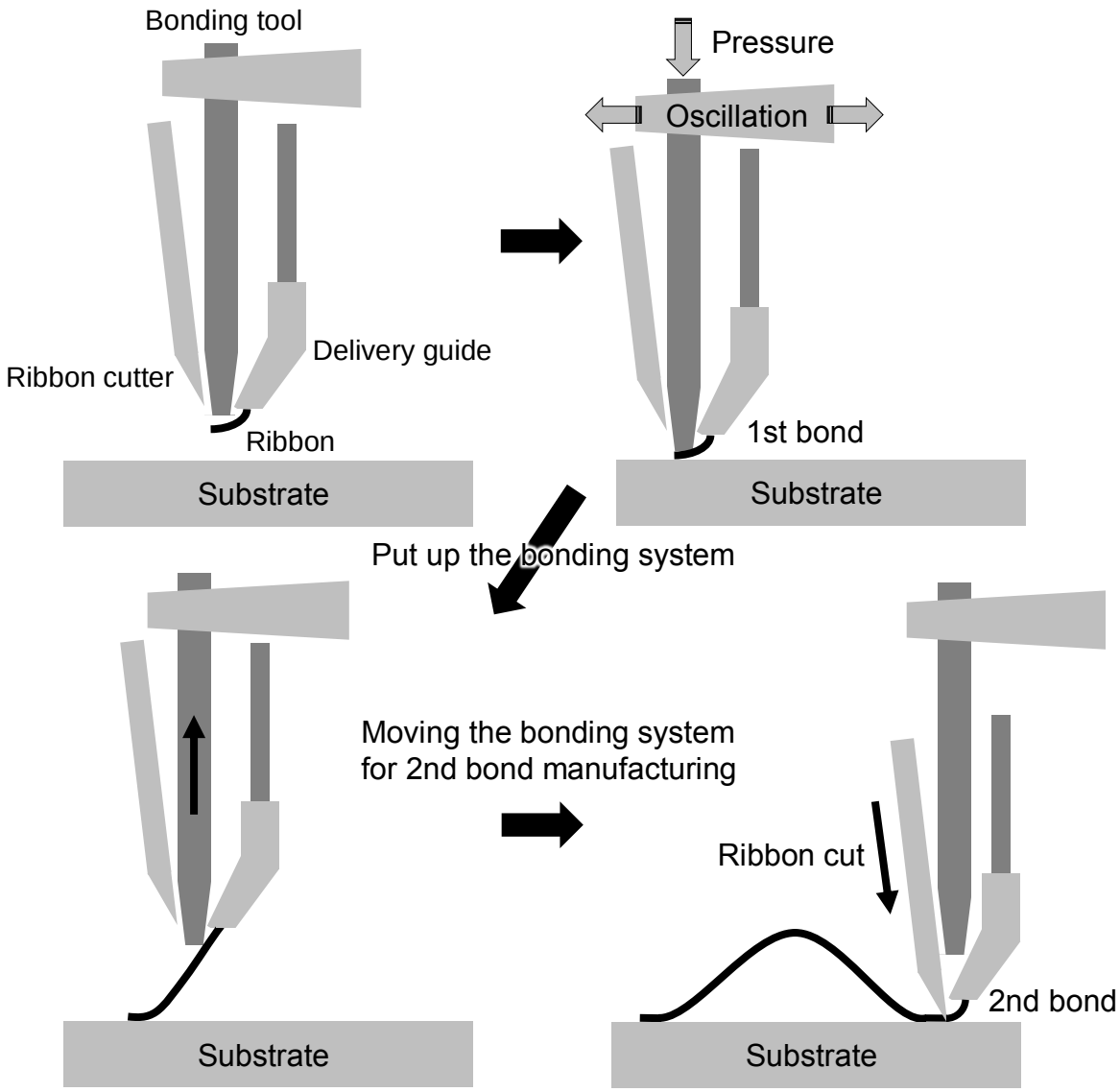

Fig. 1.11 Metal ribbon bonding procedure.

1.4.2 Effect of tool types with wedge and flat-form

In general, triangular shaped wedge tool is used in thick wire bonding. During the thick wire bonding process, cracks are frequently occurred by stress concentration at top or bottom edge of wire heel, which is called the "heel crack". Initiated heel cracks are propagated by high current/temperature service towards the central wire, and propagated heel cracks lead to degradation of joint stability, as shown in **Fig. 1.12**.

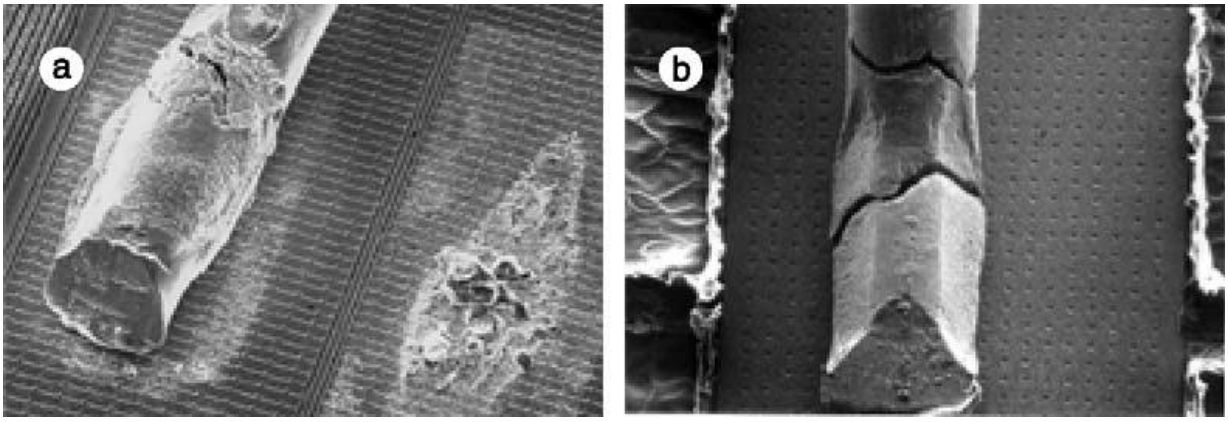

Fig. 1.12 (a) Initiation of Al wire heel crack using triangular bonding tool due to stress concentration by wire deformation and (b) their heel crack propagation during service [54].

Rectangular cross-sectional shaped ribbons are bonded using flat-form bonding tool to prevent a heel crack initiation. The occurrence of heel cracks can be fairly restrained using the flat-form tool to relieving stress concentration. The heel cracks is frequently initiated at bottom of ribbon loop edge during ribbon bonding process but is not occurred at top of ribbon loop edge. **Fig. 1.13** shows the stress comparisons depending on the bonding tool shapes with wedge and flat-form. Higher stress is concentrated at the triangular wedge tool tips by high deformation during string wire bonding, whereas, stress mitigation is expected using the flat-form bonding tool for ribbon bonding.

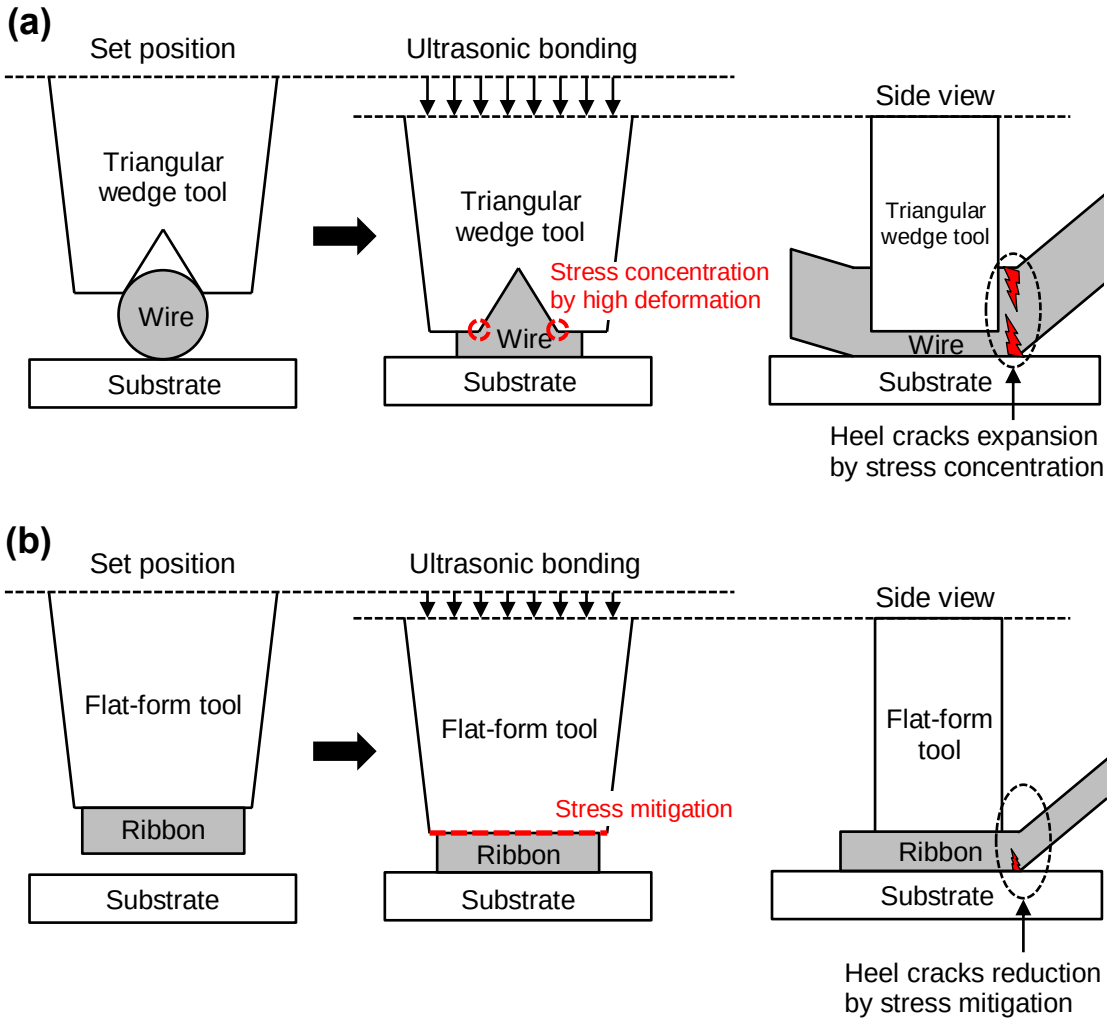

Fig. 1.13 Stress comparisons depending on the bonding tools: (a) wedge bonding tool, and (b) flat-form bonding tool.

1.5 Mechanical and thermal stability evaluations

A state of wire bonds can be evaluated with visual method and mechanical testing, depending on the requirements and the situation that may arise from previous experiences with a particular package or mechanical techniques. Visual method uses optical microscope, scanning electron microscope, and other analytical instruments to find the undesired bonds. Mechanical testing is employed for the evaluation of bond strength.

Destructive pull test, i.e. tensile strength test, is the major method to evaluate the bond strength by hooking and pulling the bonded wire until failure occurs [55–59]. The purpose of this test is to examine the bond strength and to certify the proper setup of the bonding parameters. The results are important evidences for evaluating bonding quality and reliability, as well as understanding bond failure mechanisms including flexure failures, interfacial de-adhesion, cratering, and shear fatigue at bonded interfaces during thermal cycling. Pull strength is strongly dependent upon the geometrical configuration of the pull testing. For absolute values of tensile strength, the pull test should be normalized. Based on the illustration of **Fig 1.14**, the force in each wire with the pull force at hook (F) is represented by

$$F_1 = \frac{F\cos(\theta_2 - \phi)}{\sin(\theta_1 + \theta_2)} \qquad (1)$$

$$F_2 = \frac{F\cos(\theta_1 + \phi)}{\sin(\theta_1 + \theta_2)} \qquad (2)$$

where ϕ is the pull angle, which is positive when the pull direction is deviated from the bond 1. F_1 is the component of force acting along the wire at the bond 1, F_2 along the wire at the bond 2. Equation (1) and equation (2) are the wire forces of the two bonds, which can be easily achieved, based on the hook

attachment position, and the hook heights from the two bonds. If both the bonds are at the same level and the hook is applied at the center, the forces can be represented as

$$F_1 = F_2 = \frac{F}{2\sin\theta} \qquad (3)$$

when the both angles are 30°, the pull force is equal to the break load. The failure during pull test may occur at one of the four positions in the wire bond structure:

A. Wire break at transition first bond
B. Wire break at transition second bond
C. Lift-off first bond
D. Lift-off second bond

when properly pulled, the bond should fail at A or B. If failures occur at C or D, then the bonding parameters, metallization, bonding machine, bonding tool, hook, has to be reviewed.

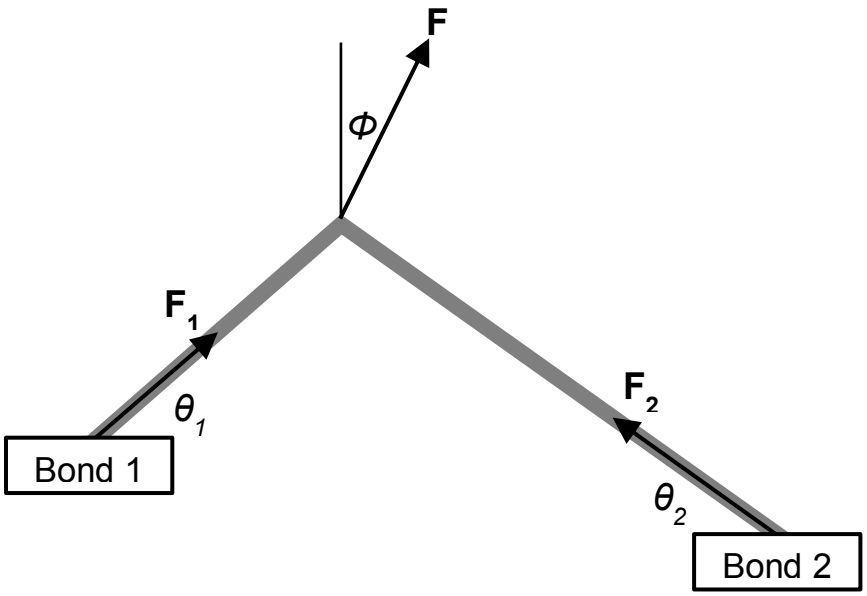

Fig. 1.14 Schematic diagram of pull strength evaluation [57].

Pull tests are suitable for mechanical strength evaluation of metal wirings but it is difficult to determining the strength of ball bonds. The reason is that the ball bonds have a large interfacial bonded area in the order of 6-10 times cross-section area of the wire, and the pull test often causes the bonded wire to break at a weak point for instance at the transition above the ball. Thus, little information about the ball bond strength is obtained unless its bonded area is less than 10% of its interfacial area. Therefore, to determine the ball bond strength, a shear test is necessary. Also, the shear test is helpful to discover cratering problems not normally uncovered by pull testing. This test is performed using a shear tool to push off ball bond with a sufficient force. However, cares must be taken to prevent incorrect and misleading data. The factors to influence the test include:

A. The improper vertical positioning of the tool, which should approach from 2.5 to 5 μm above the substrate. Otherwise the tool could drag on the substrate.
B. Cleanliness of shear tool.
C. Test speed may affect the shear strength.
D. Void-free intermetallic compounds formed in bond interfaces can lead to exceptionally high shear test values.

The shear test is also used mostly for ball bonds but it is not particularly useful for evaluating wedge bonds made from small-diameter wire. The reason is that pull test is very sensitive to the weakening of the bond heel, which increases with wire deformation, whereas shear test is completely independent of the condition of the heel and sensitive to the actual amount of bonded area.

Thermal environmental tests such as heat storage and thermal cycling have to perform to evaluate bond strength for electronics operating conditions. The purpose of those tests is to determine the electrical performance of wire bond interconnects to exposure to the temperatures alternatively changed. The degradation mechanisms by the test include flexure failure of the wire at the heel, bond pad-substrate shear failure, wire-substrate shear failure. Susceptibility to these failure mechanisms may be actuated by

excessive neck down at the heel or excessive embrittlement of the wire during bonding, or poor bond shear strength resulting from surface roughness and the presence of contaminants.

1.6 Objective and outline of the thesis

The next generation WBG semiconductors electronics instead of the conventional Si are expected to reduce an energy loss with high-temperature operation. In the interconnection technology between semiconductor chips and substrates or lead frames, string metal wire having a diameter of 400 μm have been commonly used. However, it cannot withstand the high breakdown voltage of more than 1 kV, and is easily destroyed at wire junction in the high-temperature operating environment, especially at 200 °C.

In Chapter 1, the goal of this thesis is for establishing "proposal of a new metal wiring technology with ultrasonic bonding process optimization" based on the survey of research trends and issues. Using ribbons replacing typical wires, it can be expected to improve the joint reliability under high-current/high-temperature because ribbons have a large cross sectional area. One ribbon (width 1500 × thickness 200 μm^2) has almost the same allowable current value compared to 3 string wires (400 μm), where area of the bond interfaces of a ribbon is much bigger than a string wire. However, a standard of ultrasonic ribbon bonding technology is not yet established in assessing reliability and their property at the present.

In Chapter 2, the optimization of the ultrasonic ribbon bonding process was performed to secure a steady bond interface and an applicability of practical power devices. Having a high formability 4N Al was selected as wirings material and their optimum ribbon bonding condition was established by verifying of each bonding parameter. In particular, a reaction mechanism in ultrasonic bonding was investigated.

For 4N Al ribbons, a grain coarsening easily occur at high operating temperatures exceeding 200 °C, which leads to wiring heel cracks. The prevention of mechanical degradation by heel crack propagations is necessary in order to secure the interconnections stability. Here, we propose a new structure ribbons using cladding or coating processes. In Chapter 3, Cu/Al clad ribbons for power electronics wiring was proposed to achieve high thermal/electrical performance together with easy manufacturing. The thermo-mechanical stability of Cu/Al clad ribbons was compared to Al ribbons by harsh environmental tests such as thermal exposure to 200 °C and thermal shock cycling at -40/250 °C. After the optimizing the

ultrasonic ribbon bonding parameters, Cu/Al clad ribbons always showed higher stability than Al ribbons independent because Cu-Al intermetallic compounds (IMCs) at the clad interfaces prevents heel crack propagation.

In Chapter 4, a major failure mechanism by heel crack propagations was investigated under accelerated high temperature tests such as thermal-exposed at 200 °C and thermal-shocked at -40/250 °C. The thermal and mechanical stability of ribbon wiring structures consist of a Cu/Al clad ribbon is superior to those of Al. However, the heel crack of a Cu/Al clad ribbon propagated due to grain coarsening within an Al layer. The heel crack was formed by grain coarsening due to continuous dynamic recrystallization (CDRX). Hence, the grain coarsening by CDRX is the main mechanism of heel crack propagation that degradation of the joint reliability.

In Chapter 5, the present thesis summarizes the ultrasonic ribbon bonding technology, which can ensure long-term high-temperature reliability for WBG semiconductor interconnections.

References

[1] T.P. Chow, High-voltage SiC and GaN power devices, Microelectronic Engineering 83 (2006) 112–122.

[2] C. Raynaud, D. Tournier, H. Morel, D. Planson, Comparison of high voltage and high temperature performances of wide bandgap semiconductors for vertical power devices, Diamond & Related Materials 19 (2010) 1–6.

[3] M.K. Das, Commercially Available Cree Silicon Carbide Power Devices: Historical Success of JBS Diodes and Future Power Switch Prospects, In: Proceedings of International Conference on Compound Semiconductor Manufacturing Technology, USA, 2011.

[4] K. Shenai, R.S. Scott, B.J. Baliga, Optimum semiconductors for high-power electronics, IEEE Transactions on Electron Devices 36 (1989) 1811–1823.

[5] B.J. Baliga, Power semiconductor device figure of merit for high-frequency applications, IEEE Transactions on Electron Devices Letters 10(10) (1989) 455–457.

[6] T.P. Chow, R. Tyagi, Wide bandgap compound semiconductors for superior high-voltage unipolar power devices, IEEE Transactions on Electron Devices 41 (1994) 1481–1482.

[7] C. Buttay, A. Masson, J. Li, M. Johnson, M. Lazar, C. Raynaud, and H. Morel, Die attach of power devices using silver sintering bonding process optimization and characterization, In: proceedings of the IMAPS High Temperature Electron. Netw., Oxford, U.K., 2011.

[8] M. Knoerr, S. Kraft, and A. Schletz, Reliability assessment of sintered nano-silver die attachment for power semiconductors, In: Proceedings of 12th Electronics Packaging Technology Conference, Singapore, 2010.

[9] R. Skuriat, J.F. Li, P.A. Agyakwa, N. Mattey, P. Evans, C.M. Johnson, Degradation of thermal interface materials for high-temperature power electronics applications, Microelectronics Reliability 53 (2013) 1933–1942.

[10] Y. Celnikier, L. Dupont, E. Herve, G. Coquery, L. Benabou, Optimization of wire connections design for power electronics, Microelectronics Reliability 51 (2011) 1892–1897.

[11] S. Ramminger, N. Seliger, Reliability model for Al wire bonds subjected to Heel crack failures, Microelectronics Reliability 40 (2000) 1521–1525.

[12] J.M. Hu, M. Pecht, A probabilistic approach for predicting thermal fatigue life of wire bonding in microelectronics, Journal of Electronic Packaging 113 (1991) 275–285.

[13] S. Ramminger, P. Turkes, Crack mechanism in wire bonding joints, Microelectronics Reliability 38 (1998) 1301–1305.

[14] M. Ciappa, Selected failure mechanisms of modern power modules, Microelectronics Reliability 42 (2002) 653–667.

[15] H. Lu, C. Bailey, C. Yin, Design for reliability of power electronics modules, Microelectronics Reliability 49 (2009) 1250–1255.

[16] T. Ueoka, J. Tsujino, Welding Characteristics of Aluminum and Copper Plate Specimens Welded by a 19 kHz Complex Vibration Ultrasonic Seam Welding System, Japanese Journal of Applied Physics 41(1) (2002) 3237–3242.

[17] E. Vries, Mechanics and Mechanisms of Ultrasonic Metal Welding, Ph.D. thesis, Ohio State University, Columbus, 2004.

[18] D.R. White, Ultrasonic Consolidation of Aluminum Tooling, Advanced Materials & Processes 161(1) (2003) 64–65.

[19] G.G. Harman, J. Albers, The Ultrasonic Welding Mechanism as Applied to Aluminum- and Gold-Wire Bonding in Microelectronics Aluminum- and Gold-Wire Bonding in Microelectronics, IEEE Transactions on Parts, Hybrids, and Packaging 13(4) (1977) 406–412.

[20] S.I. Matsuoka, Ultrasonic Welding of Ceramics/Metals Using Inserts, Journal of Material Processing Technology 75(1–3) (1998) 259–265.

[21] D.A. Grewell, A Prototype Expert System for Ultrasonic Welding of Plastics, Plastics Engineering 55 (1999) 33–37.

[22] G. Wagner, F. Walther, T. Nebel, D. Eier, Glass/Glass Joints by Ultrasonic Welding, Glass Technology 44 (2003) 152–155.

[23] W.H. Kearns, Welding Handbook, 7th ed., Vol. 3, American Welding Society, 1980, Chapter 10.

[24] G. Harman, Wire Bonding in Microelectronics Materials, Processes, Reliability, and Yield, second edition, McGraw-Hill, New York, 1997.

[25] R.R. Tummala, Fundamentals of Microsystems Packaging, McGraw-Hill, New York, 2001, Chapter 9.

[26] T. L. Landers, Electronics Manufacturing Processes, Prentice Hall, New Jersey, 1994, Chapter 4.

[27] R. Rodwell and D.A. Worrall, Quality Control in Ultrasonic Wire Bonding, International Journal for Hybrid Microelectronics 8(2) (1985) 1–8.

[28] L.R. Levine, Wire Bonding Optoelectronics Packages, Chip Scale Review, Nov. – Dec. 2001.

[29] J. Pan, R.M. Pafchek, F.F. Judd, J. Baxter, Effect of Chromium-Gold and Titanium- Titanium Nitride-Platinum-Gold Metallization on Wire/Ribbon Bondability, In: Proceedings of the 29th IEEE/CPMT/SEMI International Electronics Manufacturing Technology Symposium, San Jose, July 2004.

[30] M. Deley, L. Levine, The Emergence of High Volume Copper Ball Bonding, In: Proceedings of the 29th IEEE/CPMT/SEMI International Electronics Manufacturing Technology Symposium, San Jose, July 2004.

[31] C.D. Breach, What is the future of bonding wire? Will copper entirely replace gold?, Gold Bulletin 43(3) (2010) 150–168.

[32] C.J. Hang, C.Q. Wang, Y.H. Tian, M. Mayer, Y. Zhou, Microstructural study of copper free air balls in thermosonic wire bonding, Microelectronic Engineering 85 (2008) 1815–1819.

[33] C.J. Hang, W.H. Song, I. Lum, M. Mayer, Y. Zhou, C.Q. Wang, J.T. Moon, J. Persic, Effect of electronic flame off parameters on copper bonding wire: Free-air ball deformability, heat affected zone length, heat affected zone breaking force, Microelectronic Engineering 86 (2009) 2094–2103.

[34] H.M. Ho, W. Lam, S. Stoukatch, P. Ratchev, C.J. Vath, E. Beyne, Direct gold and copper wires bonding on copper, Microelectronics Reliability 43 (2003) 913−923.

[35] S. Murali, N. Srikanth, C.J. Vath, An analysis of intermetallics formation of gold and copper ball bonding on thermal aging, Materials Research Bulletin 38 (2003) 637−646.

[36] H. JI, M. Li, S. C. Wang, J. Guan, Evolution of the bond interface during ultrasonic Al-Si wire wedge bonding process, Journal of Materials Processing Technology 182 (2007) 202−206.

[37] S. Murali, N. Srikanth, C.J. Vath, Grains, deformation substructures, and slip bands observed in thermosonic copper ball bonding, Materials Characterization 50 (2003) 39−50.

[38] I. Lum, M. Mayer, Y. Zhou, Footprint study of ultrasonic wedge-bonding with aluminum wire on copper substrate, Journal of Electronic Materials 35(3) (2006) 433−442.

[39] J.E.Krzanowski, N. Murdeshwar, Deformation and bonding processes in aluminium ultrasonic wire wedge bonding, Journal of Electronic Materials 19(9) (1990) 919−924.

[40] H. Xu, C. Liu, V.V. Silberschmidt, S.S. Pramana, T.J. White, Z. Chen, A micromechanism study of thermosonic gold wire bonding on aluminum pad, Journal of Applied Physics 108 (2010) 113517.

[41] N. Noolu, N. Murdeshwar, K. Ely, J. Lippold, and W. Baeslack, Phase transformations in thermally exposed Au-Al ball bonds, Journal of Electronic Materials 33(4) (2004) 340−352.

[42] C.D. Breach, F. Wulff, New observations on intermetallic compound formation in gold ball bonds: general growth patterns and identification of two forms of Au_4Al, Microelectronics Reliability 44(6) (2004) 973−981.

[43] A. Karpel, G. Gur, Z. Atzmon, TEM microstructural analysis of As-Bonded Al–Au wire-bonds, Journal of Materials Science 42 (2007) 2334−2346.

[44] H. Ji, M. Li, J.M. Kim, D.W. Kim, C. Wang, Nano features of Al/Au ultrasonic bond interface observed by high resolution transmission electron microscopy, Materials Characterization 59 (2008) 1419−1424.

[45] H. Xu, C. Liu, V.V. Silberschmidt, S.S. Pramana, T.J. White, Z. Chen, V.L. Acoff, Intermetallic phase transformations in Au–Al wire bonds, Intermetallics 19 (2011) 1808–1816.

[46] H. Xu, C. Liu, V.V. Silberschmidt, S.S. Pramana, T.J. White, Z. Chen, V.L. Acoff, Behavior of aluminum oxide, intermetallics and voids in Cu–Al wire bonds, Acta Materialia 59 (2011) 5661–5673.

[47] H. Xu, C. Liu, V.V. Silberschmidt, S.S. Pramana, T.J. White, Z. Chen, A re-examination of the mechanism of thermosonic copper ball bonding on aluminium metallization pads, Scripta Materialia 61 (2009) 165–168.

[48] H. Kim, J. Lee, K. Baik, K. Koh, J. Won, S. Choe, J. Lee, J. Moon, Y. Park, Effects of Cu/Al intermetallic compound (IMC) on copper wire and aluminum pad bondability, IEEE Transactions on Components, Packaging and Manufacturing Technology 26(2) (2003) 367–374.

[49] M. Li, H. Ji, C. Wang, H.S. Bang, H.S. Bang, Interdiffusion of Al–Ni system enhanced by ultrasonic vibration at ambient temperature, Ultrasonics 45 (2006) 61-65.

[50] M. Li, H. Ji, C. Wang, H.S. Bang, H.S. Bang, Interdiffusion of Al–Ni system enhanced by ultrasonic vibration at ambient temperature, Ultrasonics 45 (2006) 61–65.

[51] D.E. Eakins, D.F. Bahr, M.G. Norton, An *in situ* TEM study of phase formation in gold-aluminum couples, Journal Materials Science 39 (2004) 165–171.

[52] C. Luechinger, Large Aluminum Ribbon Bonding-An Alternative Interconnect Solution for Power Module Applications, In: Proceedings of PCIM, Nuremberg, 2005.

[53] J. Pan, P. Fraud, Wire Bonding Challenges in Optoelectronics Packaging, In: Proceedings of 1st SME Annual Manufacturing Technology, USA, 2004.

[54] Y. Celnikier, L. Benabou, L. Dupont, G. Coquery, Investigation of the heel crack mechanism in Al connections for power electronics modules, Microelectronics Reliability 51 (2011) 965–974.

[55] M.G. Pecht, A. Zhong, A. Choubey, P.S. Chauan, Copper Wire Bonding, 1st ed. New York, Springer, 2014.

[56] G.G. Harman, C.A. Cannon, The microelectronic wire bond pull test – how to use it, how to abuse it, IEEE transaction on components, hybrids, and manufacturing technology 1(3) (1978) 203–210.

[57] ASTM standard test method: F459-06, Standard Test Method for Measuring Pull Strength of Microelectronic Wire Bonds, Annual listing of ASTM standards, ASTM International West Conshohocken, Pennsylvania, USA, 2006.

[58] ASTM standard test method: F458-06, Standard Non-Destructive Pull Testing of Wire Bonds, Annual listing of ASTM standards, ASTM International West Conshohocken, Pennsylvania, USA, 2006.

[59] S. Mazzei, M. Madia, S. Beretta, A. Mancaleoni, S. Aparo, Analysis of Cu-wire pull and shear test failure modes under ageing cycles and finite element modelling of Si-crack propagation. Microelectronics Reliability 53 (2014) 2501–2512.

Chapter 1
Introduction

Chapter 2

Process optimization and mechanism of ultrasonic bonding with Al ribbon wirings

2.1 Introduction

Interconnections in high power electronic devices generally require a wide capacity of electric current while both the device miniaturization and bond joint stabilities become the issues for next generation wide band-gap (WBG) semiconductors like silicon carbide (SiC) and gallium nitride (GaN) [1–4]. Both Cu and Al have been used as wiring materials in power devices. The materials characteristics of Cu and Al are compared in **Table 2.1** [5, 6]. The higher electrical and thermal conductivities of Cu are certainly advantageous to be applied for power device wiring. However, bare Cu wire is easily oxidized, and thus Cu ribbon may need special care like inert gas, or protective coatings for bonding [7]. The hardness and modulus of Cu higher than those of Al are drawback in bonding process leading to higher risk of chip fracture [7]. In the present study, we hence adopted Al ribbon to achieve sufficient joint reliability by ultrasonic bonding.

Table 2.1 Comparison of ribbon material characteristics at the ambient temperature

Material property	Al	Cu
Electrical resistivity (nΩ·m)	27	17
Thermal conductivity (W/m·K)	210	401
Vickers hardness (MPa)	167	369
Young's modulus (GPa)	68	110

In the WBG power module under a high current operating condition, high temperature above 200 ^{o}C can be reached at the wire joints. This high temperature causes an interface fracture and wire heel crack [8, 9]. In order to avoid these mechanical failures, heavy ribbon wiring is emerging in the field to replace the thick wires that are popularly used in integrated semiconductor device packaging. A transition from string metal wire interconnects to ribbon interconnects provides several advantages. The electrical advantages are higher current capacity and lower impedance. The mechanical advantages are higher bond

joint strength and stacked bonding capacity. Particularly, the wide cross-section areas of metal ribbon wires increase the maximum current through the wire, without increasing the total package size [10–12]. However, the bonding method of ribbon wires has not yet been established, particularly for bonding process stability in power devices.

Ultrasonic wire bonding method is popularly used in the device packaging, applying acoustic energy to wire bonding interface under the pressure by a tool tip [13]. During the bonding process, temperature elevation is undesirable to avoid the degradation of facing metal parts between wire and substrate, particularly for Al wires of which mechanical strength may be affected by grain growth at high-temperature. It is thus important to optimize the bonding parameters like normal force and acoustic power [14, 15].

In this study, we perform precise pull-tests to evaluate the mechanical reliability of Al ribbon bonds on electroless nickel immersion gold (ENIG) finished Cu substrate, and optimize the process parameters at ambient temperature. It is found that the ultrasonic sound bonding can be achieved without heating, showing no lift-off fracture due to heel cracking. Bond area and their propagation were examined by relative motions after shear-test to understand of bonding mechanism at the boned interface between Al ribbon and Cu substrate. We would suggest the optimized bonding parameters of heavy Al ribbon bonding, and investigated the mechanism of ultrasonic ribbon bonding.

2.2 Materials and experimental methods

Heavy ribbon bonding process that uses a flat form metal wire rather than thin metal string is a kind of wedge bonding process, and typically employs a bonding machine equipped with rectangular shaped tool head (**Fig. 2.1a**). In our case, TPT HB-30 semiautomatic ribbon bonder is used to maintain a certain bonding shape (**Fig. 2.1c**) as well as automated alignment and positioning. The machine can arrange in thermo-compression, thermo-sonic, and pure ultrasonic bonding processes of heavy metal ribbons like $1500 \times 200\ \mu m^2$ cross-section of Al or Cu wires. Gaiser LW-DWG111214 ribbon bonding tool is used

bonding system. The central cubic is arranged by central position of tool. A ribbon bonding process is used by the ultrasonic sound and normal bonding force. The first bonding step is combined by transducer oscillation with bonding tool pressure at ambient temperature during removal the oxide layer on the Al ribbon surface. Subsequently, the bonding system is lifted up from the first bonded point with 49.5^{o} of the ribbon angle, and then the ribbon is cut off by ribbon cutter after second bonding process. The second bonding process is same of the first bonding process.

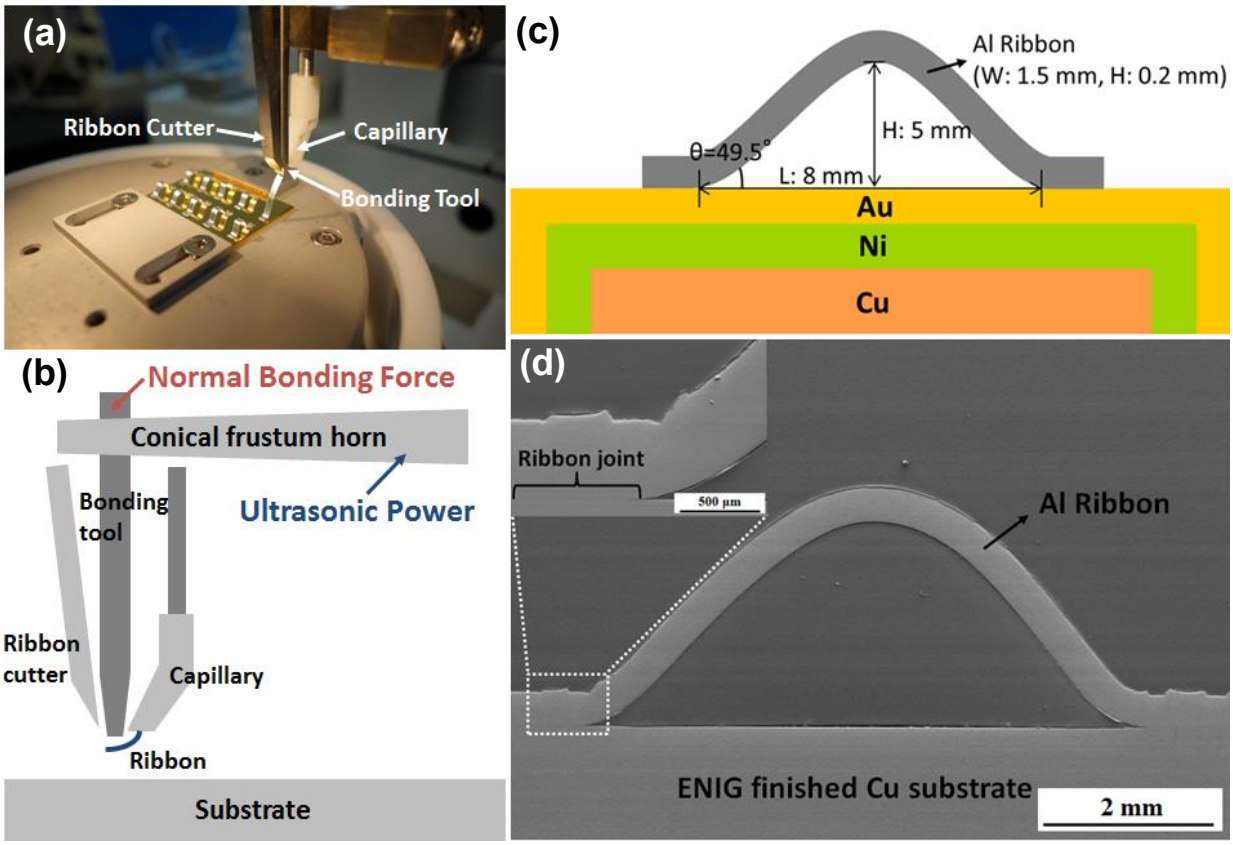

Fig. 2.1 Heavy ribbon bonding method; (a) TPT HB-30 semiautomatic ribbon bonder, (b) schematic illustration of applied bonding sources, (c) our standard design of ribbon wiring loop on ENIG finished Cu substrate, and (d) FE-SEM observation image of a cross-sectioned sample.

ENIG finished Cu substrates for our tests are electroless plated by Au (0.1 μm) /Ni (3 μm), which is a low cost chemical plating without introduction of electricity. Basically the principle of the electroless plating is that the chemical reactions are reduced on the activated solid solution's surface [16–18].

Focusing on ultrasonic bonding phenomena, we examined the variation of bonding parameters: ultrasonic power, bonding time, and normal bonding force. Twelve bonding samples were made by combination of each parameter. The ultrasonic power was varied from 0 to 20 W. The normal bonding forces were used from six levels of 0, 200, 400, 600, 800, and 1000 cN. The bonding times were 1, 1.2, 1.4, 1.6, 1.8, and 2.0 s, while the ultrasonic frequency was held constant at 60 kHz. Since the ribbon bonding area is bigger than that of thin string metal wire, such high ultrasonic power, long bonding time, and strong normal bonding force would be required for successful bonding.

2.3 Results

2.3.1 Mechanical evaluation by pull testing

Pull-test is popularly accepted for mechanical strength evaluation of wire bonding, and is generally useful to identify a source of reliability problems triggered by mechanical failures. Our ribbon bonding samples are also tested by pull-tests (Dage 4000-PXY) to evaluate the rupture force and the features of wire bonding process. It is noticed that pull-tests for ribbon bonding have not been standardized yet. Therefore, we have maintained the same shape of bonded wire loop shown in Figs. 3.1c and d, aiming to establish standard test conditions of ribbon wire pull-test.

Our results of ribbon bonding strength are plotted in **Fig. 2.2** for various bonding conditions of ultrasonic power and processing time. Several samples are tested in each bonding conditions, and the error bars show the standard deviations. **Fig. 2.2** obviously displays that higher power of ultrasonic results in higher rupture force, while the process times longer than 1.6 s exhibit no improvement in the strength.

2.3.2 Ribbon bonding parameters optimized by lift-off failure

Each pull-test ends in two failure modes, i.e. ribbon fracture and “lift-off” as shown in **Fig. 2.3**. The former mode means suitable condition of bonding process; almost fracture positions occurred near by the first bond. After first bonding process, the first loop angle has been increase and reduces again for the

second bonding. At this time, around the first loop has been weakened by repetitive load. The possibility of lift-off failures was summarized in **Table 2.2**. No lift-off failure occurs when 20 W is applied over 1.8 s. Without ultrasonic power, there was observed few or no fretting and bonding on the substrate, and all twelve bonds lifted off as separated interfaces between ribbon and substrate (**Fig. 2.4**). The complete bonding is only achieved over 20 W and 1.8 s conditions, and the resulting maximal rupture force reveals 28 N (**Fig. 2.2**). At this time, steady ribbon joint can be obtained by high ultrasonic energy over 35 J, as shown in **Fig. 2.5**. On the other hands, lift-off failure always occurs under the 18 W of ultrasonic power, and the rupture force remains less than 25 N. This means the Al ribbon used in the present study fractures at this tension, when our bonding loop geometry is adopted. Optimizations of Al ribbon bonding process have been achieved by evaluating mechanical rupture force by pull-test. The lift-off phenomenon at the reacted bond interfaces mainly depends on the acoustic energy of the ultrasound. The maximal mechanical rupture force about 28 N between Al ribbon and ENIG finished Cu substrate can be obtained by 1.8 s processing of 20 W ultrasonic powers.

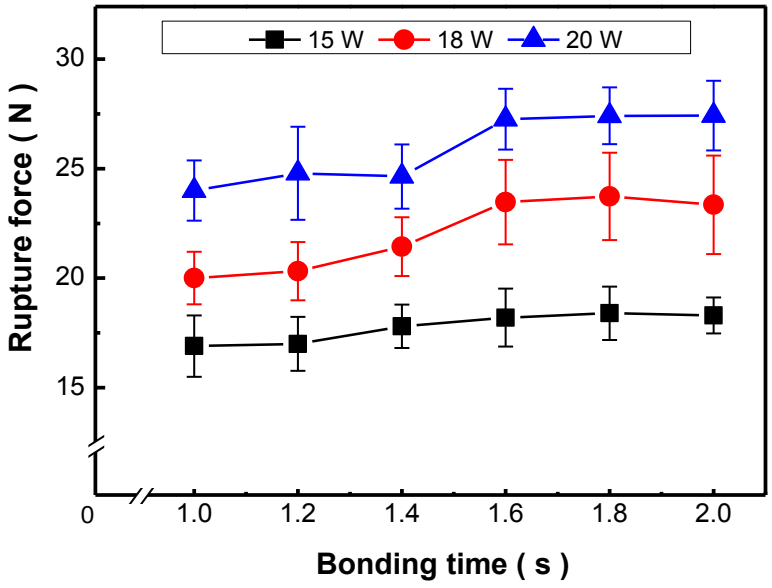

Fig. 2.2 Rupture force values of evaluating the pull test in different bonding conditions.

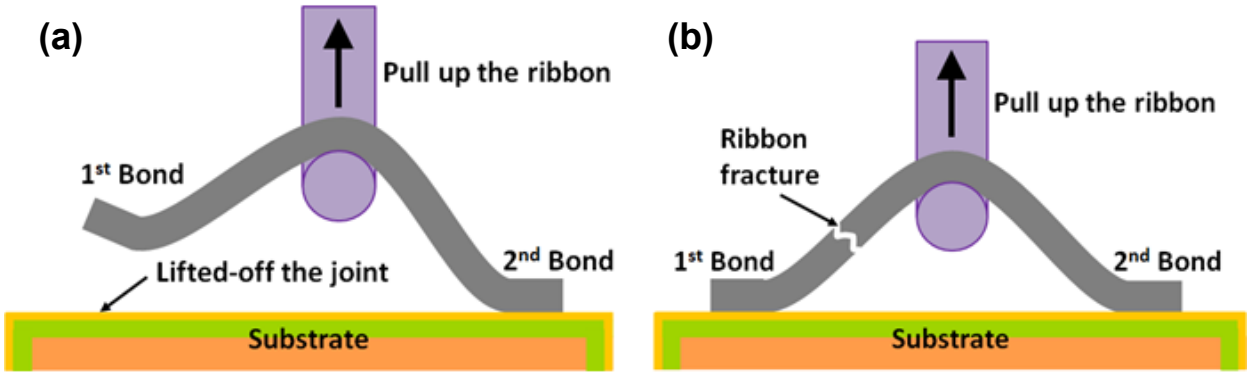

Fig. 2.3 Two failure modes of pull-test; (a) lift-off phenomenon, and (b) ribbon fracture phenomenon.

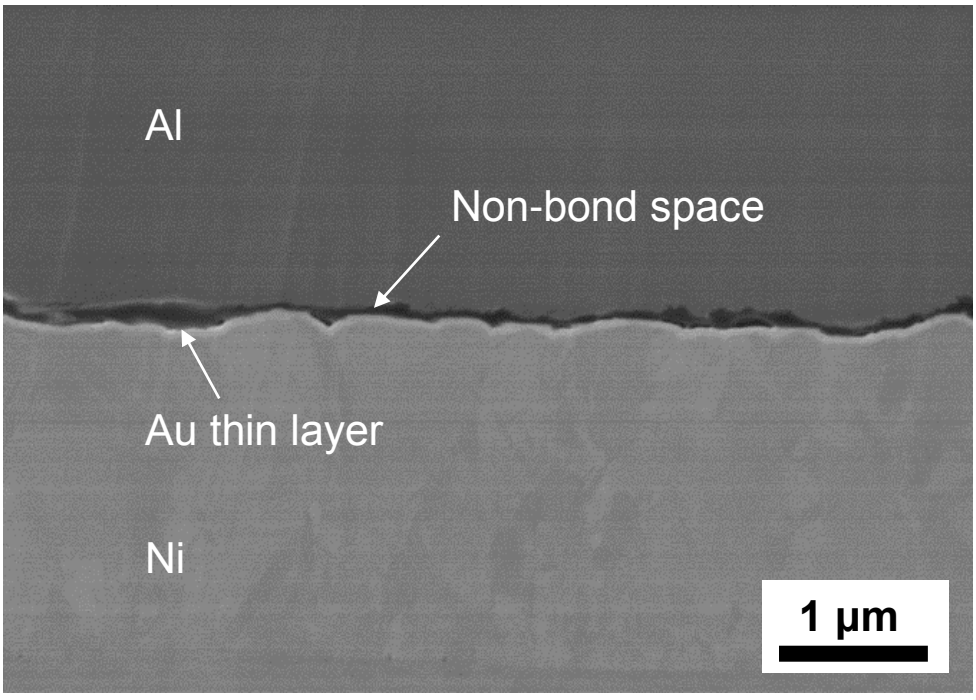

Fig. 2.4 Lift-off phenomenon occurred by lack of bonding conditions; less than ultrasonic power = 20 W and bonding time = 1.8 s.

Table 2.2 Lift-off occurrence rate after pull-test

Ultrasonic power (W)	Bonding time (s)					
	1.0	1.2	1.4	1.6	1.8	2.0
	Lift-off occurrence rate (%)					
15	100	100	100	100	100	100
16	100	100	100	100	100	100
17	100	100	100	90	100	90
18	100	90	100	80	90	80
19	90	80	90	40	30	20
20	80	60	40	10	0	0

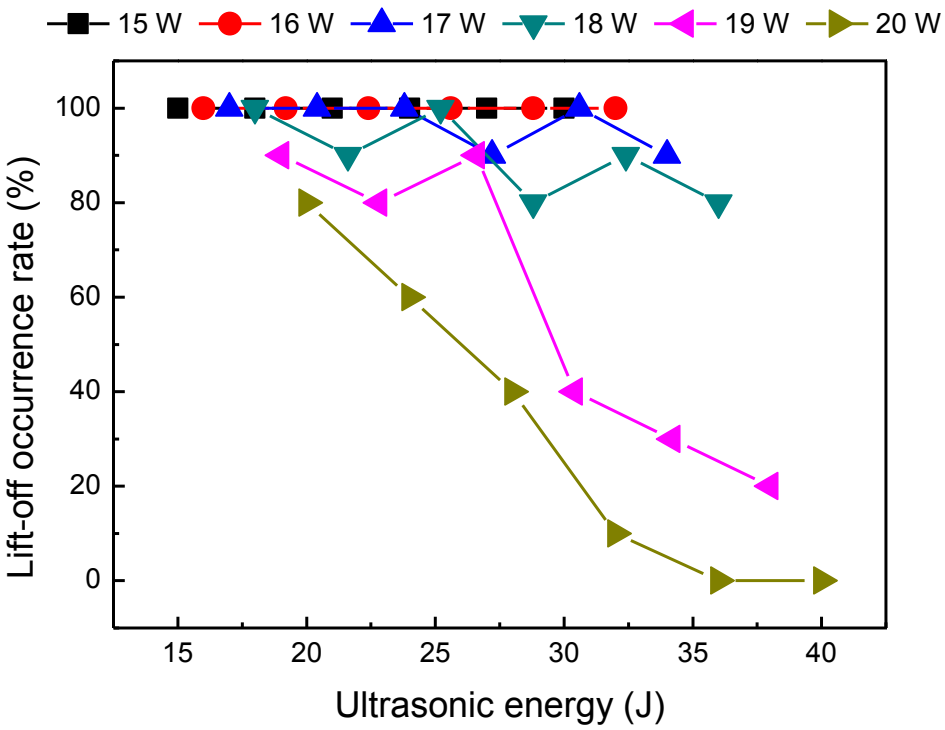

Fig. 2.5 A function of ultrasonic energy depending on lift-off occurrence.

2.3.3 Failure mode evaluation at the second bond joint by shear-test

The bondability of ribbon bonding was further investigated by verifying of normal bonding force from 0 N to 1000 cN. The fixed conditions of bonding parameter were ultrasonic power and bonding time in 20 W and 1.8 s, which is based on our optimized results by pull-test. As shown in **Fig. 2.6**, the highest shear force was indicated by 62 % relative motions at 800 cN. The maximum shear strength of 38 N obtained for Al ribbons are about three times higher than that of 300 μm round-shaped wire [19]. This large difference in shear strength comes from the smaller bonding area of thick wire than that of our ribbon wires. Without normal bonding force, there was observed 20 % relative motions between ribbon and substrate. It is almost same rate of the 200 cN normal bonding force. Increasing the maximum shear force has been increased the relative motion rate. However, the highest normal bonding force has not adopted the highest shear force. This means the highest normal bonding force is disturbed the oscillation of bonding tool. This will be discussed in detail at the following section.

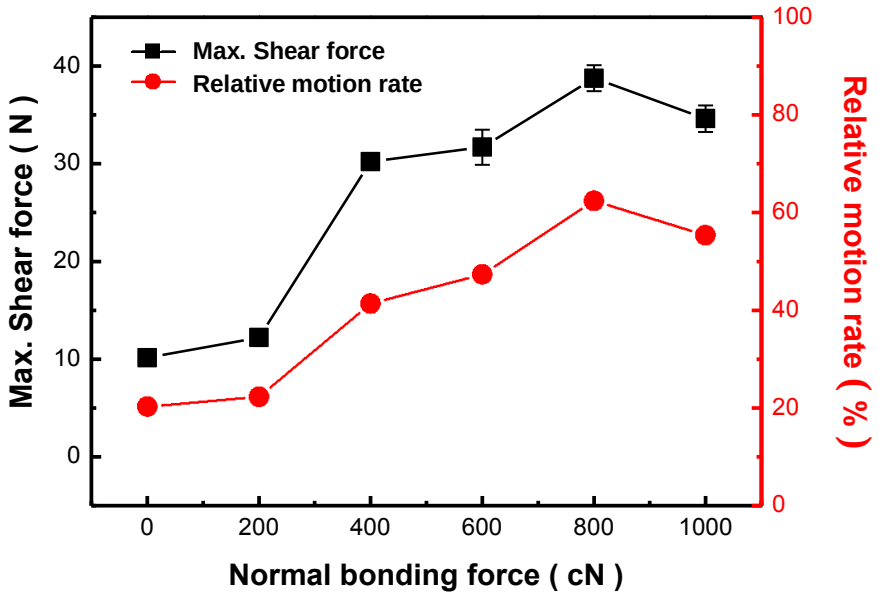

Fig. 2.6 Maximum shear force values in different normal bonding force conditions involved in the relative motions.

2.4 Discussion

2.4.1 Ribbon bonding mechanism by relative motions

Ultrasonic ribbon bonding method at the ambient temperature is required higher bonding parameters compared to thin string wire bonding. At a low ultrasonic power, microslip does not reach nearby the gross sliding area (**Fig. 2.7a**). This situation is observed for bonding performed under the condition of 16 W ultrasonic powers. Ultrasonic vibration activates a stable bond interface due to increased friction energy [20–22]. The mechanical strength of the ribbon joint was enhanced by relative motions. The relative motions are enhanced by increasing the friction energy following ultrasonic direction. As shown in **Fig. 2.7**, the model was developed based on classical microslip theory to explain the ultrasonic bonding phenomena observed in the evolution of reacted bonding area on the substrate (**Fig. 2.7a**). Microslip propagates to the outside of relative motion area (**Fig. 2.7b**). With increased ultrasonic power, bonding time and normal bonding force, the transition to gross sliding occurs by increasing the bonded area (**Fig. 2.7c**). The results of gross sliding indicated that the ribbon bonding mechanism is similar to the thin string wire bonding mechanism between Al wire and Au substrate [23]. However, the ribbon bonding process is different to thin string wire bonding process. Because the reacted bonding areas is bigger than wire ball bonding, and boned shape is rectangular morphology.

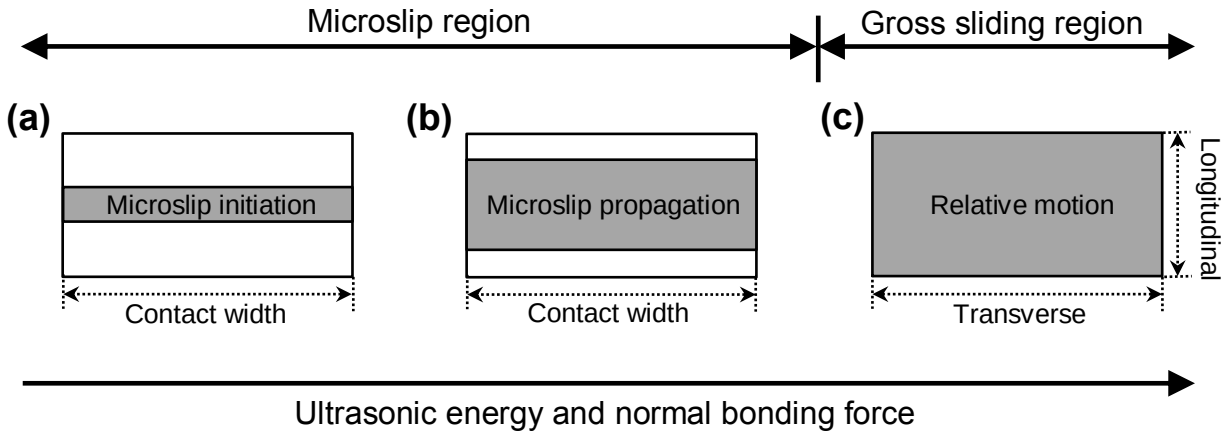

Fig. 2.7 Schematic illustrations of (a) microslip initiation in rectangular contact, (b) propagation of microslip from the initial microslip, and (c) rectangular contact area undergoing relative motion on the gross sliding.

2.4.2 Effects of microslip and gross sliding

In case of thin string wire bonding, the microslip fretting was indicated from outline of gross sliding areas [24]. With an increasing the normal bonding force, a transition from microslip into gross sliding will occur, as predicted by Mindlin's classical microslip theory for perfectly elastic spherical contacts [23]. The bond area shape of thin string wires is spherical regardless to the ball/wedge bonding methods. However, the typical contact area of a ribbon bond is rectangular shape. The microslip propagations of ribbon bonding are different to those of the wedge and balls as well. In thin string wire bonding, the microslip is initially propagated from the perimeter of the circular bonding tool [25]. On the contrary, the bonded ribbon area spreads from the center of the relative motion area (**Fig. 2.8**). In this study, we defined that the contact coordination of longitudinal and transverse axes influences the bond reaction based on the ultrasonic vibration directions (**Fig. 2.7**); longitudinal movement of the tool tip is larger than transverse one, and this relative movement easily propagates the microslip following longitudinal direction because of the rectangular tool morphology. The growth of relative motion leads to gross sliding between Al ribbon and Au metallization to achieve the bonding. As shown in **Fig. 2.9**, the size of relative motions were almost the same under the fixed normal bonding force independent to the varied ultrasonic power. The normal bonding force exhibited a decisive effect on the microslip essential to bonding stability.

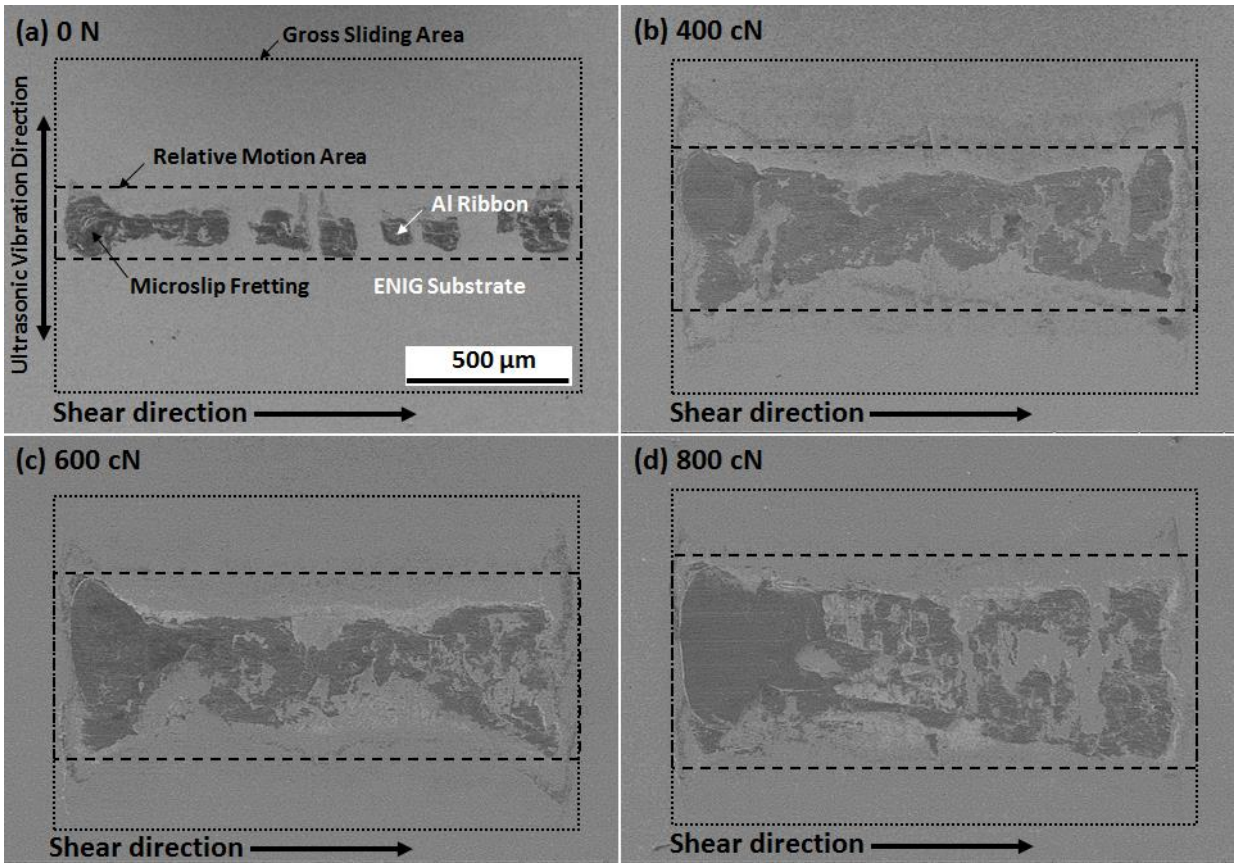

Fig. 2.8 Relative motions made with ultrasonic power = 20 W and bonding time = 1.8 s at various normal bonding forces. Sheared ribbon bonds made at (a) 0, (b) 400, (c) 600, and (d) 800 cN.

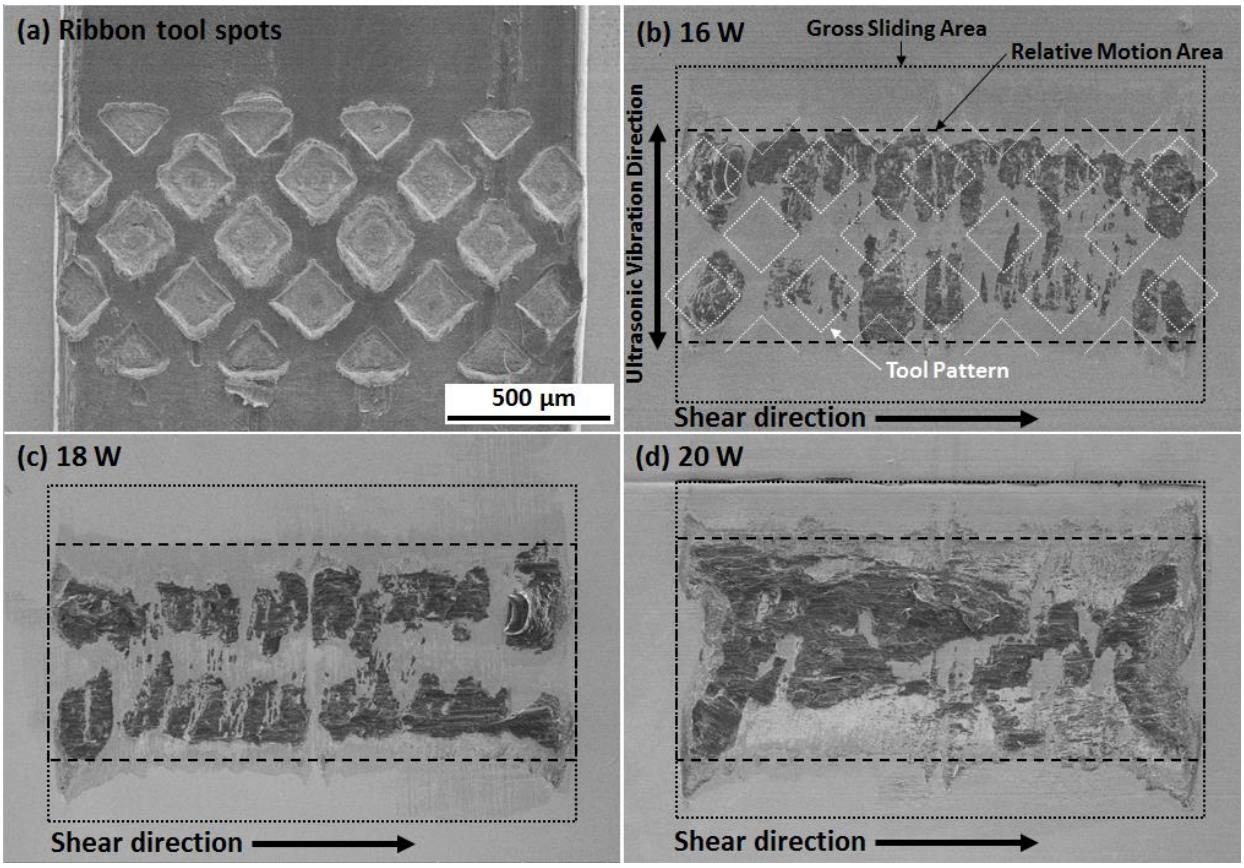

Fig. 2.9 (a) Flat-form ribbon tool morphology and relative motions made with normal bonding force = 1000 cN and bonding time = 1.8 s at various ultrasonic powers. Sheared ribbon bonds made at (b) 16, (c) 18, and (d) 20 W.

2.4.3 Splash effects

The ultrasonic bonding system consists of ultrasonic energy and normal bonding force. While applying the ultrasonic energy during bonding, shear forces add to the already applied normal bonding force. Such shear stress can transmit through bond pad metallization to the brittle, easily fractured the dielectrics, leading to pad peeling and bond failure [26–29]. Higher hardness wire material can smear off the soft pad material during bonding following the ultrasonic direction, which is commonly called “splash effect” [30]. The splash effect occurred at the bond interface, that phenomenon is disturbed to obtain high bonding strength. The pure Al ribbons have been selected for heavy ribbon bonding application. Because the hardness of pure Al is lower than metallization materials. Minimizing the splash effect at the metallization can be expected to higher bond ability. As shown in **Fig. 2.10**, the Au atoms were concentrated by splash effect at the relative motion edge. As the present results (**Fig. 2.6**), the highest shear force was measured the normal bonding force condition of 800 cN and then decreased after 800 cN. The maximum splash effect damage on substrate occurs at the relative motions edge. Based on the result, the migration of Au atoms occurred at the edge of bonded interface due to high normal bonding force following the ultrasonic longitudinal direction. Therefore, determining the normal bonding force and evaluating the splash effect are important for heavy ribbon bonding.

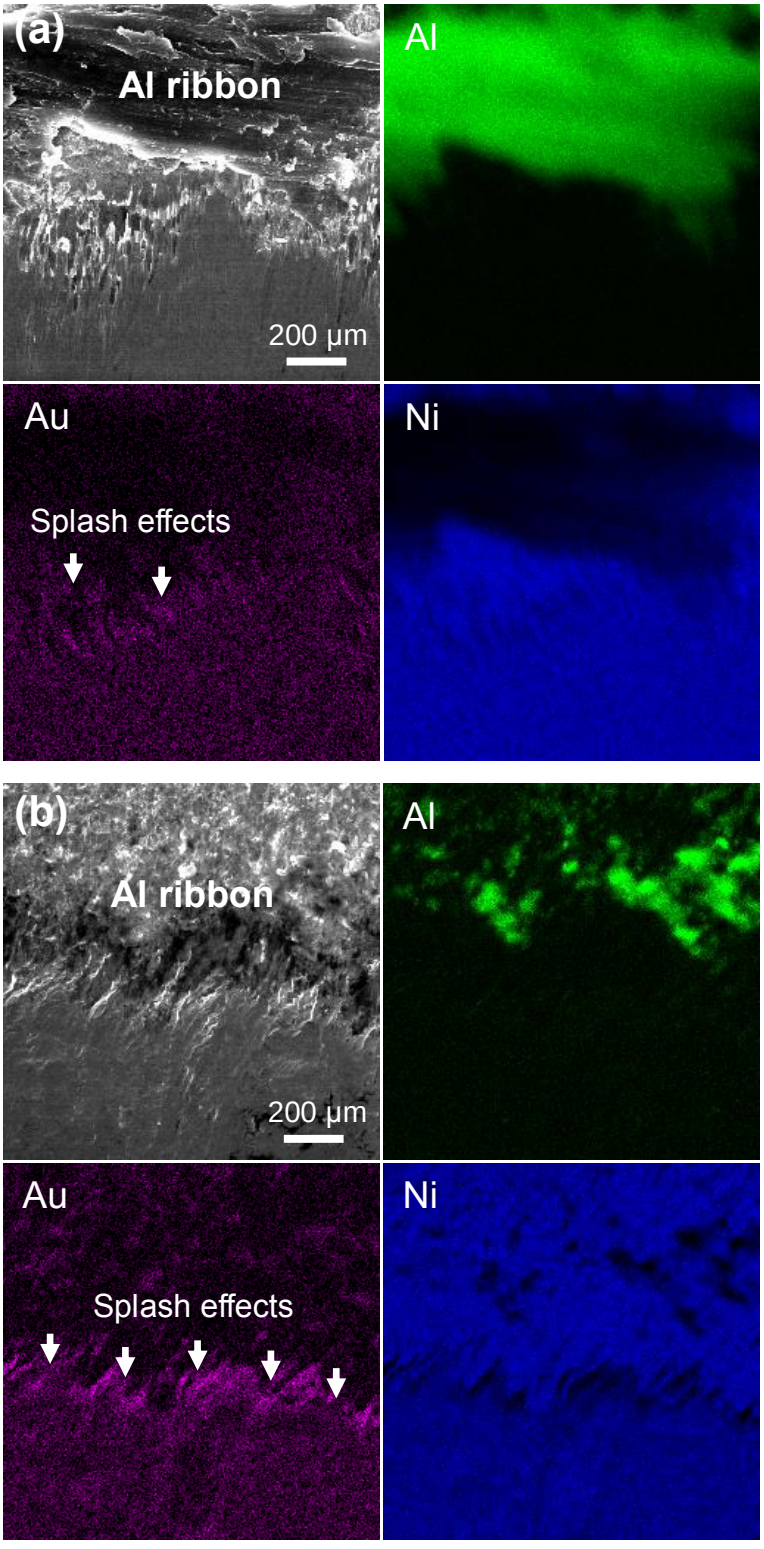

Fig. 2.10 EDS mapping results of splash effect at the relative motions edge by ultrasonic power = 20 W, bonding time = 1.8 s; (a) normal bonding force = 800 cN, and (b) normal bonding force = 1000 cN.

2.5 Conclusions

Pure Al ribbon bonding was examined on a typical ENIG finished Cu substrate to maximize the advantages of ribbon interconnections suitable for advanced power module packaging. The bonding parameters, namely ultrasonic power, bonding time and normal bonding force are higher than those of thin string wire bonding. The ribbon bonding requires thus the higher energy to achieve a sufficient mechanical strength to avoid lift-offs under pull-tests. The findings in our study on the ultrasonic ribbon bonding are summarized as follows.

The reliability of ribbon bonding can be evaluated by lift-off possibility under pull-tests. In our case, the lift-off phenomenon was observed for the powers lower than 20 W or bonding time shorter than 1.8 s. The highest rupture force between Al ribbon and ENIG finished Cu substrate was about 28 N, obtained for 1.8 s processing of 20 W ultrasonic power.

The microslip fretting is initiated on the transversal line at the center of the longitudinal movement of the tool tip, and then propagated to the longitudinal direction. The normal force essentially determines the size of microslip area, and hence the resulting bond strength.

When the normal bonding force exceeds 800 cN, the concentration of Au atoms was observed at the edge of the longitudinal relative motion. This splash effect has a critical influence on the bond reliability. Although the splash effect is necessary in order to remove the oxide layer on the Al ribbon surface, the Au layer must remain to maintain the Au-Al reaction. Adjusted to optimize the splash effect, the normal bonding force is the key to achieve an excellent stability of ultrasonic bonding between Al ribbons and ENIG finished Cu substrate.

References

[1] F. Roccaforte, A. Frazzettoa, G. Greco, F. Giannazzo, P. Fiorenza, R. Lo Nigro, M. Saggio, M. Leszczynski, P. Pristawko, V. Raineri, Critical issues for interfaces to p-type SiC and GaN in power devices,Applied Surface Science 258 (2012) 8324–8333.

[2] H. Matsunami, Current SiC technology for power electronic devices beyond Si, Microelectronic Engineering 83 (2006) 2–4.

[3] T. Paul Chow, High-voltage SiC and GaN power devices, Microelectronic Engineering 83 (2006) 112–122.

[4] R. Singh, Reliability and performance limitations in SiC power devices, Microelectronics Reliability 46 (2006) 713–730.

[5] E. Brandes, G. Brook: Smithells Metals Reference Book.

[6] http://www.matweb.com/

[7] H. Xu, I. Qin, H. Clauberg, B. Chylak, V. L. Acoff, Behavior of palladium and its impact on intermetallic growth in palladium-coated Cu wire bonding, Acta Materialia 61 (2013) 79–88.

[8] P. Agyakwa, M. Corfield, L. Yang, J. Li, V. Marques, C. Johnson, Microstructural evolution of ultrasonically bonded high purity Al wire during extended range thermal cycling, Microelectronics Reliability 51 (2011) 406–415.

[9] Y. Yamada, Y. Takaku, Y. Yagi, I. Nakagawa, T. Atsumi, M. Shirai, I. Ohnuma, K. Ishida, Reliability of wire-bonding and solder joint for high temperature operation of power semiconductor device Microelectronics Reliability 47 (2007) 2147–2151.

[10] M. Li, H. Ji, C. Wang, H. Bang, H. Bang, Interdiffusion of Al–Ni system enhanced by ultrasonic vibration at ambient temperature Ultrasonics 45 (2006) 61–65.

[11] A. Shah, H. Gaul, M. Schneider-Ramelow, H. Reichl, M. Mayer, Ultrasonic friction power during Al wire wedge-wedge bonding, Journal of Applied Physics 106 (2009) 013503.

[12] X. Liu, G. Lu, Power Chip Interconnection: From Wirebonding to Area Bonding, The International Journal of Microcircuits and Electronic Packaging 23 (2000) 407–413.

[13] M. Ando, M. Maeda, Y. Takahashi, Evolution of Interfacial Shear Force during Ultrasonic Al Ribbon Bonding, Materials Transactions 54(6) (2013) 911–915.

[14] S. Pietranico, S. Lefebvre, S. Pommier, M. Berkani Bouaroudj, S. Bontemps, A study of the effect of degradation of the aluminium metallization layer in the case of power semiconductor devices, Microelectronics Reliability 51 (2011) 1824–1829.

[15] U. Geibler, M. Schneider-ramelow, K. lang, H. reichl, Investigation of Microstructural Processes during Ultrasonic Wedge/Wedge Bonding of AlSi1 Wires, Journal of Electronic Materials 35(1) (2006) 173–180.

[16] H. Clauberg, P. Backus, B. Chylak, Nickel–palladium bond pads for copper wire bonding Microelectronics Reliability 51 (2011) 75–80.

[17] C. Biasotto, L. B. Isoda, C. S. Franco, N. Armigliato, Evaluation of low cost metallization process for power electronics module by wire wedge bond process on Nickel/Copper and Nickel/Copper/Silver pads, ECS Transactions 39(1) (2011) 385–392.

[18] K. Honsho, H. Terai, H. Yamazoe, T. Tatsuta, O. Tsuji, A New Plasma Process for Surface Treatment prior to Wire Bonding that Utilizes the Sublimation Effect of Alkyl Group Radicals, Japanese Journal of Applied Physics 42 (2003) 7112–7115.

[19] T. Komiyama, Y. Chonan, J. Onuki, M. Koizumi, T. Shigemura, High-Temperature Thick Al Wire Bonding Technology for High-Power Modules, Japanese Journal of Applied Physics 41 (2002) 5030–5033.

[20] H. Xu, C. Liu, V.V. Silberschmidt, S.S. Pramana, T.J. White, Z. Chen, V.L. Acoff, Intermetallic phase transformations in Au–Al wire bonds, Intermetallics 19 (2011) 1808–1816.

[21] J. Li, L. Han, J. Duan, J. Zhong, Microstructural characteristics of Au/Al bonded interfaces, Materials Characterization 58 (2007) 103–107.

[22] H. Ji, M. Li, J. Kim, D. Kim, C. Wang, Nano features of Al/Au ultrasonic bond interface observed by high resolution transmission electron microscopy, Materials Characterization 58 (2008) 1419–1424.

[23] I. LUM, M. Mayer, Y. Zhou, Footprint Study of Ultrasonic Wedge-Bonding with Aluminum Wire on Copper Substrate, Journal of Electronic Materials 35(3) (2006) 433–442.

[24] I. LUM, J. P. Jumg, Y. Zyou, Bonding Mechanism in Ultrasonic Gold Ball Bonds on Copper Substrate, Metallurgical Materials Transactions A 36A (2005) 1279–1286.

[25] H. Ji, M. Li, C. Wang, J. Guan, H. Bang, Evolution of the bond interface during ultrasonic Al–Si wire wedge bonding process, Journal of Materials Processing Technology 182 (2007) 202–206.

[26] B. K. Appelt, A. Tseng, C. Chen, Y. Lai, Fine pitch copper wire bonding in high volume production, Microelectronics Reliability 51 (2011) 13–20.

[27] A. Rezvani, A. Shah, M. Mayer, Y. Zhou, J.T. Moon, Role of impact ultrasound on bond strength and Al pad splash in Cu wire bonding, Microelectronics Reliability 53 (2013) 1002–1008.

[28] A. Shah, A. Rezvani, M. Mayer, Y. Zhou, J. Persic, J.T. Moon, Reduction of ultrasonic pad stress and aluminum splash in copper ball bonding, Microelectronics Reliability 51 (2011) 67–74.

[29] M. Maeda, Y. Yoneshima, H. Kitamura, K. Yamane, Y. Takahashi, Deformation Behavior of Thick Aluminum Wire during Ultrasonic Bonding, Materials Transactions 54 (2013) 916–921.

[30] B. Chylak, J. Ling, H. Clauberg, T. Thieme, next generation nickel based bond pads enable Cu wire bonding, ECS Transactions 18(1) (2009) 777–785.

Chapter 3

A comparison of the high-temperature stability of Al and Cu/Al clad ribbon wirings

3.1 Introduction

Ultrasonic wire bonding is a key technique to interconnect between the chip and a substrate or a lead frame in power electronics. String wires are typically used in the power electronic industries but have limitations with regard to higher current-carrying capacity in packaged power modules [1, 2]. To overcome the limitations caused by the use of typical string wires, the direct bonding of novel rectangular ribbons is attracting much attention as an interconnection technology, because the cross-sectional area of ribbons is wider than that of typical string wires. The novel rectangular ribbons provide several advantages such as high current density, low impedance, and high bond joint strength. Particularly, use of a wide cross-sectional ribbon can help achieve the maximum current density through the wirings without increasing the total package size [3].

In general, Al is used in ribbon interconnections because of its excellent formability in wiring process. However, heel cracks are frequently formed from high bonding pressure and ultrasonic energy around the Al ribbon loops (top and bottom regions) because Al is a soft material. Subsequently, the heel cracks are propagated along the Al grain boundaries during high-temperature operation [4–6]. To prevent heel crack propagation, a Cu layer is cladded on the Al layer by a cold rolling process. Cu has many advantages such as higher electrical/thermal conductivities than Al. However, higher bonding parameters such as ultrasonic power, normal bonding force, bonding time, and ultrasonic frequency are required for successful Cu/Al clad ribbon wiring because Cu has higher acoustic impedance and hardness than Al.

The service temperature of power electronics is higher than that of micro-electronics due to the high current flow. At the same time, joint failures occur easily due to cracking and intermetallic compound (IMC) growth between ribbon and chip/substrate under high service temperature. Voids and cracks are formed on IMC interfaces because of an increasing diffusion rate. Subsequently, mechanical strength degradation occurs depending on the growth of crack length and IMC thickness [7–9]. In the present work, various IMCs were formed on bond and clad interfaces, and ribbon heel cracks were present within the Al layers during thermally harsh tests. Those heel crack tips occurred at the edge of ribbon bond heel and

propagated reaching to the Cu-Al IMC layers within the clad interface. Consequently, the mechanical strength of Cu/Al clad ribbon wirings decreased with increasing heel crack length and Cu-Al IMCs thickness. Thus, we investigated the correlation of microstructural evolution and mechanical stability with regard to heel crack propagation and Cu-Al IMC formation during harsh tests after determining a suitable ultrasonic ribbon bonding process.

3.2 Materials and experimental methods

Al and Cu/Al clad ribbons (width 1500 μm × height 200 μm) were bonded on electroless nickel immersion gold (ENIG) finished Cu substrates with suitable ultrasonic bonding parameters at ambient temperature, as illustrated in **Fig. 3.1a**. The wiring loop design of the Al ribbon is the same as that of the Cu/Al clad ribbon, and both structures have a similar contact area between ribbon and substrate. The wiring length between the first and second bonds is 8 mm, and the height of the wiring loop is 5 mm. **Fig. 3.1b** shows a comparison of the Al and Cu/Al clad ribbons. High-purity Al (99.99 mass%) and Cu (99.99 mass%) metals were used in the ribbon materials. The ENIG-finished Cu substrate was coated on a Cu plate with Au (0.1 μm)/Ni (3 μm) by electroplating. The role of plated Au is to reduce surface oxidation, and plated Ni is a diffusion barrier layer between the Al ribbon or layer and the Cu plate [10, 11]. **Figs. 3.1c** and **d** show the cross-sectional images of the Al and Cu/Al ribbon wirings at the first bond zone. The Cu/Al clad ribbon was manufactured by a cold rolling process. Subsequently, an annealing process was performed at 100 °C to relieve the residual stress at the Cu/Al clad interface. The area ratio of the Cu layer within the Cu/Al clad ribbon is twice as large as that of the Al layer, as shown in **Fig. 3.1e**.

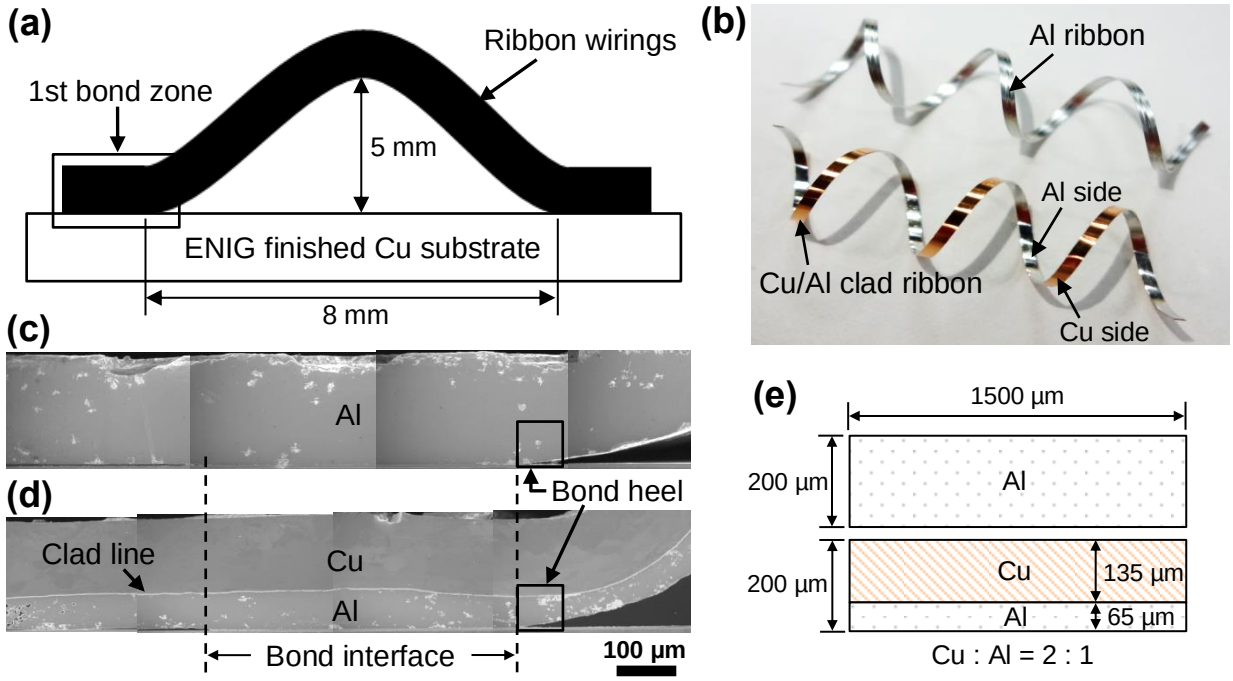

Fig. 3.1 Schematic images: (a) illustration of wiring sample design, (b) a comparison of the Al ribbon and the Cu/Al clad ribbon, cross-sectional images of (c) the Al ribbon and (d) the Cu/Al clad ribbon at the first bonded zone, and (e) size comparison of the Al and Cu/Al clad ribbons.

Ultrasonic ribbon bonding was conducted with TPT HB-30 (Al ribbon bonding) and Orthodyne 3600 plus (Cu/Al clad ribbon bonding) wedge/ribbon semiautomatic bonders to maintain a steady ribbon wiring formation. A flat-form bonding tool was used in the bonders to avoid the occurrence of heel cracks at the top of the ribbon heels. The ultrasonic bonding of Al and Cu/Al clad ribbons was optimized by varying the ultrasonic power, normal bonding force, and bonding time, focusing on the highest pull strength. The optimized ribbon bonding samples were subjected in harsh tests such as thermal exposure at 200 °C and thermal shock cycling at -40/250 °C. Subsequently, the ribbon pull testing was performed under each harsh test condition (as bonded, after 1000/2000 h, and after 1000/2000 cycles) to evaluate the mechanical stability of the ribbon wirings. A Dage 4000 series pull/shear tester was used for ribbon pull testing. The fracture mode and IMC formation were observed using field emission-scanning electron microscopy (FE-SEM), and their quantitative elements were analyzed using an electron probe micro

analyzer (EPMA) and energy dispersive spectroscopy (EDS). The average grain size of Al was also measured using electron backscatter diffraction (EBSD).

3.3 Results and discussion

3.3.1 Optimization of ultrasonic ribbon bonding

The acoustic impedance (Z) in dissimilar metal joints during ultrasonic bonding is proportionally related to the ultrasound velocity (V) and density (ρ) of the material [12]:

$$Z = V \cdot \rho \qquad (1)$$

As shown in **Table 3.1**, denser materials such as Cu, Ni, and Au have high acoustic impedances, whereas Al has relatively low acoustic impedance. This characteristic explains why high bonding parameters are essential for Cu/Al clad ribbon bonding. Furthermore, the ultrasound reflection of a Cu/Al clad ribbon is larger than that of an Al ribbon because a Cu/Al clad ribbon consists of a Cu layer and an Al layer. The ultrasound wave is reflected or transmitted at the interface of different materials during ultrasonic bonding [13]. Steady ribbon joints are made by transmitted ultrasound energy. The effects of ultrasound waves between different interfaces can be calculated by using the reflection and transmission equations:

$$R = \frac{(Z_2 - Z_1)^2}{(Z_2 + Z_1)^2} \qquad (2)$$

$$T = 1 - R \qquad (3)$$

where R is the reflection coefficient at dissimilar interfaces, Z_1 and Z_2 are acoustic impedances of adjacent materials (first and second materials from transducer), and T is the transmission coefficient. **Fig. 3.2** shows the ultrasound waves with regard to reflection and transmission of the Al ribbon and the Cu/Al clad ribbon bonding. Assuming an ultrasound transmission of T_{total} = 100 % from the transducer, T_{final} of the Al ribbon bonding can be determined to be 53 % (R = 47 %) between the Al ribbon and substrate, which is higher than the value of T_{final} of the Cu/Al clad ribbon (23 %), as illustrated in **Fig 3.2a**. The T_{final} value of Cu/Al clad ribbon bonding is 30 % even in T_{total} = 100 % because ultrasound reflection (R_1 = 43 %) occurred at the Cu/Al clad interfaces as a result of the difference in acoustic impedances between the Cu and Al layers, as illustrated in **Fig. 3.2b**. Higher value of ultrasound energy is necessary for Cu/Al ribbon bonding compared to Al ribbon bonding. Therefore, it is necessary to optimize the bonding process with regard to ultrasound reflection and transmission of acoustic impendence to achieve successful manufacturing of ribbon wirings.

Wide cross-sectional ribbon bonding has to require higher bonding parameters such as ultrasonic power, bonding force, bonding time, and ultrasonic frequency than typical string wire bonding because which has 3 times wider cross-sectional area than that of 300 μm typical string wire. Particularly, Cu/Al clad ribbon bonding requires higher bonding parameters to successful manufacture their ribbon wirings than the Al ribbon bonding because Cu has higher acoustic impedance and hardness as compared to Al. Our suitable bonding parameters of the Al and Cu/Al clad ribbon wirings depending on the highest pull strength presented in **Table 3.2**.

Table 3.1 Material property of used metals

Materials	Acoustic impedance ($N \cdot s \cdot m^{-3}$)	Density ($g \cdot cm^{-3}$)	Ultrasound velocity (m/s)	Vickers hardness (MPa)
Al	17.4	2.7	6420	167
Cu	44.6	8.9	5010	369
Au	63.8	19.7	3240	216
Ni	49.5	8.8	5600	638

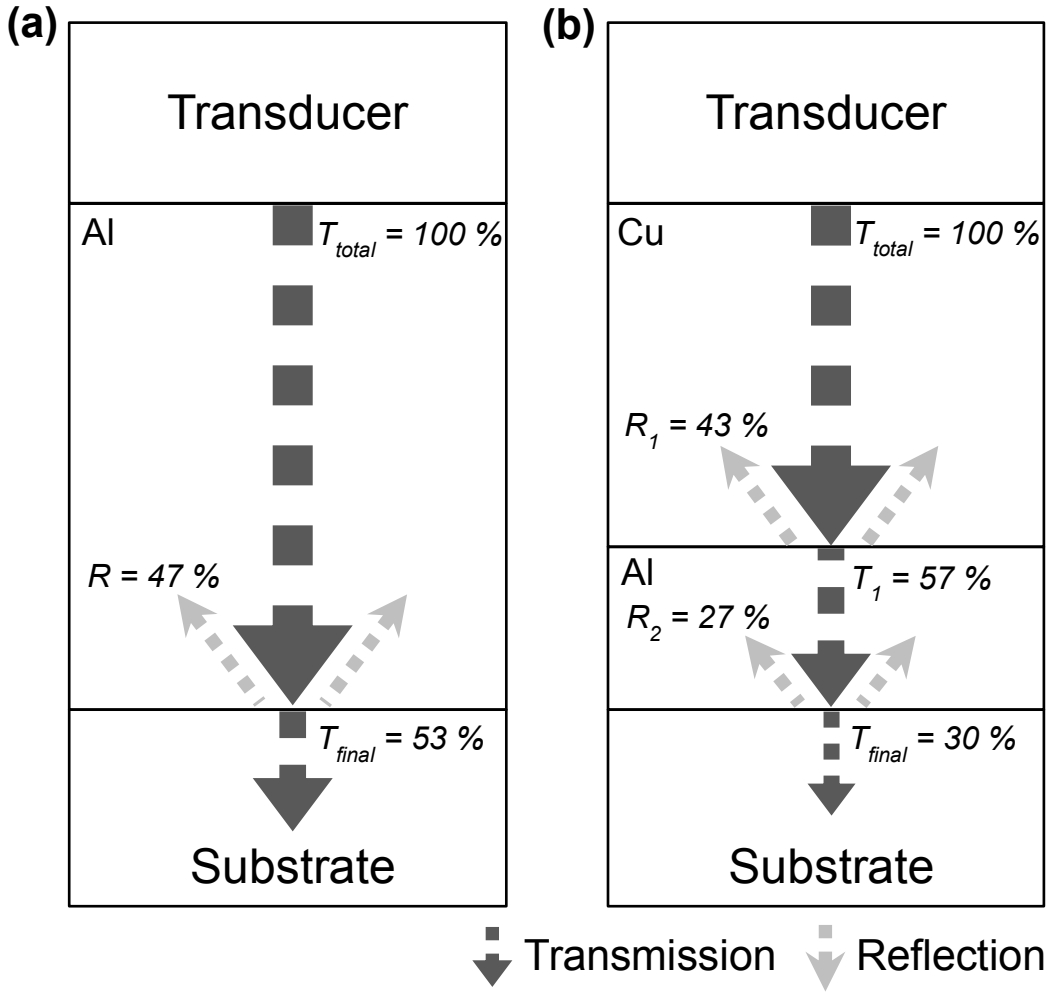

Fig. 3.2 Ultrasound wave transfer with regard to interface reflection and transmission; comparison of (a) Al ribbon and (b) Cu/Al clad ribbon bonding.

Table 3.2 Suitable bonding parameters of the Al and Cu/Al clad ribbon wirings

Bonding parameters	Al ribbon	Cu/Al clad ribbon
Ultrasonic power (W)	20	150
Bonding time (s)	2.0	0.5
Normal bonding force (N)	18.5	34.3
Ultrasonic frequency (kHz)	60	76

3.3.2 Mechanical strength and heel crack propagation

The mechanical stabilities of ribbon wirings are usually evaluated by pull testing [14–16]. In the present work, the mechanical strengths of the Al ribbon and Cu/Al ribbon wirings were compared under each harsh test period. In both cases, no lift-off phenomenon was observed at ribbon joints, indicating successful bonding. The initial rupture forces of the Al ribbon and Cu/Al ribbon manufactured under optimal bonding conditions are 27.4 N and 38.0 N, respectively. Independent of the test conditions, the rupture force of the Cu/Al clad ribbon wirings was always higher than that of the Al ribbon wirings. The pull fractures of the Al and Cu/Al clad ribbons occurred around the first ribbon bond heel. **Figs. 3.3** and **3.4** compare the pull strength and heel crack propagation around the ribbon heel under each harsh test condition. During a thermal exposure test at 200 °C, as shown in **Fig. 3.3**, the rupture force of the Al ribbon decreases gradually until the first 1000 h and saturates from 1000 to 2000 h because the crack propagates along the Al/substrate interface. In contrast, the rupture force of the Cu/Al clad ribbon does not change significantly over the first 1000 h, but then decreases from 1000 h to 2000 h. During thermal shock test at -40/250 °C, as shown in **Fig. 3.4**, the rupture force of the Al ribbon decreased steadily from 0 to 1000 cycles and saturated to 2000 cycles. Whereas the rupture force of the Cu/Al clad ribbon strongly decreased from 0 to 1000 cycles and saturated towards 2000 cycles because the heel crack reached the Cu-Al IMCs and propagated along the IMC layers. The peak temperature of the heat cycling is higher

than that of the temperature storage and is caused by Al grain coarsening leading to severe heel crack propagation.

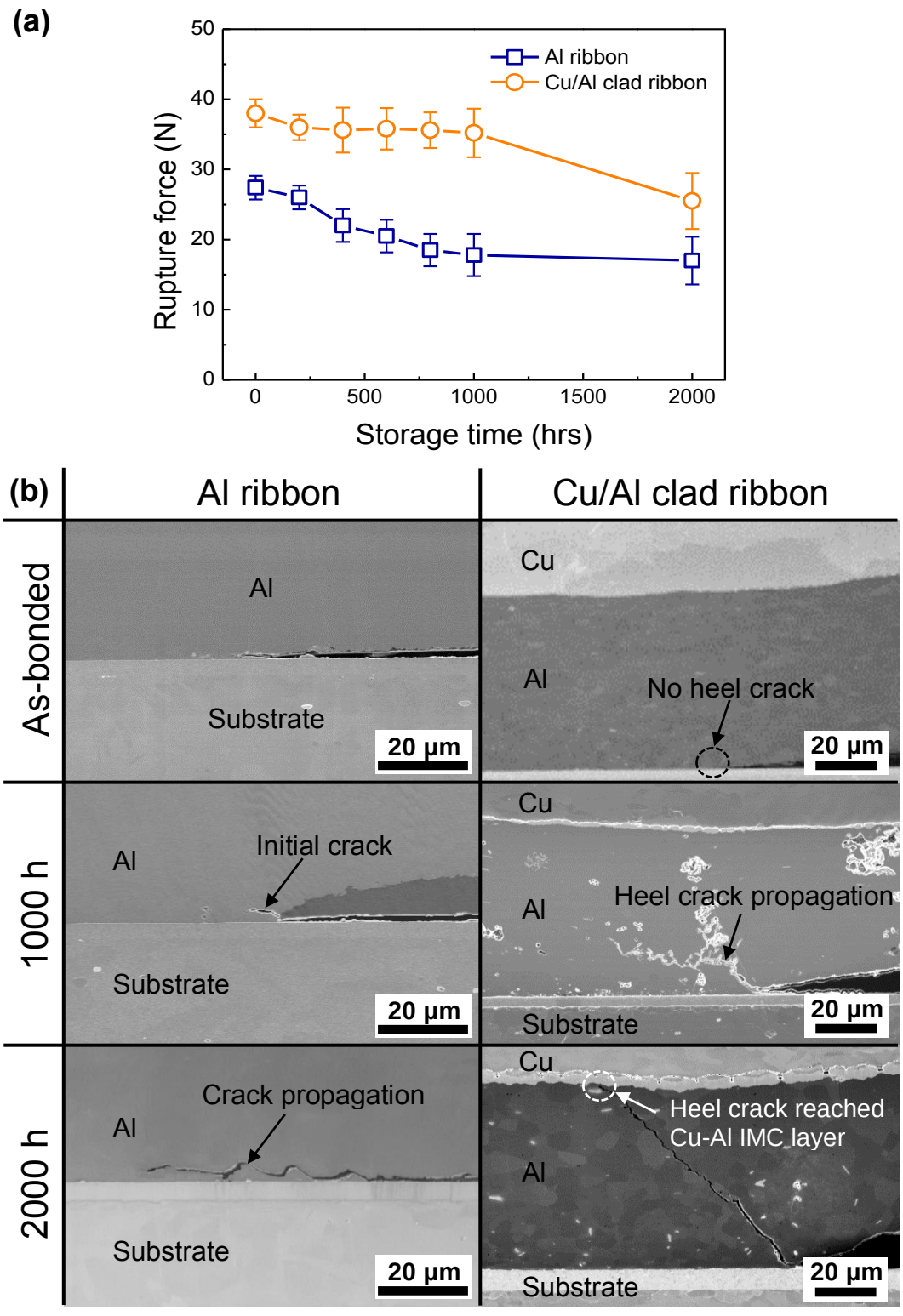

Fig. 3.3 (a) Pull strength degradation of the Al and Cu/Al clad ribbon wirings after thermal exposure testing at 200 °C and (b) FE-SEM images showing the tendency of heel crack propagation.

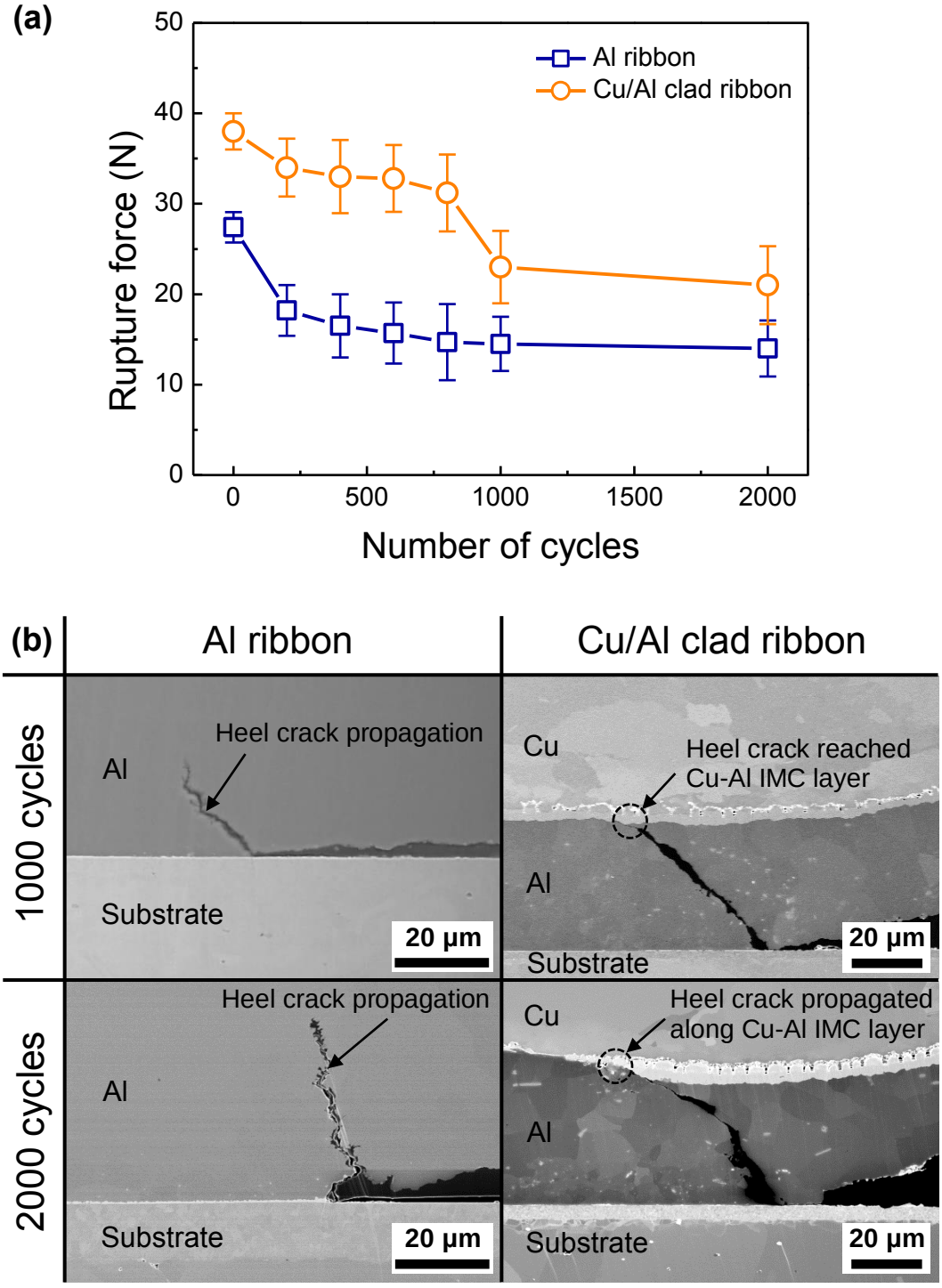

Fig. 3.4 (a) Pull strength degradation of the Al and Cu/Al clad ribbon wirings after thermal shock testing at -40/250 °C and (b) FE-SEM images showing the tendency of heel crack propagation.

The Al microstructure evolution during harsh tests was analyzed by electron backscatter diffraction (EBSD), as shown in **Figs. 3.5** and **3.6**. The average grain size of Al increased with longer test periods. The grain size of thermal-shocked samples is larger than that of thermal-exposed samples because the highest temperature influences the coarsening of the Al grain. The Al average grain sizes of Cu/Al clad ribbon were smaller than those of the Al ribbon during each thermal test. Relatively small Al grains of the Cu/Al clad ribbon with cold rolling process inhibit the heel crack propagation between grain boundaries. Therefore, higher joint stability can be obtained by the use of Cu/Al clad ribbons over Al ribbons in power device interconnections.

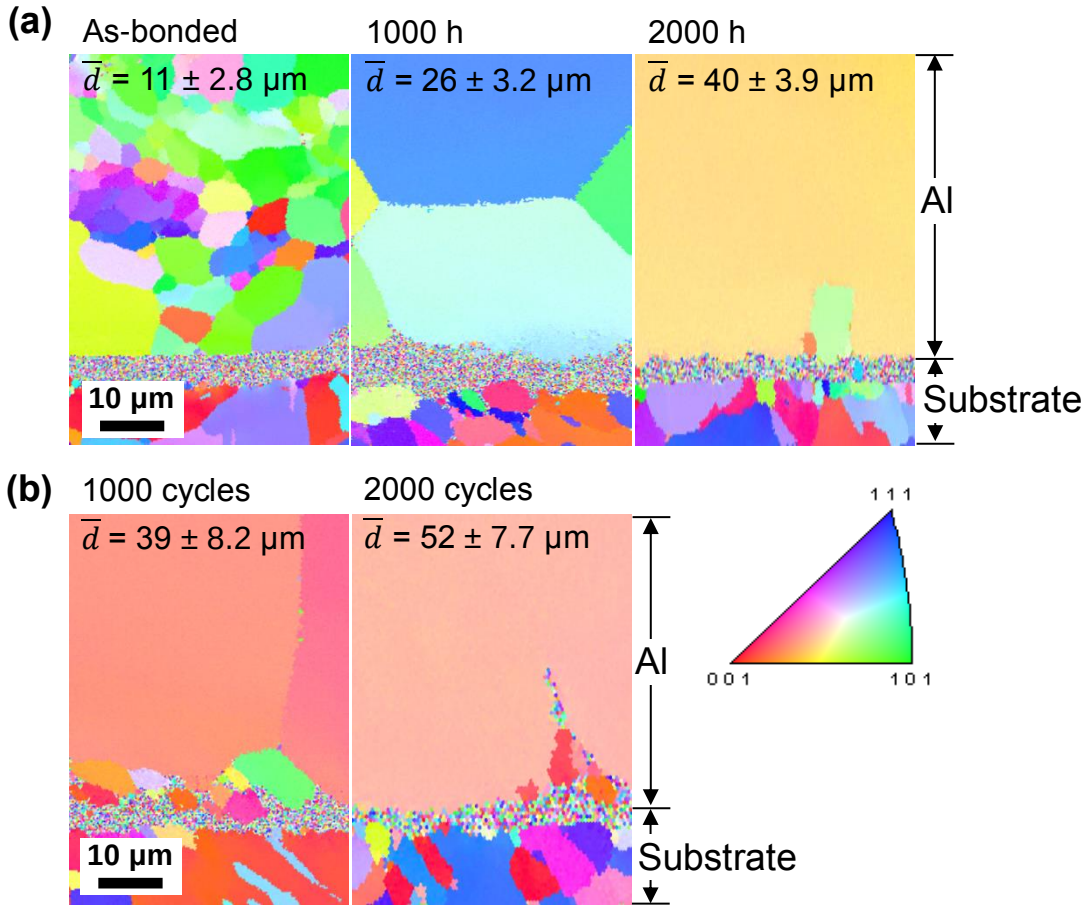

Fig. 3.5 Microstructural evolution in Al ribbon wirings by grain coarsening at the bond interface near the ribbon heel. Inverse pole figure (IPF) maps analyzed by EBSD after (a) thermal exposure testing at 200 °C and (b) thermal shock testing at -40/250 °C. $\overline{d}$ denotes the average diameter of the Al grains. The legend of the IPF maps is shown at the bottom right corner.

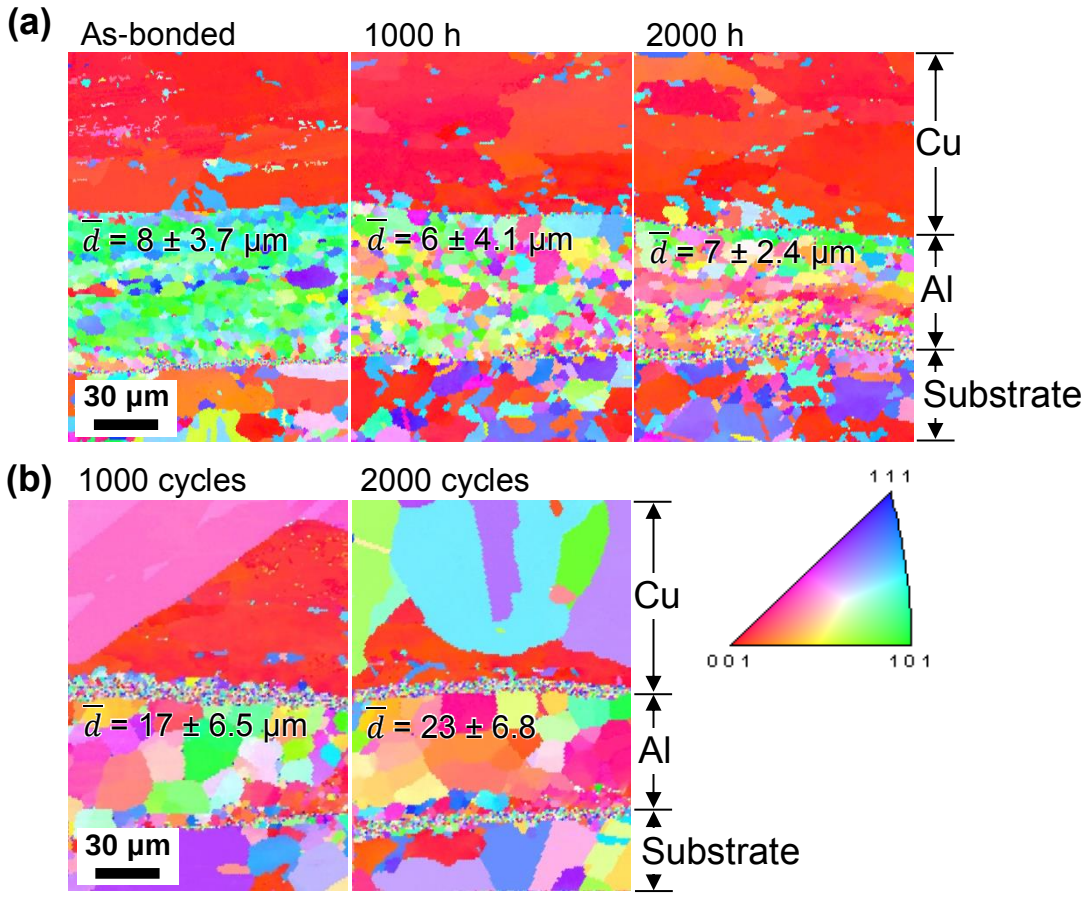

Fig. 3.6 Microstructural evolution in Cu/Al clad ribbon wirings by grain coarsening at the bond interface near the ribbon heel. Inverse pole figure (IPF) maps analyzed by EBSD after (a) thermal exposure testing at 200 °C and (b) thermal shock testing at -40/250 °C. $\overline{d}$ denotes the average diameter of the Al grains. The legend of the IPF maps is shown at the bottom right corner.

3.3.3 IMCs formation and fracture mode of Cu/Al clad ribbon

Heel crack propagation reached the Cu-Al IMCs through the Al layer during harsh tests, and severe IMC growth occurred after thermal shock cycling. The IMC growth influences the mechanical stability because the heel cracks propagate toward the Cu-Al IMCs. IMC formation is important to understanding the fracture modes. The images of bond and clad interfaces and their results of quantitative elemental analysis from the Cu layer to the substrate are presented in **Figs. 3.7**–**3.9**. The heel crack cannot be clearly observed in the as-bonded specimen, as shown in **Fig. 3.7a**. The result of elemental analysis line from the Cu layer to substrate is represented in **Fig. 3.7b**. Various phases of Cu-Al IMCs are formed by high-

temperature diffusion [17–22]. As observed in **Fig. 3.7c**, γ_1-Cu_9Al_4, ζ_2-Cu_4Al_3, and θ-$CuAl_2$ are formed between the Cu and Al layers, where the combined IMC thickness is 0.6 μm after the rolling process during annealing at 100 °C. As observed in **Fig. 3.7d**, the ternary mixed phases of Al-Au-Ni at the bonded interface are formed by ultrasonic oscillation due to the friction energy during ultrasonic ribbon bonding [23–25].

The heel crack is clearly observed within the Al layer and almost propagates to the Cu-Al IMCs after the thermal exposure test, as shown in **Fig. 3.8a**. The result of elemental analysis line from the Cu layer to substrate is represented in **Fig. 3.8b**. The combined thickness of the IMC phases of δ-Cu_3Al_2, η_2-CuAl, and θ-$CuAl_2$ is 2.5 μm after 2000 h, as observed in **Fig. 3.8c**. During the thermal exposure test at 200 °C, δ-Cu_3Al_2 and η_2-CuAl were revealed with increasing Al at.% due to the faster diffusion rate of Al in Cu compared with that of Cu in Al. The thickness of the Al_3Ni_2 layer is 200 nm, and voids are specifically observed at the bonded interface after 2000 h, as shown in **Fig. 3.8d**. Interdiffusion between Al atoms and Ni atoms at the bonded interface occurred during high-temperature storage test [17, 26].

Severe heel crack propagation, which reaches the Cu-Al IMCs within the clad interface during thermal shock cycling, is observed in **Fig. 3.9a**. The result of elemental analysis line from the Cu layer to substrate is represented in **Fig. 3.9b**. An interfacial crack is also observed at the bonded interface. The combined thickness of the IMCs formed at the clad interface, namely γ_1-Cu_9Al_4, η_2-CuAl, and θ-$CuAl_2$, is 7.5 μm after 2000 cycles, as observed in **Fig. 3.9c**. The voids are also indicated between Cu-Al IMC layers. The thickness of the Cu-Al IMCs after thermal shock at -40/250 °C is greater than that of the thermally exposed samples at 200 °C due to the highest temperature used. At the bonded interface and after 2000 cycles, as observed in **Fig. 3.9d**, the Al_3Ni layer is thicker (500 nm) than that of the thermally exposed sample because the high temperature influences the diffusion rate.

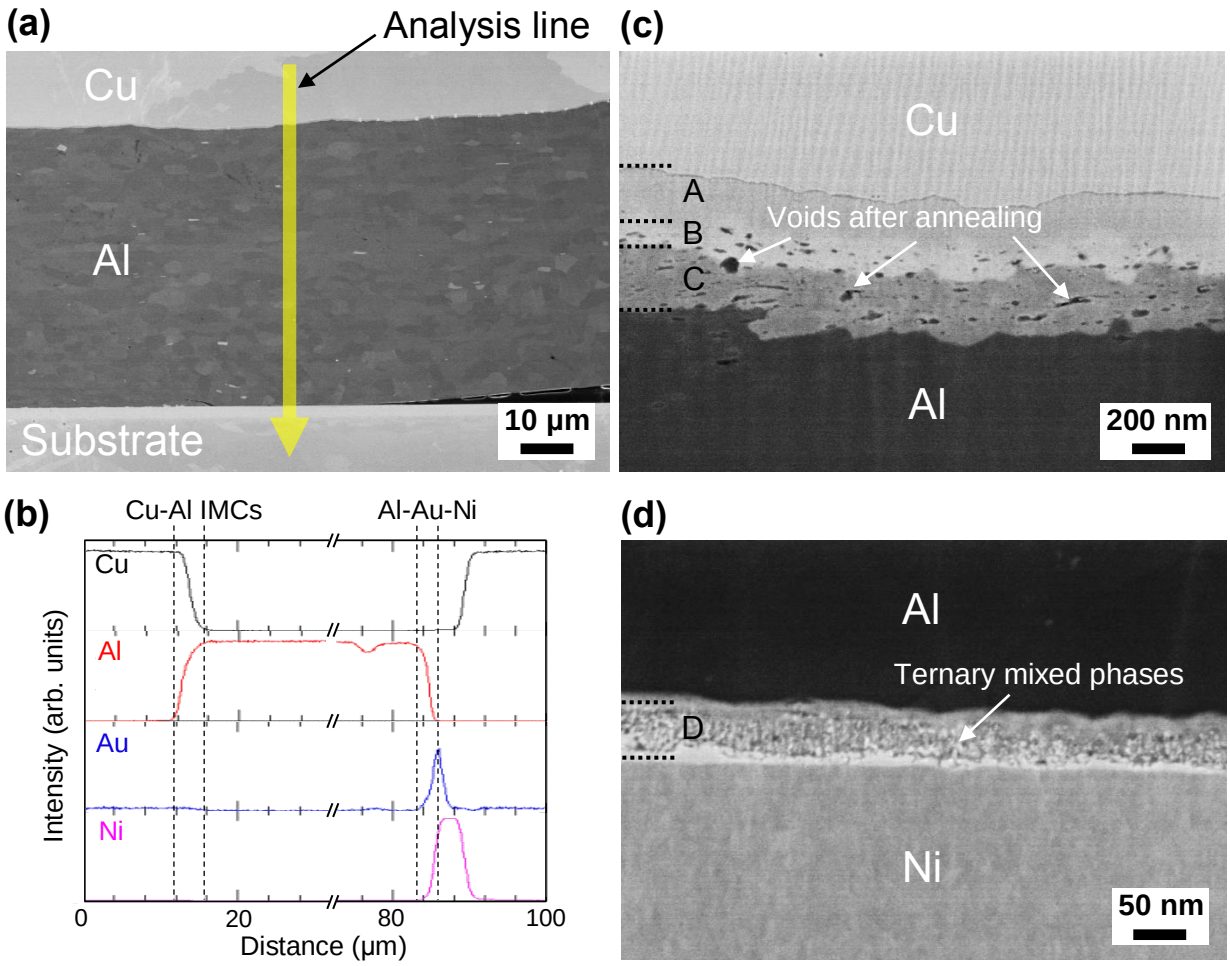

Region	Thickness	Cu at.%	Al at.%	Ni at.%	Au at.%	Phase
A	< 0.2 μm	66.8	33.1	-	-	γ_1-Cu_9Al_4
B	< 0.1 μm	56.2	43.7	-	-	ζ_2-Cu_4Al_3
C	< 0.3 μm	32.2	67.8	-	-	θ-$CuAl_2$
D	< 0.06 μm	-	Unquantifiable			Ternary mixed

Fig. 3.7 IMC identification in the Cu/Al clad ribbon wiring in the as-bonded specimen: (a) FE-SEM image at the ribbon heel, (b) elemental analysis line from the Cu layer to the substrate, (c) at the clad interface, and (d) at the bond interface. Quantitative analysis results within the IMCs are shown at the bottom diagram.

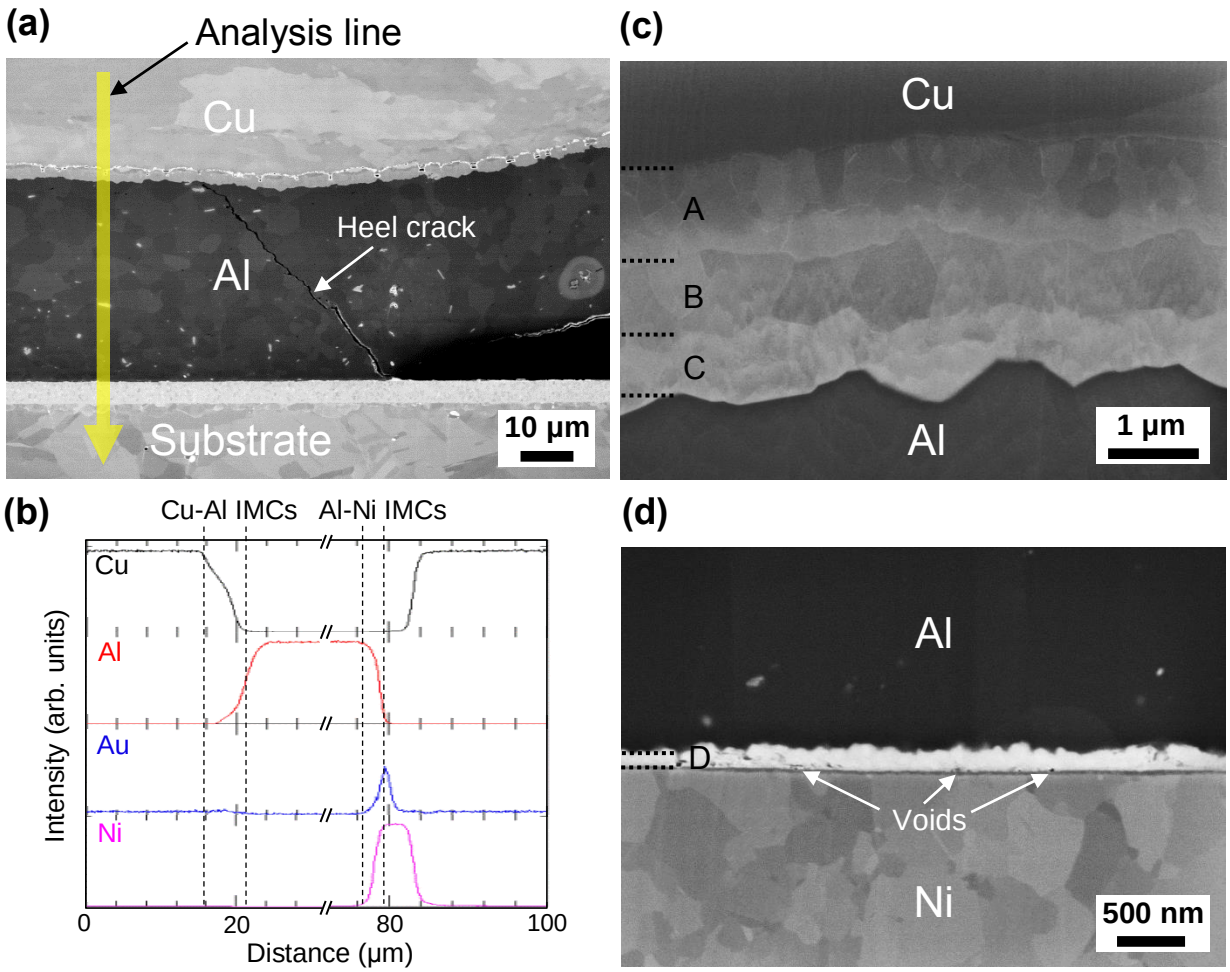

Region	Thickness	Cu at.%	Al at.%	Ni at.%	Au at.%	Phase
A	~ 1.1 μm	59.9	40.0	-	-	δ-Cu_3Al_2
B	~ 0.8 μm	49.9	50.0	-	-	η_2-CuAl
C	~ 0.6 μm	32.9	67.0	-	-	θ-$CuAl_2$
D	~ 0.2 μm	-	59.1	38.1	2.7	Al_3Ni_2

Fig. 3.8 IMCs growth and identification in the Cu/Al clad ribbon wiring after 2000 h thermal storage: (a) FE-SEM image at the ribbon heel, (b) elemental analysis line from the Cu layer to substrate, (c) at the clad interface, and (d) at the bond interface. Quantitative analysis results within the IMCs are shown in the bottom diagram.

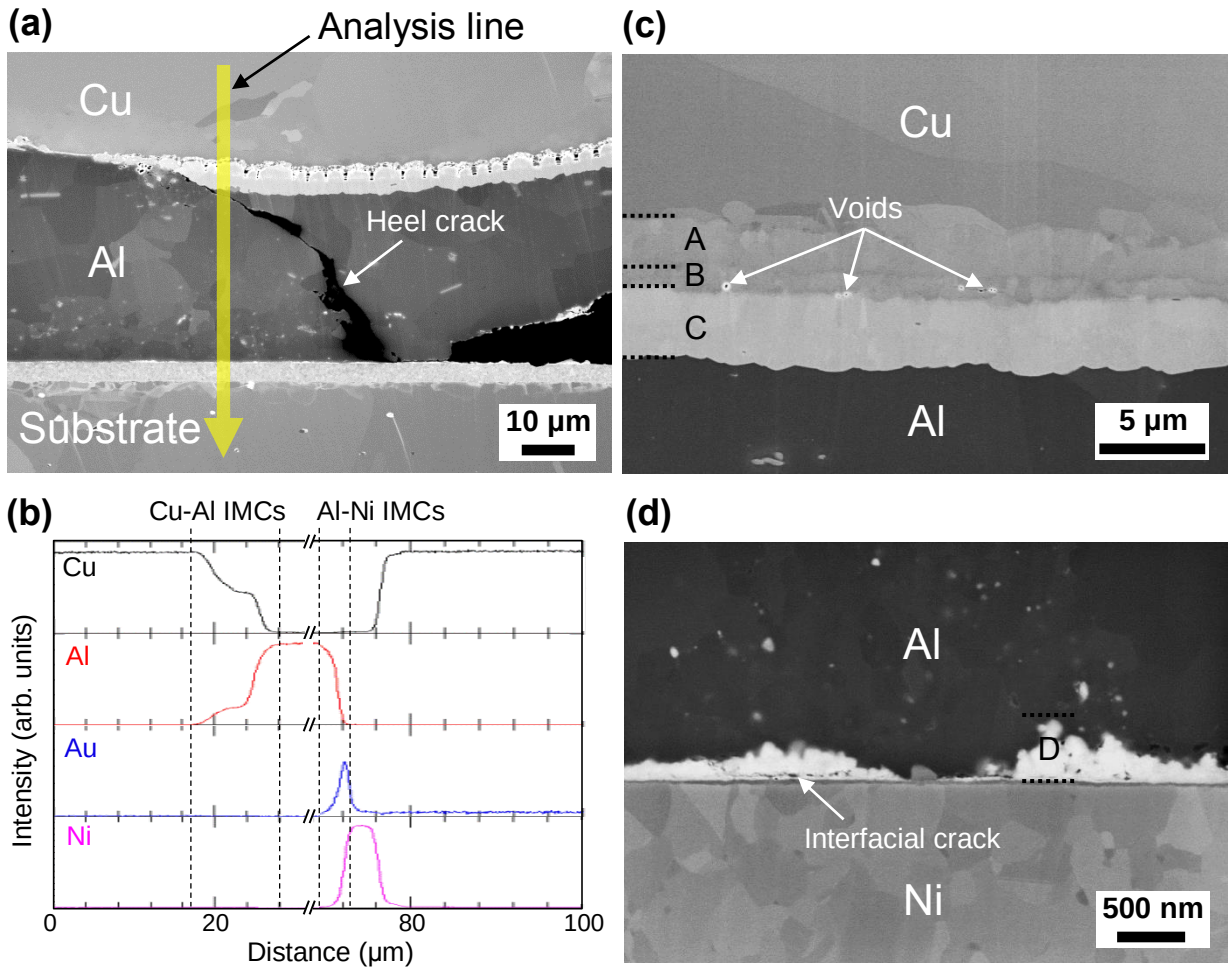

Region	Thickness	Cu at.%	Al at.%	Ni at.%	Au at.%	Phase
A	~ 2.8 μm	66.8	33.1	-	-	γ_1-Cu_9Al_4
B	~ 0.7 μm	49.9	50.0	-	-	η_2-CuAl
C	~ 4.0 μm	32.0	67.9	-	-	θ-$CuAl_2$
D	~ 0.5 μm	-	68.8	28.0	3.0	Al_3Ni

Fig. 3.9 IMCs growth and identification in the Cu/Al clad ribbon wiring after 2000 thermal shock cycles: (a) FE-SEM image at the ribbon heel, (b) elemental analysis line from the Cu layer to substrate, (c) at the clad interface, and (d) at the bond interface. Quantitative analysis results within the IMCs are shown at the bottom diagram.

The weakest region observed by pull testing was the Cu-Al IMCs. All pull fractures of the Cu/Al clad ribbon occurred at the Cu-Al IMC layers within the clad interfaces regardless of the highest temperature and test duration, whereas pull fractures of the Al ribbon occurred at the ribbon loop. We focused on the fracture surface of Cu/Al clad ribbons. The pull fracture surfaces and the elemental mapping results of the as-bonded, thermally exposed, and thermally shocked specimens are shown in **Fig. 3.10**. The elemental quantity levels of Al and Cu were observed to be different depending on each specimen. The fracture surface of the as-bonded specimen was revealed to be an Al-rich phase. The Cu-rich phase was revealed with increased thickness of Cu-Al IMC during thermally harsh tests. The IMCs at the fracture surface were θ-$CuAl_2$ (as-bonded), δ-Cu_3Al_2 (thermally exposed), and γ_1-Cu_9Al_4 (thermally shocked), respectively. The IMC thickness of the thermally shocked specimen was greater than that of the thermally exposed specimen. This means that the mechanical strength degradation is influenced by severe Cu-Al IMC growth at highest temperature, because voids and cracks are formed at the Cu-Al IMCs by thermal diffusion. Consequently, the mechanical strength degradation of Cu/Al clad ribbon wirings is caused by increasing the IMC thickness at the clad interface because the IMCs are brittle.

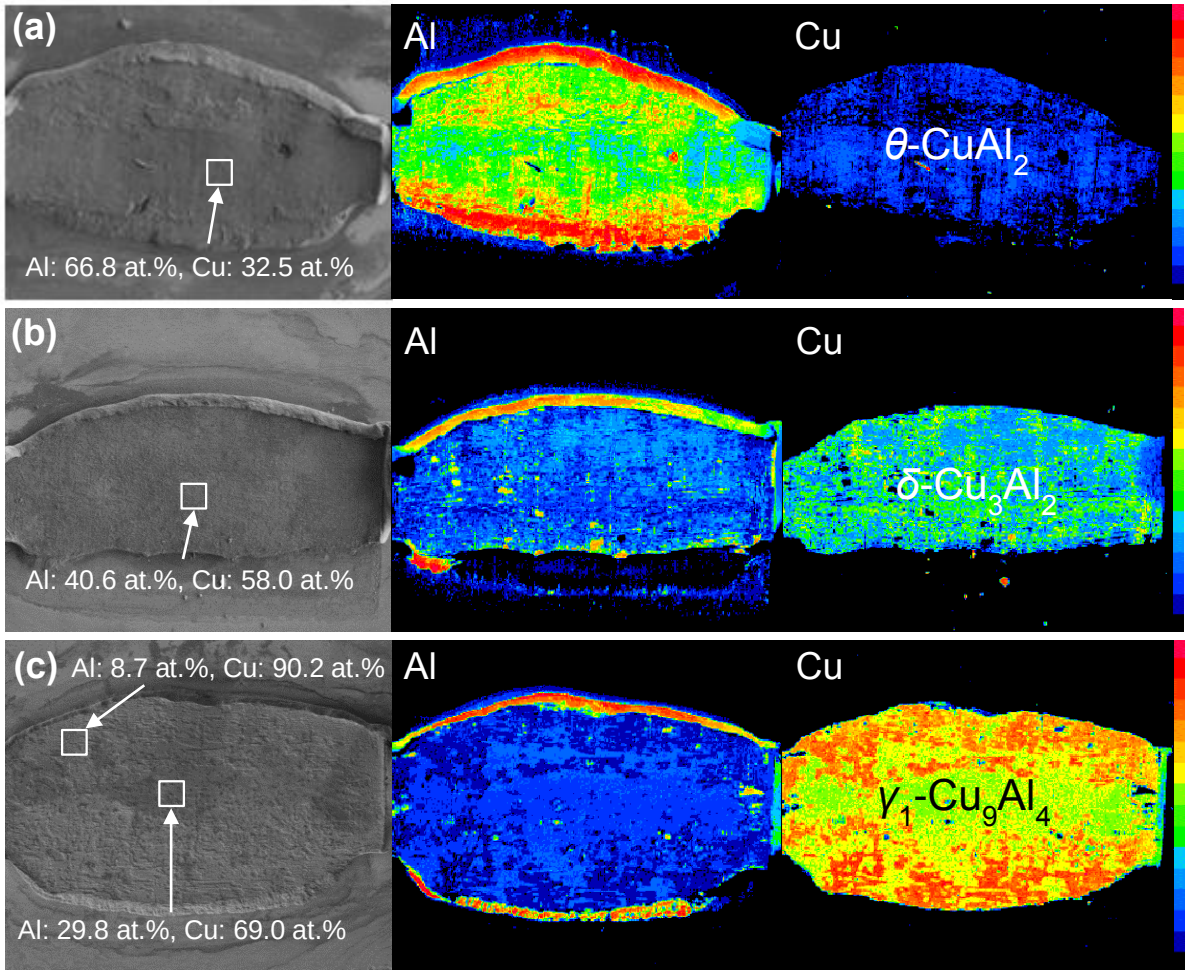

Fig. 4.10 EPMA reveals different IMC phases on the fracture surface after pull test: (a) as-bonded, (b) thermal exposure test after 2000 h, and (c) thermal shock test after 2000 cycles.

3.4 Conclusions

Microstructural evolution in Al and Cu/Al clad ribbons for high-temperature storage at 200 °C and thermal shock cycling at -40/250 °C was reported, and the mechanical stabilities in the two thermal tests were compared with respect to heel crack propagation by grain coarsening. The heel cracks were initiated between the edge of the bonded interface and the ribbon loop. Heel crack propagations occurred due to Al grain coarsening during high-temperature storage and cycling conditions, which lead to degradation of mechanical stability. The mechanical strength of Cu/Al clad ribbon wiring was higher than that of Al ribbon wiring regardless of the test conditions. The Cu-Al IMCs influenced the enhancement of mechanical stability because a certain IMC thickness interrupts heel crack propagation. All Al ribbon fractures occurred at the ribbon loop whereas Cu/Al clad ribbon fractures occurred at the Cu-Al IMCs regardless of the high temperature and test duration. The Cu-Al IMCs on the fracture surface were observed to be different depending on each specimen, the main compositions of which were indicated as θ-$CuAl_2$ (as-bonded), δ-Cu_3Al_2 (thermally exposed), and γ_1-Cu_9Al_4 (thermally shocked). In the present work, we concluded that the mechanical stability of the Cu/Al clad ribbons is superior to that of the Al ribbons with respect to the investigation of heel crack propagation by grain coarsening even in high-temperature tests.

References

[1] Y. Celnikier, L. Benabou, L. Dupont, G. Coquery, Investigation of the heel crack mechanism in Al connections for power electronics modules, Microelectronics Reliability 51 (2011) 965–974.

[2] X. Liu, G. Lu, Power Chip Interconnection: From Wirebonding to Area Bonding, The International Journal of Microcircuits and Electronic Packaging 23 (2000) 407–413.

[3] A. Shah A, H. Gaul H, M. Schneider-Ramelow M, H. Reichl, M. Mayer, Y. Zhou, Ultrasonic friction power during Al wire wedge-wedge bonding. Journal of Applied Physics 106 (2009) 013503.

[4] M. Ciappa, Selected failure mechanisms of modern power modules, Microelectronics Reliability 42 (2002) 653–667.

[5] Y. Yamada, Y. Takaku, Y. Yagi, I. Nakagawa, T. Atsumi, M. Shirai, I. Ohnuma, K. Ishida, Reliability of wire-bonding and solder joint for high temperature operation of power semiconductor device Microelectronics Reliability 47 (2007) 2147–2151.

[6] S. Ramminger, N. Seliger, G. Wachutka, Reliability Model for AI Wire Bonds subjected to Heel Crack Failures, Microelectronics Reliability 40 (2000) 1521–1525.

[7] R. Pelzer, M. Nelhiebel, R. Zink, S. Wohlert, A. Lassnig, G. Khatibi, High temperature storage reliability investigation of the Al–Cu wire bond interface, Microelectronics Reliability 52 (2012) 1966–1970.

[8] H. Xu, C. Liu, V.V. Silberschmidt, S.S. Pramana, T.J. White, Z. Chen, V.L. Acoff, Behavior of aluminum oxide, intermetallics and voids in Cu–Al wire bonds, Acta Materialia 2011;59:5661–73.

[9] H. Xu, C. Liu, V.V. Silberschmidt, S.S. Pramana, T.J. White, Z. Chen, M. Sivakumar, V.L. Acoff, A micromechanism study of thermosonic gold wire bonding on aluminum pad, Journal of Applied Physics 108 (2010) 113517.

[10] H. Clauberg, P. Backus, B. Chylak, Nickel-palladium bond pads for copper wire bonding, Microelectronics Reliability 51 (2011) 75–80.

[11] C. Biasotto, L. B. Isoda, C. S. Franco, N. Armigliato, Evaluation of low cost metallization process for power electronics module by wire wedge bond process on Nickel/Copper and Nickel/Copper/Silver pads, ECS Transactions 39(1) (2011) 385–392.

[12] S. Hoche, M.A. Hussein, T. Becker, Ultrasound-based density determination via buffer rod techniques: a review, Journal of Sensors and Sensor Systems 2 (2012) 103–125.

[13] A.A. Mohammed, S.M. Haris, M.Z. Nuawi, Using the pressure transmission coefficient of a transmitted wave to evaluate some of the mechanical properties of refractory metals. Ultrasonics 55 (2015) 133–140.

[14] S. Mazzei, M. Madia, S. Beretta, A. Mancaleoni, S. Aparo, Analysis of Cu-wire pull and shear test failure modes under ageing cycles and finite element modelling of Si-crack propagation. Microelectronics Reliability 53 (2014) 2501–2512.

[15] M.G. Pecht, A. Zhong, A. Choubey, P.S. Chauan, Copper Wire Bonding, 1st ed. New York, Springer, 2014.

[16] R. Dohle, M. Petzold, R. Klengel, H. Schulze, F. Rudolf, Room temperature wedge-wedge ultrasonic bonding using aluminum coated copper wire, Microelectronics Reliability 51 (2011) 97–106.

[17] H. Kim, S. Kim, J. Lee, M. Choi, S. Choe, K. Kim, J. Ryu, S. Kim, S. Han, W. Kim, S. Lim, Microstructural evaluation of interfacial intermetallic compounds in Cu wire bonding with Al and Au pads, Acta Materialia 64 (2014) 356–366.

[18] H. Kim, J. Lee, K. Paik, K. Koh, J. Won, S. Choe, J. Lee, J. Moon, Y. Park, Effects of Cu/Al Intermetallic Compound (IMC) on Copper Wire and Aluminum Pad Bondability, IEEE Transactions on Components and Packaging Technologies 26(2) (2003) 367–374.

[19] S. Gueydan, B. Domenges, E. Hug, Study of the intermetallic growth in copper-clad aluminum wires after thermal aging, Intermetallics 50 (2014) 34–42.

[20] I. Bae, D. Jung, W. Chen, Y. Du, Intermetallic compound formation at Cu-Al wire bond interface, Journal of Applied Physics 112 (2012) 123501.

[21] Y. Guo, G. Liu, H. Jin, Z. Shi, G. Qiao, Intermetallic phase formation in diffusion-bonded Cu/Al laminates, Journal of Materials Science 46 (2011) 2467–2473.

[22] T.J.S. Anand, C.K. Yau, Y.S. Leong, L.W. Keat, H.M. Ting, Microstructural and mechanical analysis of Cu and Au interconnect on various bond pads, Current Applied Physics 13 (2013) 1674–1683.

[23] I. Lim, M. Mayer, Y. Zhou, Footprint Study of Ultrasonic Wedge-Bonding with Aluminum Wire on Copper Substrate, Journal of Electronic Materials 35(3) (2006) 433–442.

[24] A. Shah, A. Rezvani, M. Mayer, Y. Zhou, J. Persic, J. Moon, Reduction of ultrasonic pad stress and aluminum splash in copper ball bonding, Microelectronics Reliability 51 (2011) 67–74.

[25] A. Rezvani, A. Shah, M. Mayer, Y. Zhou, J. Moon, Role of impact ultrasound on bond strength and Al pad splash in Cu wire bonding, Microelectronics Reliability 53 (2013) 1002–1008.

[26] Y. Jiang, R. Sun, Y. Yu, Z. Wang, Q. Chen, Formation and Growth of Intermetallic Compounds in Cu–Au and Au–Al Systems for Copper on Gold Bonding, IEEE Transactions on Electronics Packaging Manufacturing 33(3) (2010) 228–235.

Chapter 4

Heel crack propagation mechanism of cold-rolled Cu/Al clad ribbon bonding in harsh environment

4.1 Introduction

Novel ribbon bonding with ultrasonic oscillation has attracted considerable attention as an interconnection technology of next-generation wide-band-gap power electronics because of its capability to pass a large electrical current compared with conventional wire bonding [1–3]. Typical materials for ribbon bonding for power device interconnections are Al and Cu. High-purity Al ribbon has been already used in many applications because of its excellent formability in wiring. However, high-purity Al has several disadvantages such as rapid grain coarsening and relatively low current/heat conductivity during high-temperature operation. There is also a risk of heel crack propagation within Al ribbons [4, 5]. In contrast, Cu offers many advantages compared with Al such as higher electrical and thermal conductivities. However, bare Cu is not easily bonded by conventional ultrasonic bonding primarily because of its hardness. Thus, Cu ribbon wiring usually requires special care such as cladding with Al or the use of a soft material coating to achieve successful bonding. Cold rolling is employed to prepare Cu/Al clad ribbons.

For Cu/Al clad ribbon bonding, a heel crack frequently occurs within an Al layer under a Cu layer even in the ribbon-bonding process. Heel crack propagation must be prevented to achieve mechanical stability; the heel crack propagation is caused by microstructural evolution and textural transition under severe thermal stress in high-temperature operations. The ultrasonic bonding process with high energy plays an important role in the formation of a deformed microstructure both in the Al layer and the substrate. In particular, ultrasonic bonding generates the intense deformation of bonding materials, which is called the ultrasonic softening effect [6, 7]. In addition, other plastic deformation occurs at a loop of a Cu/Al clad ribbon during the lift-up procedure. Under the operation condition of power devices, a substantial temperature rise occurs at the bonded interfaces and wiring loops [8]. Dynamic recrystallization (DRX, i.e., microstructural evolution) results from the severe temperature increase [9–13], and the formation of microstructures leads to grain coarsening and heel cracking. The DRX mechanism can be described by discontinuous dynamic recrystallization (DDRX, i.e., involving

nucleation and grain growth) and continuous dynamic recrystallization (CDRX, i.e., the transformation of sub-grains into grains). The *"discontinuous"* phenomena involve discontinuous sub-grain growth, primary recrystallization, and abnormal grain growth, whereas the *"continuous"* phenomena by dynamic recovery involve sub-grain growth, continuous recrystallization, and normal grain growth [9–13]. Textural transitions should be analyzed to understand the material characteristics of *"discontinuous"* and *"continuous"* phenomena [14–16]. Consequently, the microstructural evolution and textural transitions of a Cu/Al clad ribbon may cause substantial mechanical degradation. Thus, the objective of the present work was to understand the recrystallization mechanism of Cu/Al ribbon under harsh operation conditions. The authors performed thermal acceleration tests under harsh conditions such as thermal exposure (200 °C) and thermal shock (-40/250 °C) on Cu/Al clad ribbon wiring.

4.2 Experimental methods

4.2.1 Materials and ultrasonic bonding process

High-purity Cu (99.99 mass%) and Al (99.99 mass%) clad ribbons were prepared using the cold-rolling process with a deformed reduction rate above 50 %. The Cu/Al clad ribbons were bonded on an ENIG-finished Cu substrate using a flat-form wedge bonding tool, as illustrated in **Fig. 4.1a**. First, the ribbon bond cross-sections indicated in **Fig. 4.1b** were analyzed by scanning electron microscope (SEM) and electron back scatter diffraction (EBSD). The volume fraction of Cu layers within the Cu/Al clad ribbon is 67 %, which is twice that of the Al layers, as shown in **Fig. 4.1c**. The ultrasonic bonding process of Cu/Al clad ribbons was optimized by varying of the ultrasonic power, normal bonding force, and bonding time (**Table 4.1**). Successful Cu/Al clad ribbon bonding requires a higher ultrasonic power and bonding force and a longer time than typical Al ribbon bonding because Cu is hard and has a higher acoustic impedance than Al. The Cu/Al clad ribbon bonding samples were prepared, as shown in **Fig. 4.1d**.

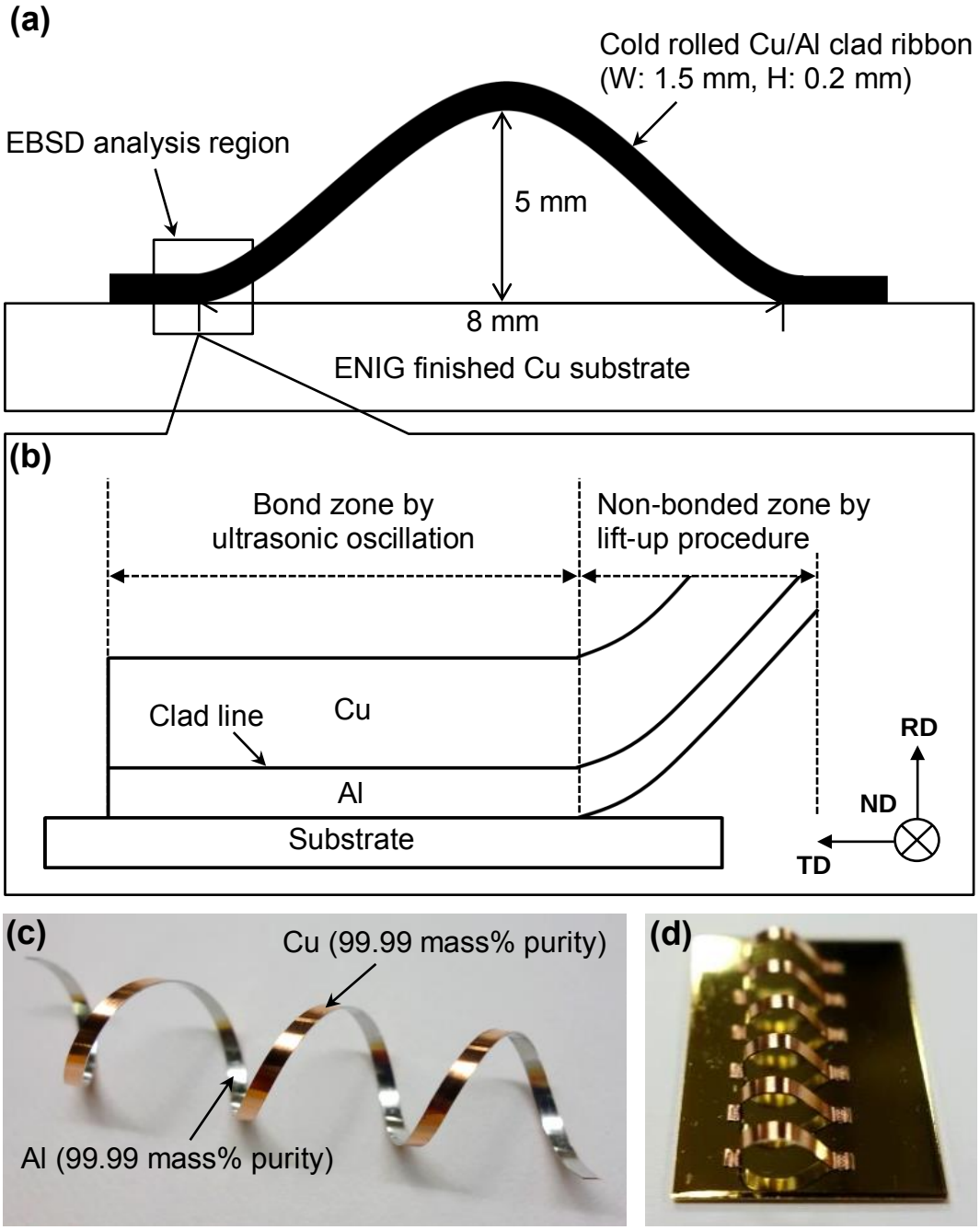

Fig. 4.1 Schematic images: (a) illustration of wiring sample design and (b) close-up view of bonded and non-bonded zones. (c) Cold-rolled Cu/Al clad ribbon and (d) wiring samples for harsh tests.

Table 4.1 Optimized ultrasonic bonding parameters

Bonding parameters	US power (W)	Bonding force (N)	Bonding Time (s)	US frequency (kHz)
Values	150	34.3	0.5	76

4.2.2 Thermal exposure and thermal shock tests

The Cu/Al clad ribbon samples were exposed to harsh environments such as thermal exposure up to 2000 h and thermal shock up to 2000 cycles in air. The temperature profiles are presented in **Fig. 4.2**. Under the operation condition of power devices, the highest temperature above 200 °C occurred at the ribbon joints. When turning on/off the power devices, the temperature change at the ribbon joints is extreme because of the transient heat up/cool down. Thus, we performed thermal acceleration tests such as thermal exposure at 200 °C and thermal shock at -40/250 °C.

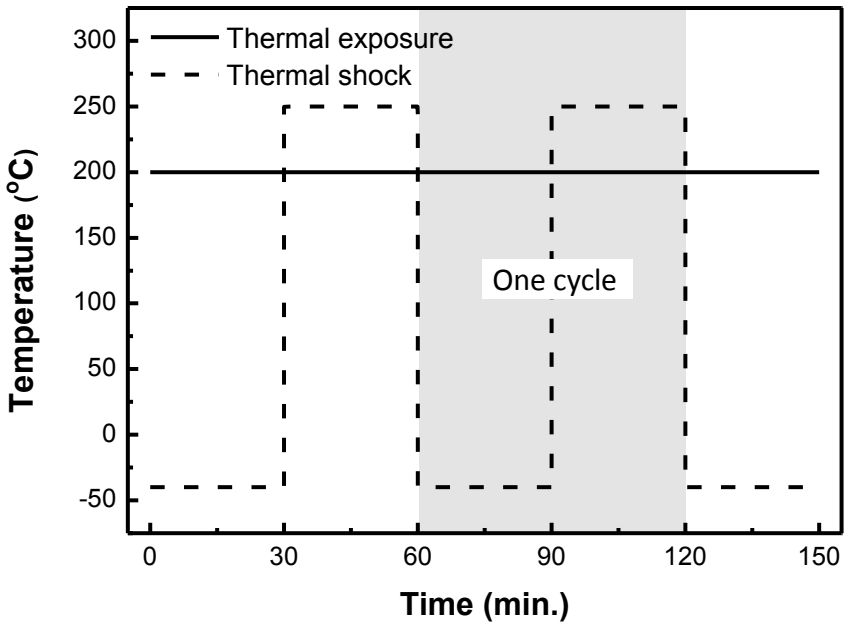

Fig. 4.2 Temperature profiles of harsh environment; thermal exposure test at 200 °C, and thermal shock test at -40/250 °C.

5.2.3 EBSD analysis

The microstructural evolution and textural transition of the Cu/Al clad ribbons were investigated by EBSD analysis. Each cross-section was polished using emery paper and 0.03 μm alumina paste. The samples were finally finished by ion milling to achieve flatness. High-quality electron backscatter diffraction pattern (EBSP) images were obtained using a 20 kV accelerating voltage, 40 mm working distance, and 75 nm beam spot size. Step sizes of 0.5 and 0.8 μm were used, and its shape was a hexagonal pixel. In general, many pixels within one grain should form five to ten grids to reduce errors in the measurement [17]. The step size and confidence index affect the results of the EBSD analysis after data processing [18, 19]. The present step size was small enough to obtain accurate data. In addition, the number of confidence index (CI) above 0.2 was obtained as ideal data with a reliable level of indexing rate above 90 %.

The textural transition and corresponding crystallographic orientation can be obtained by pole figure (PF) and orientation distribution function (ODF) *f(g)* maps. The crystallographic textures were determined by the {111} pole figure, which is a typical plane for evaluating the deformed FCC structure [14, 16]. Subsequently, after correction of the combined PF data with respect to errors such as irradiation and defocusing, the ODF was calculated using the harmonic series expansion method (l_{max} = 16, Gaussian smoothing = 15°); the crystallographic orientations are represented by Bunge Euler angles {φ_1, ϕ, φ_2}. The ODFs were represented using PFs by computing the orthotropic symmetry sample in rolling operations as the rolling direction (RD), transverse direction (TD), and normal direction (ND). The intensity lines in a texture were represented by a constant section of φ_2 ($\Delta\varphi_2$ = 15°) through the adjective Euler angle space ($0° \leq \{\varphi_1, \phi, \varphi_2\} \leq 90°$). Combined information about the microstructural evolution and textural transition was obtained from the harsh tests, and the spatial distribution of several texture components was evaluated by an automated EBSD analysis.

4.3 Results

4.3.1 Verification of EBSPs

EBSD analysis provides many advantages to understand a given crystallographic state and its change. Verification of image quality (IQ) should be performed to obtain ideal data before performing a series of EBSD analysis. An IQ map can typically be used to observe many microstructure features such as different phases, grain boundaries, and surface topologies, as illustrated in **Fig. 4.3**. As observed in **Figs. 4.3c–f**, the IMC layers were observed along the interface of the Cu/Al clad and the bonding interface of the Al/substrate. Both grains of Al and Cu coarsened during the harsh tests. In addition, heel cracks propagated within the Al layer as coarsening Al grains. For the thermal shock test, the average grain size of Al was larger than that for the thermal exposure test (**Table 4.2**).

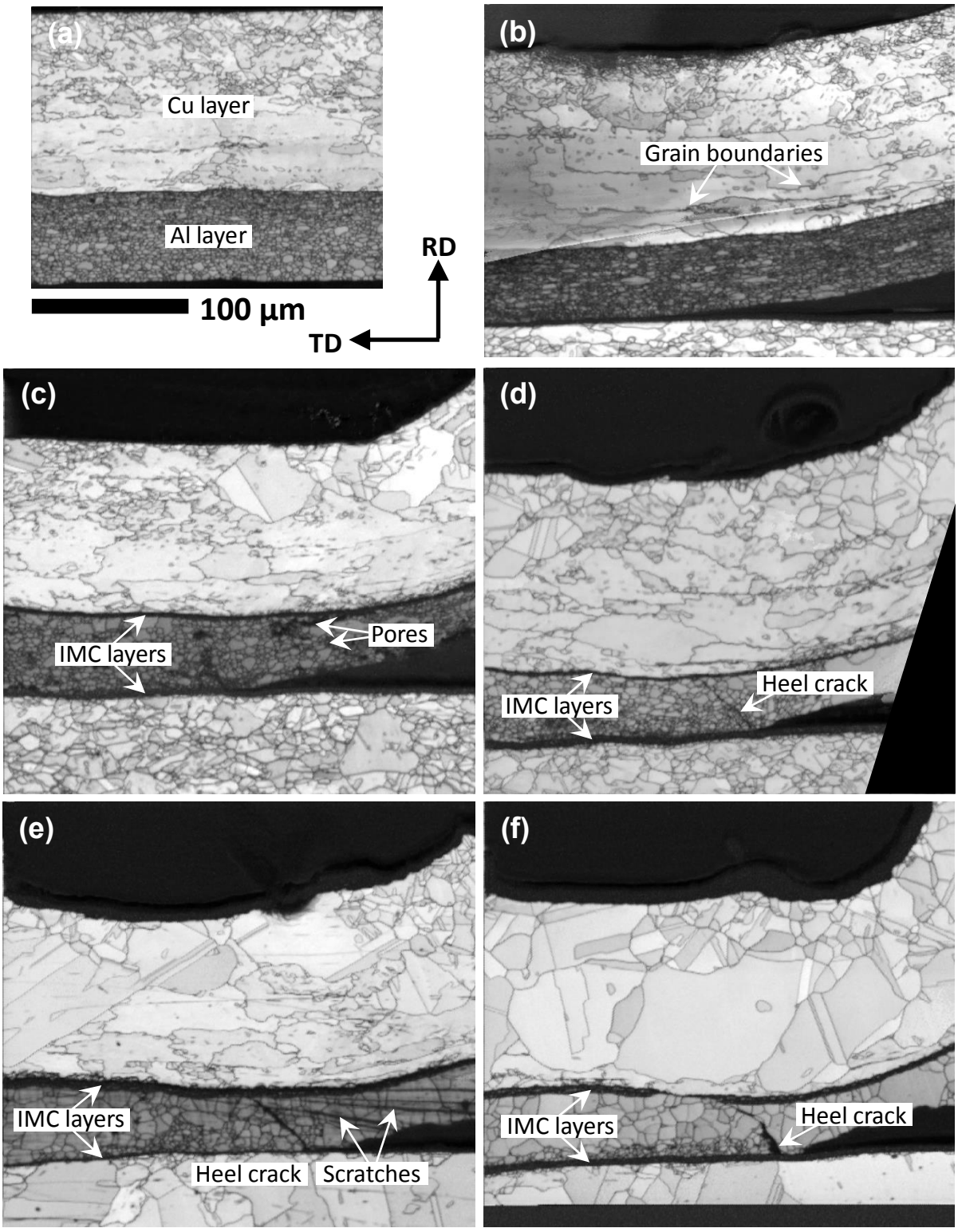

Fig. 4.3 Image quality (IQ) maps. (a) The starting material after the cold-rolling process shows clear Al and Cu layers. (b) As-bonded specimen after ultrasonic bonding, thermal exposure test at 200 °C after (c)1000 h and (d) 2000 h, thermal shock test at -40/250 °C after (e) 1000 cycles and (f) 2000 cycles.

Table 4.2 Average grain size during harsh tests

Specimens	Starting material	As-bonded	After 1000 h	After 2000 h	After 1000 cycles	After 2000 cycles
Average grain size (μm)	8.15	8.35	6.40	7.10	16.90	23.0
Standard deviation	3.71	3.66	4.05	2.41	6.53	6.80

4.3.2 Microstructural evolution

The misorientation angle (θ) bands provide information about the microstructural evolution with respect to deformation and recrystallization during harsh tests [20]. Analysis of the nearest-neighbor pair misorientation angle (θ) distribution was performed for an Al layer within a Cu/Al clad ribbon. **Fig. 4.4** shows variations of the nearest-neighbor pair misorientation angle distributions. The green and blue lines signify low-angle grain boundaries (LAGBs) ($2° \leq \theta \leq 15°$) and high-angle grain boundaries (HAGBs) ($\theta \geq 15°$), respectively. As observed in **Figs. 4.4a** and **b**, fine grain structures (tangled grain boundaries) within the Al layer are introduced by deformation during the cold-rolling and ultrasonic bonding processes. During the harsh tests, CDRX grains are formed by dynamic recovery, where boundaries are overlaid with LAGBs. In contrast, DDRX grains are formed by primary recrystallization, the formation of which indicates the presence of HAGB cells. The fraction of HAGBs decreased with increasing harsh test periods, as observed in **Fig. 4.5**. The reduction of the HAGB fraction indicates a DDRX decrease and CDRX increase. The CDRX and DDRX regions were divided based on their grain orientation spread (GOS) values to understand the microstructural evolution in detail.

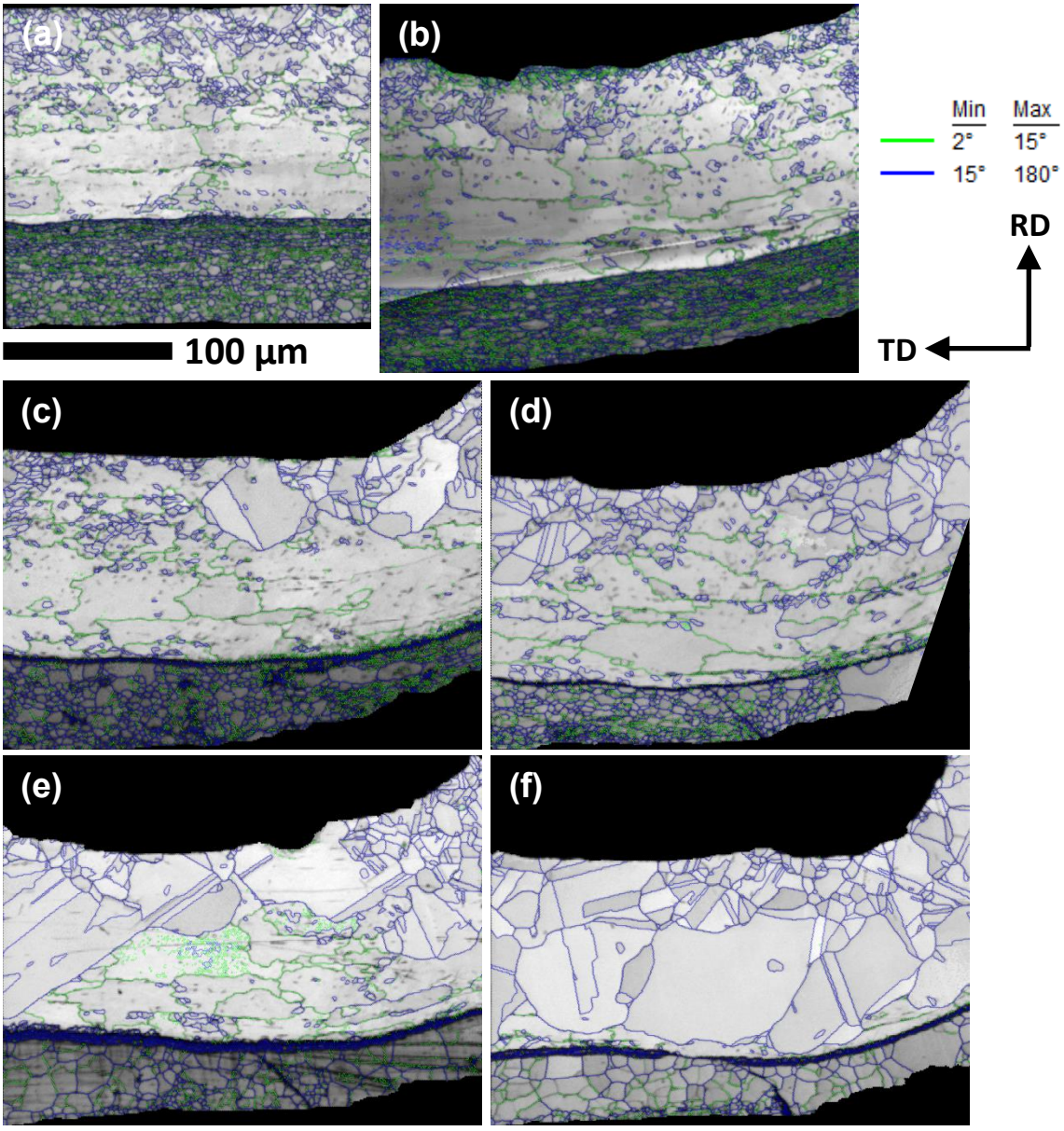

Fig. 4.4 Band contrast (BC) maps overlaid with misorientation angle distribution maps showing the microstructural evolution of cold-rolled Cu/Al clad ribbons during harsh tests. (a) Starting material, (b) as-bonded specimen, thermal exposed at 200 °C after (c) 1000 h and (d) 2000 h, thermal shocked test at -40/250 °C after (e) 1000 cycles and (f) 2000 cycles. The key for the misorientation angle is shown at the top right corner.

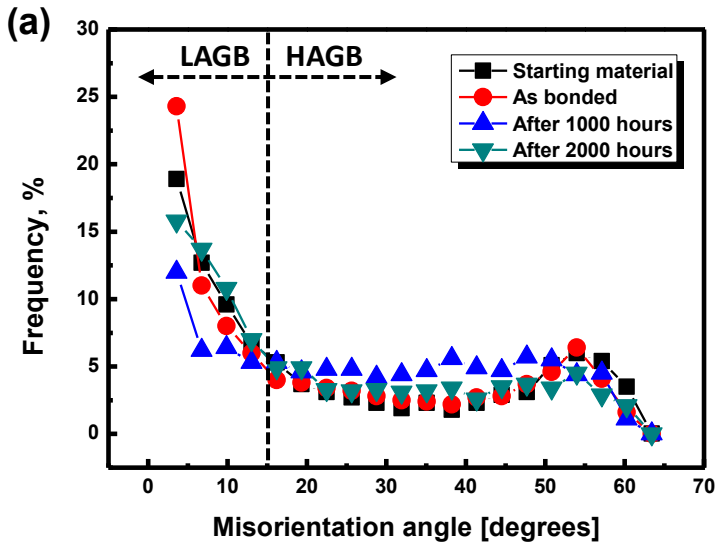

	Starting material	As-bonded	After 1000 h	After 2000 h
$\theta \geq 15^{o}$	53.2 %	53.3 %	52.5 %	40.5 %

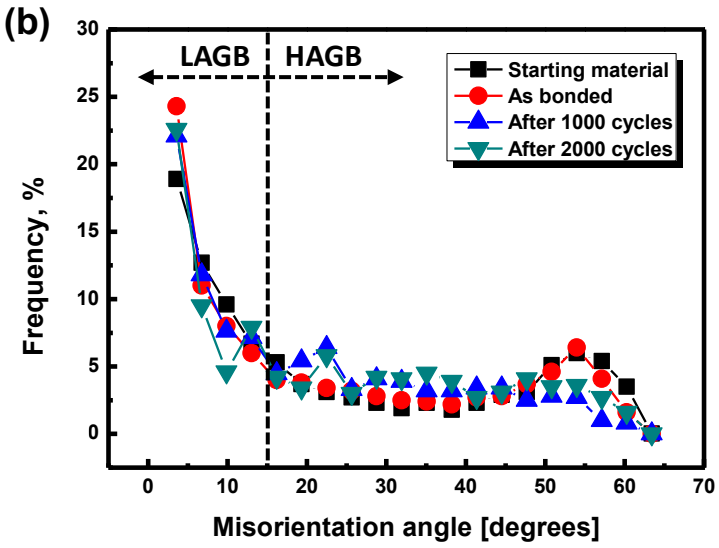

	Starting material	As-bonded	After 1000 cycles	After 2000 cycles
$\theta \geq 15^{o}$	53.2 %	53.3 %	53.2 %	48.8 %

Fig. 4.5 Diagrams of frequency depending on the misorientation angle distribution each harsh test. The fraction of HAGBs is indicated at the bottom of each diagram: (a) thermal exposure test and (b) thermal shock test.

GOS represents the average deviation of crystalline orientations among all the scan points in one grain. This methodological approach leads to assigning a single GOS value to every grain [21–23]. A GOS value of 3° was observed to be the boundary determining deformed and recrystallized grains, i.e., CDRX (GOS ≥ 3°) and DDRX (GOS ≤ 3°), respectively. Dynamic recrystallized grains (involving the CDRX and DDRX grains) were grouped together within an Al layer in all the GOS maps, as observed in **Fig. 4.6**. The fraction of CDRX regions decreased after 1000 h and 1000 cycles and increased until 2000 h and 2000 cycles, as observed in **Fig. 4.7**. This phenomenon appears to be caused by enhanced dynamic recovery within recrystallized grains. The dynamic recovery involves new sub-grain formation within recrystallized grains, which is formed by residual strain in high-dislocation-density regions. The dislocation density concerning average misorientation between neighboring scan points is calculated using the kernel average misorientation (KAM) method, which is similar to GOS but calculated within the kernel instead of within grains [24–26]. As described in the above references, high and low dislocation densities were appropriately distinguished by values of KAM ≥ 1° and KAM ≤ 1°, respectively. Compared with the GOS and KAM (**Figs. 4.6** and **4.8**), the high dislocation density was mostly observed at the sub-grain boundaries, which can be attributed to dynamic recovery. Subsequently, CDRX occurred by dynamic recovery within these sub-grains. **Fig. 4.9** shows the fraction of dislocation density within an Al layer. During thermal shock testing, the fraction of dislocation density is higher than that of the thermal exposure test with increasing test period, which will be further discussed in section 4.4.2.

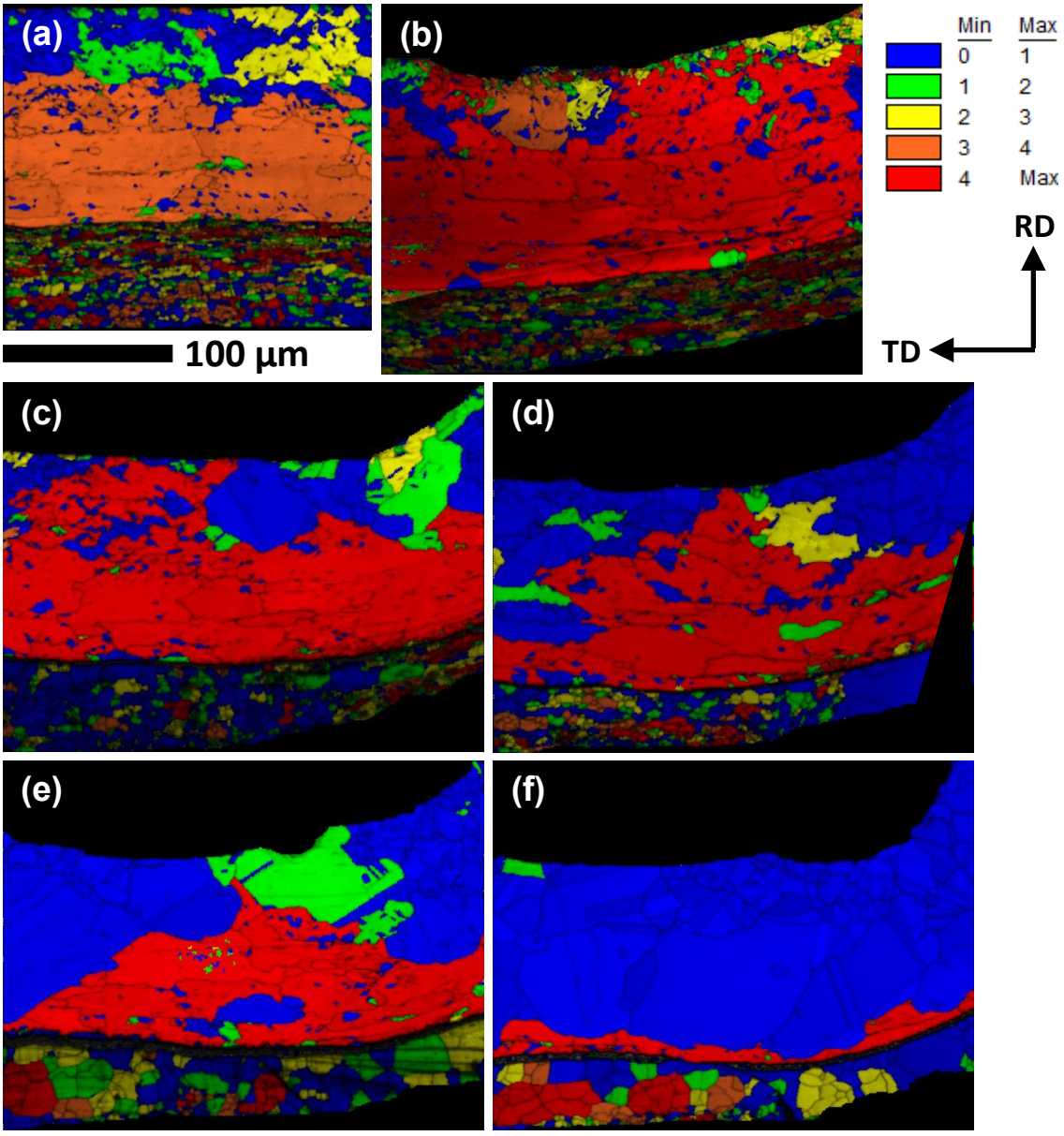

Fig. 4.6 Grain orientation spread (GOS) maps showing the CDRX and DDRX regions of cold rolled Cu/Al clad ribbons during harsh tests: (a) starting material, (b) as-bonded specimen, thermal exposed at 200 °C for (c) 1000 h and (d) 2000 h, thermal shocked at -40/250 °C for (e)1000 cycles and (f) 2000 cycles. A GOS value of 3° was determined to be appropriate for distinguishing between CDRX and DDRX microstructures there are indicated GOS ≥ 3° (orange, and red) and GOS ≤ 3° (blue, green, and yellow) on the GOS map, respectively. The key for the value of GOS is shown at the top right corner.

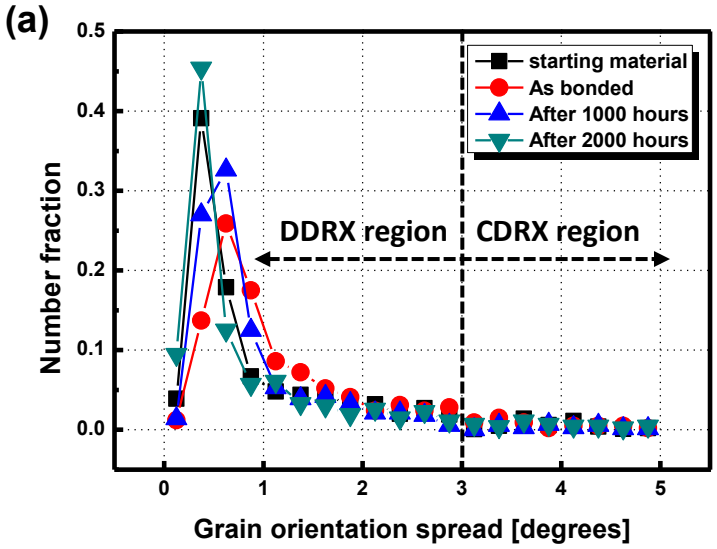

	Starting material	As-bonded	After 1000 h	After 2000 h
$\theta \geq 3^{o}$	35.9 %	35.3 %	14.5 %	24.4 %

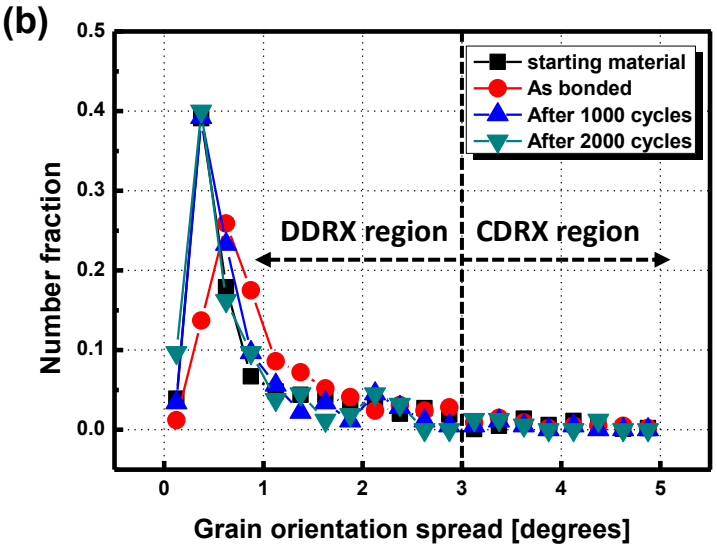

	Starting material	As-bonded	After 1000 cycles	After 2000 cycles
$\theta \geq 3^{o}$	35.9 %	35.3 %	19.6 %	33.6 %

Fig. 4.7 Diagrams of frequency depending on the GOS analysis of each harsh test. The fraction of the CDRX region is indicated at the bottom of each diagram: (a) thermal exposure test and (b) thermal shock test.

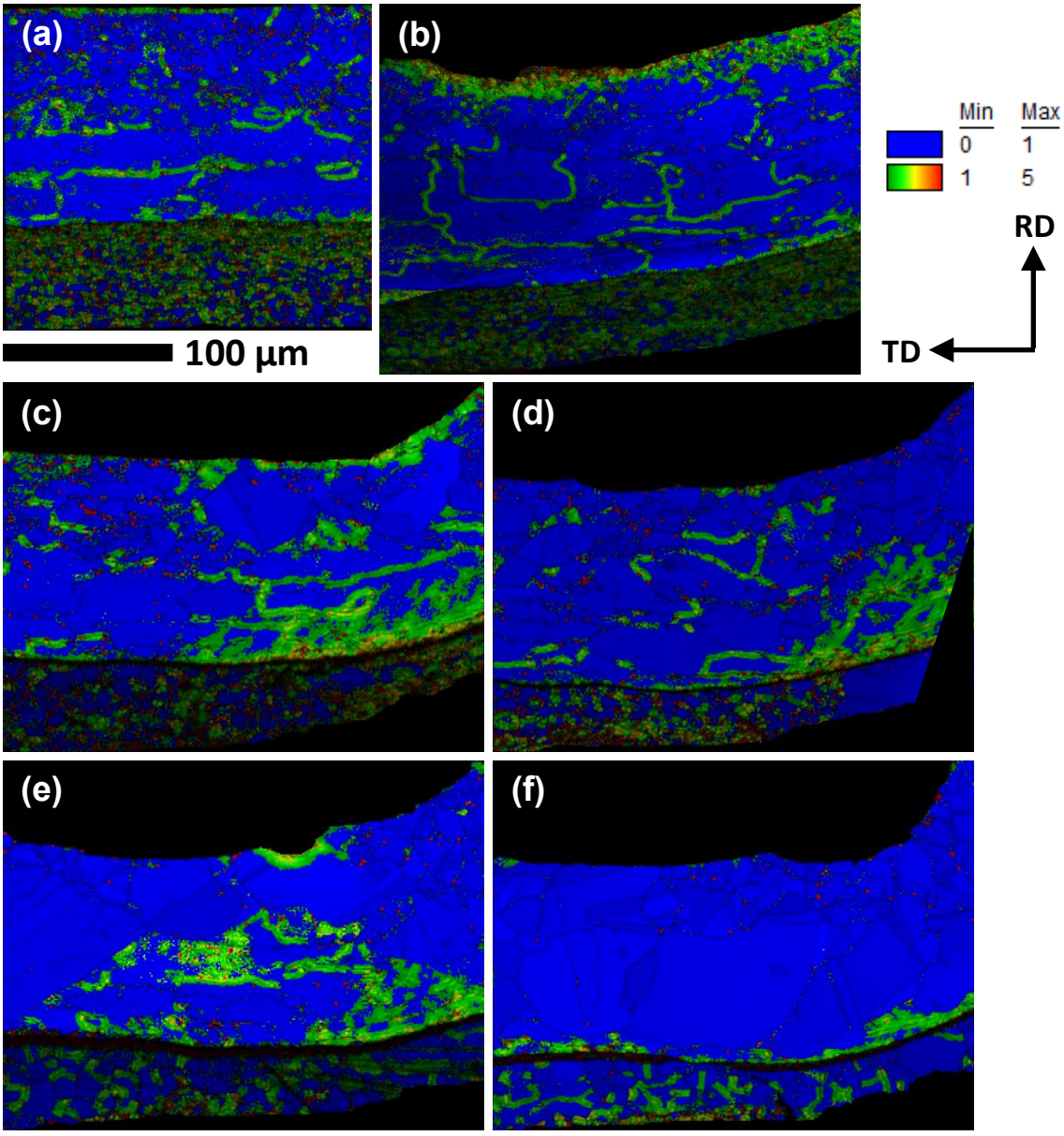

Fig. 4.8 Kernel average misorientation (KAM) maps showing the high and low dislocation densities of cold-rolled Cu/Al clad ribbons during the harsh tests: (a) starting material, (b) as-bonded specimen, thermally exposed at 200 °C for (c) 1000 h and (d) 2000 h, thermal shocked at -40/250 °C for (e) 1000 cycles and (f) 2000 cycles. The high dislocation density was indicated by a KAM value above 1°, and below 1° is low dislocation density. The key for the value of KAM is shown at the top right corner.

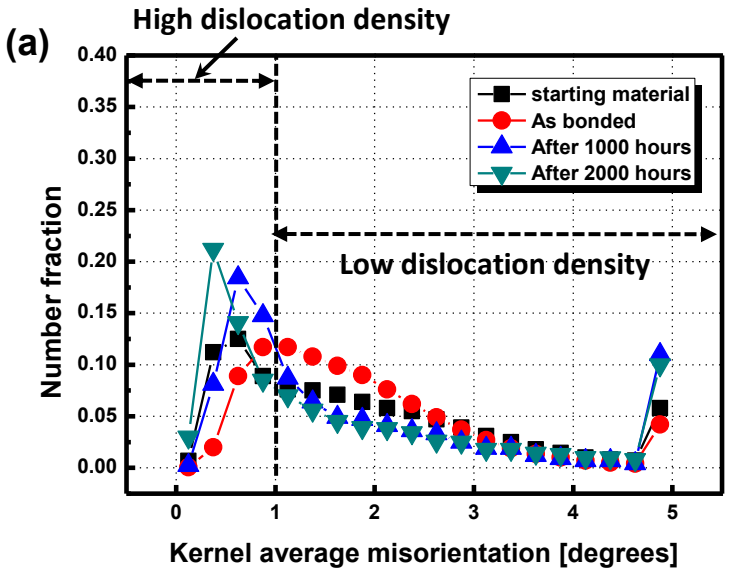

	Starting material	As-bonded	After 1000 h	After 2000 h
$\theta \leq 1^{o}$	40.8 %	34.4 %	50.2 %	53.8 %

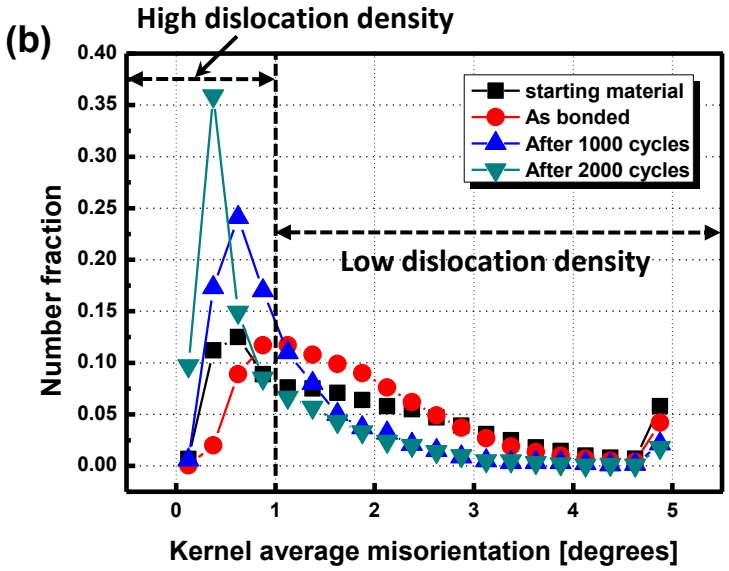

	Starting material	As-bonded	After 1000 cycles	After 2000 cycles
$\theta \leq 1^{o}$	40.8 %	34.4 %	69.9 %	75.7 %

Fig. 4.9 Diagrams of frequency depending on the KAM analysis in the harsh tests. The number fraction of dislocation density is indicated at the bottom of each diagram for the (a) thermal exposure test and (b) thermal shock test.

4.3.3 Transition of the texture

The textural transitions are apparently different between the as-received sample and the ultrasonic bonded one in a harsh environment. Cube{001}⟨100⟩, G{011}⟨100⟩, B{011}⟨211⟩, C{112}⟨111⟩, D{44 11}⟨11 11 8⟩, S{123}⟨634⟩, Y{111}⟨112⟩, and P{011}⟨8 11 11⟩ texture components were observed in the Al layer. B, C, D, and S texture components were formed by the rolling process in the bonded zone, which are typical deformation textures in the FCC structure. However, Y and P texture components were formed by the lift-up procedure in the non-bonded zone, which are plastic deformation textures such as torsion [27, 28], tension [29, 30], rolling [31–33], and deep drawing [34, 35].

Fig. 4.10 shows the band contrast overlaid with inverse pole figure maps during each harsh test. The textural transition was analyzed by PFs and ODFs based on the combination textures. Combined PFs and ODFs are shown in **Figs. 4.11b–e** and **4.12b–e** as cold-rolled, as-bonded, thermal exposure, and thermal shock specimens, respectively. **Figs. 4.11a** and **4.12a** show the most common textures and orientations of the FCC structure. As observed in **Fig. 4.11**, the transition tendency of combined PFs were revealed differently by each of the bonded (ultrasonic oscillation) and non-bonded (lift-up part) zones, respectively. B and S orientations predominated along the β-fiber in the bonded zone within the Al layer, as observed in **Figs. 4.12b–e**. In the non-bonded zone, Y and P orientations were predominated by lift-up forming procedure along the β_D-fiber.

In the bonded zone during the thermal exposure test, the main orientation transition was developed along the α-fiber (G-B) and the β-fiber (B-S-C/D) until 2000 h, as observed in **Fig. 4.12d**. In the non-bonded zone, plastic deformed Y and P orientations were developed along the β_D-fiber. During thermal shock test, in the bonded zone, B orientation was mainly developed along the β-fiber until 1000 cycles, as observed in **Fig. 4.12e**. Subsequently, the B orientation became weak upon increasing the number of cycles. In the non-bonded zone, after 1000 cycles, the P orientation was still maintained, and rotated cube orientation increased with increasing test period. However, the intensity of the rotated cube became

weaker than that of the P orientation. Subsequently, the intensity of the rotated cube became strong, and the P orientation does not exist anymore at 2000 cycles.

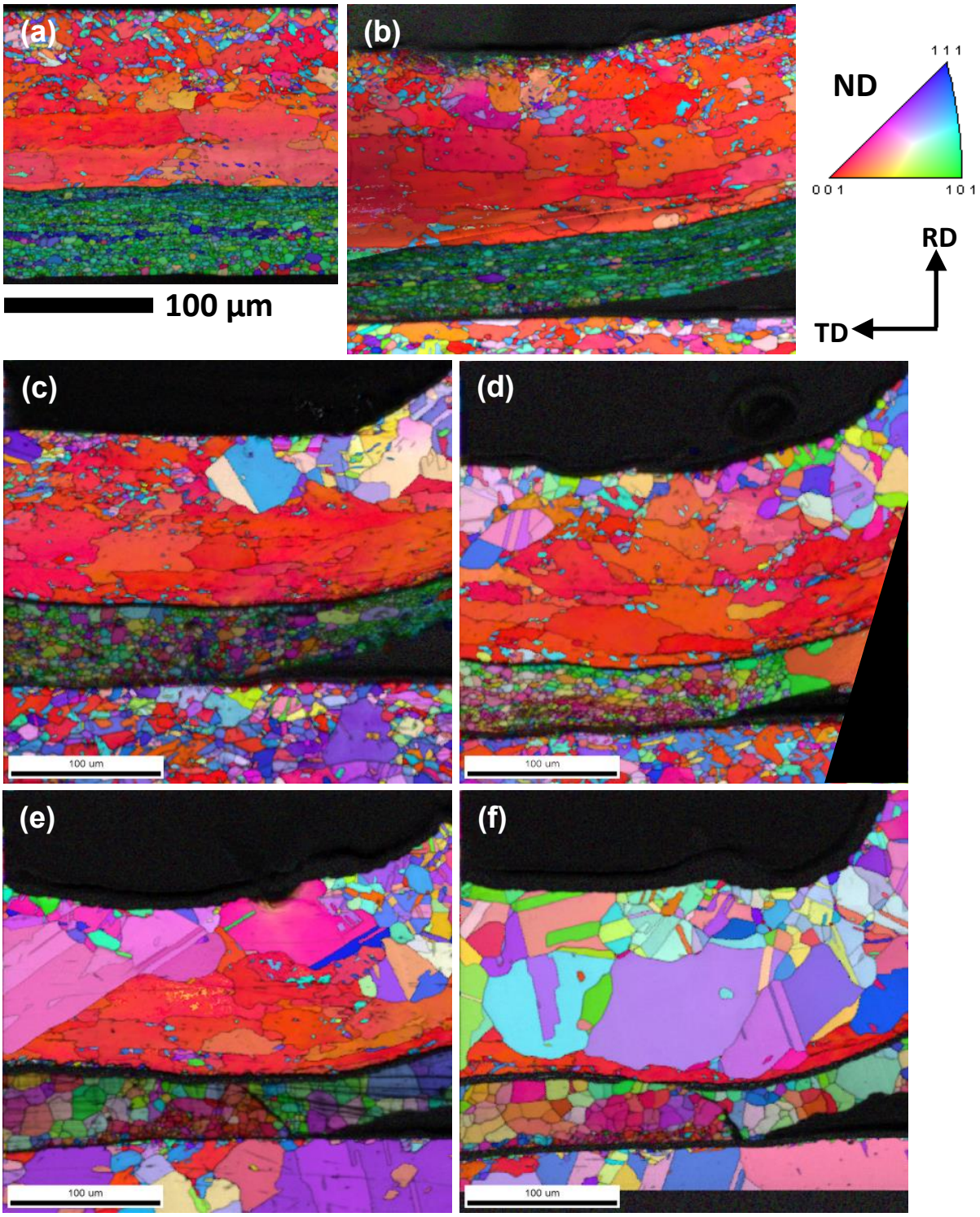

Fig. 4.10 Band contrast (BC) overlaid with inverse pole figure (IPF) maps, showing the evolution of the microstructure during harsh tests: (a) starting material, (b) as-bonded specimen after ultrasonic bonding, thermally exposed for (c) 1000 h and (d) 2000 h and thermally shocked for (e) 1000 cycles and (f) 2000 cycles. The legend for the IPF maps and directions is shown at the top right corner.

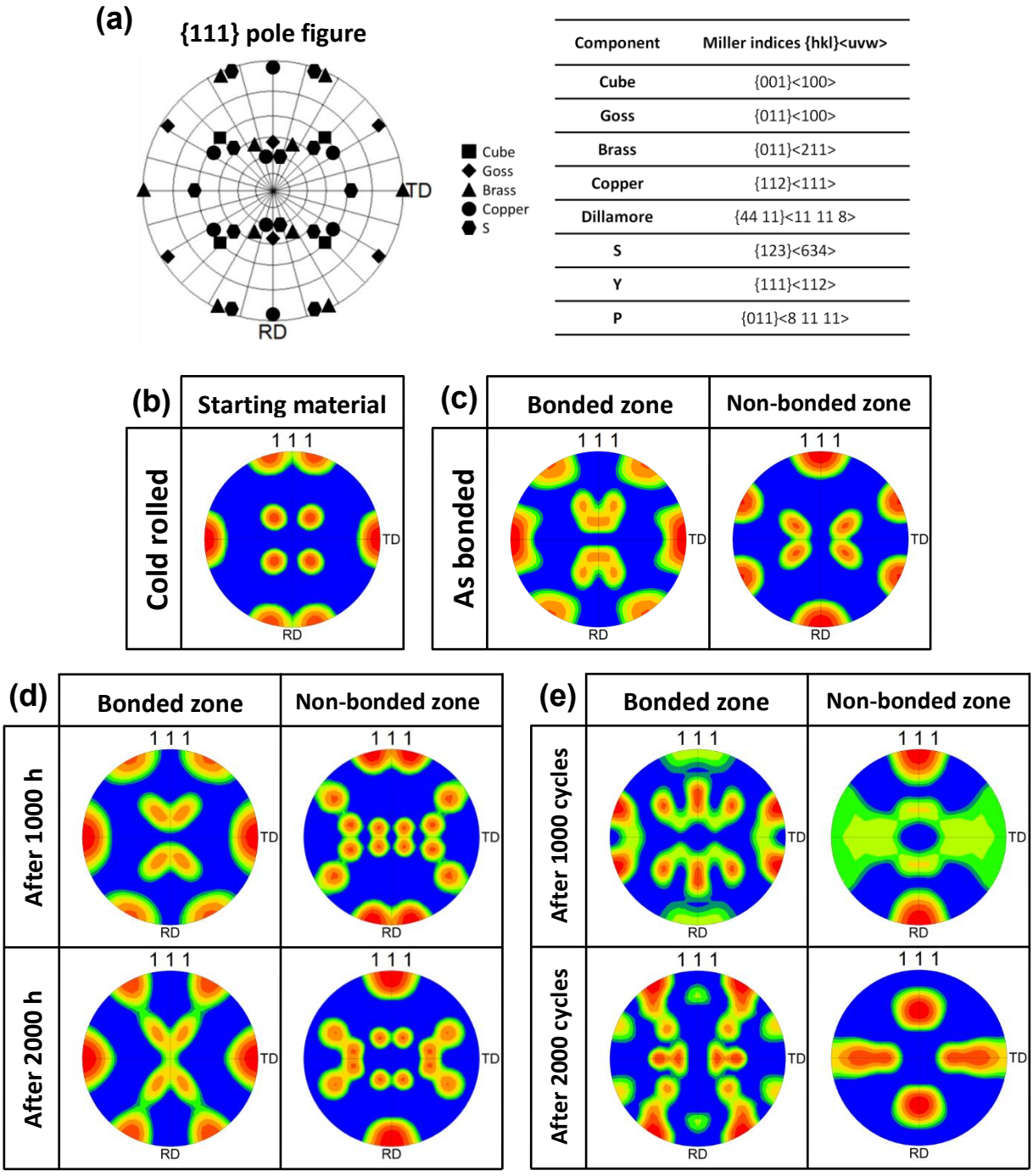

Component	Miller indices {hkl}<uvw>
Cube	{001}<100>
Goss	{011}<100>
Brass	{011}<211>
Copper	{112}<111>
Dillamore	{44 11}<11 11 8>
S	{123}<634>
Y	{111}<112>
P	{011}<8 11 11>

Fig. 4.11 (a) Pole figures (PFs) plotted for {111}, showing ideal cube, Goss, brass, copper, Dillamore, and S components. Contour diagram of combined PFs between the bonded zone and non-bonded zone, which show the variation of combined textures as a function of the harsh tests. (b) Starting material specimen, (c) as-bonded specimen, (d) thermally exposed specimen at 200 °C, and (e) thermally shocked specimen at -40/250 °C.

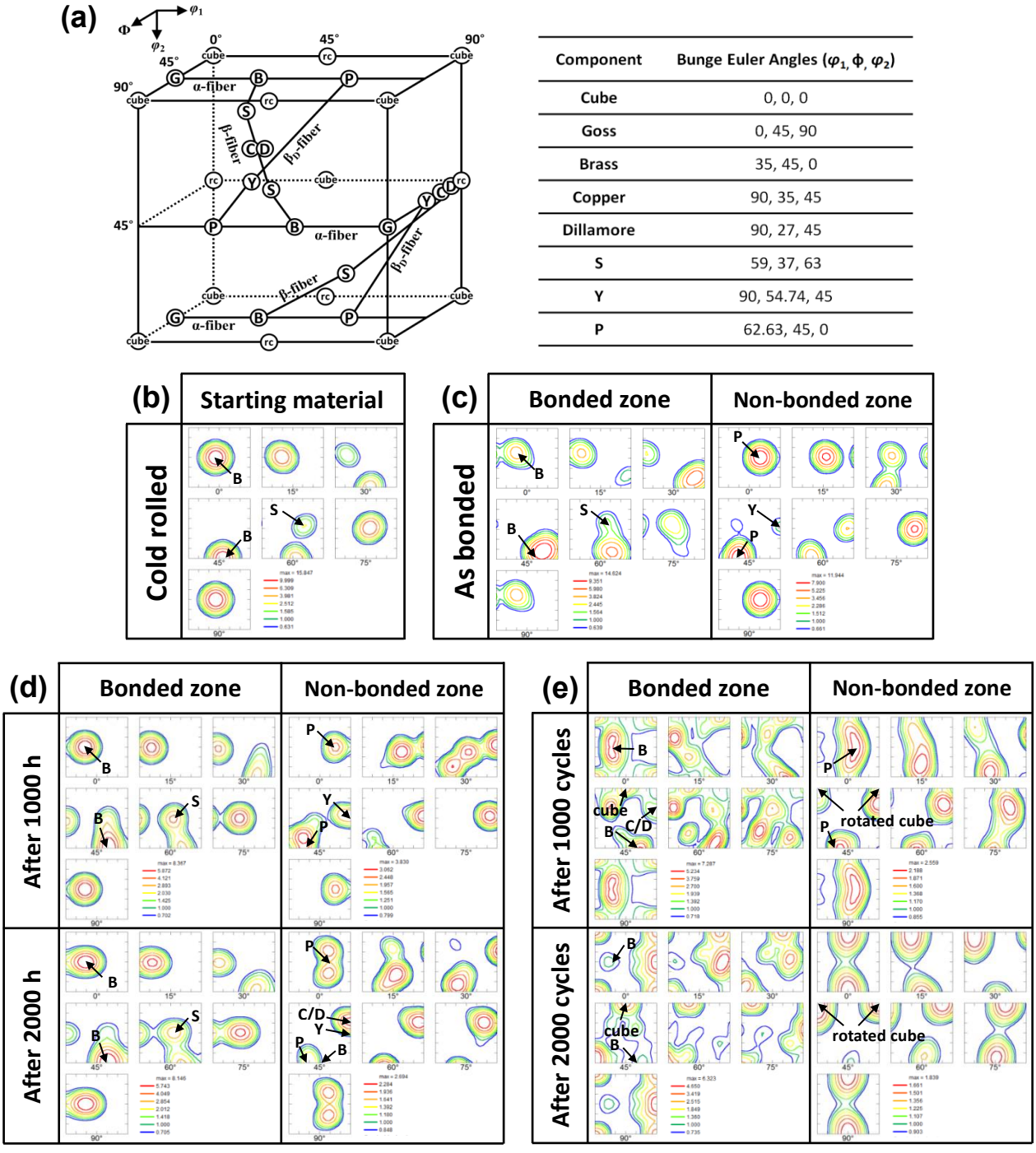

Component	Bunge Euler Angles (φ_1, ϕ, φ_2)
Cube	0, 0, 0
Goss	0, 45, 90
Brass	35, 45, 0
Copper	90, 35, 45
Dillamore	90, 27, 45
S	59, 37, 63
Y	90, 54.74, 45
P	62.63, 45, 0

Fig. 4.12 (a) Orientation distribution functions (ODFs) plotted for face-centered-cubic structure, showing ideal α-fiber, β-fiber, and plastic deformed β_D-fiber. Contour diagram of ODFs between bonded zone and non-bonded zone, which show the variation of orientations as a function of the harsh tests: (b) starting material specimen, (c) as-bonded specimen, (d) thermally exposed specimen at 200 °C, and (e) thermally shocked specimen at -40/250 °C. The intensity lines in the texture are represented by a constant section of φ_2 ($\Delta\varphi_2 = 15°$) through the adjective Euler angle space ($0° \leq \{\varphi_1, \phi, \varphi_2\} \leq 90°$).

4.4 Discussion

4.4.1 Grain coarsening and heel crack growth

The formation of heel crack and its growth is one of the main concerns in determining the reliability of wire/ribbon bonds. Thus, the heel crack growth of the cold-rolled Cu/Al clad ribbons in the current harsh test is discussed hereafter, especially in terms of Al grain coarsening.

The heel cracks were formed at the boundary between the bonded and non-bonded zones. In the harsh tests, these heel cracks propagated along the coarsened grain boundaries deep into the Al layer. After 1000 h of thermal exposure, the average grain size of the Al layer was smaller than those of the starting ribbons and the as-bonded specimens. Subsequently, the average grain size was coarsened by 0.7 μm until 2000 h as shown in **Table 4.2**, which clearly demonstrates the occurrence of CDRX. Any heel cracks observed in the specimens of the staring material, in the as-bonded, and in the 1000 h exposed one are shown in **Figs. 4.3a–c**. During the thermal shock test, the average grain size of the Al layer continuously increased with increasing test period. CDRX discontinuously occurs in the recrystallized grains, which are transformed into new sub-grains by dynamic recovery. Finally, formed sub-grains are gradually coarsened by CDRX, for which the sub-grain growth rate was faster than grain boundary migration by DDRX. Sub-grain boundaries are formed as low-angle grain boundaries within the recrystallized grains, which are transformed into new high-angle grain boundaries. In thermal shock tests up to the highest temperature 250 °C, grain coarsening was mainly induced by CDRX. Thus, heel cracks propagated by grain coarsening, which can be clearly observed in the boundary between the bonded and non-bonded zones, as observed in the specimens after heat-exposure of 2000 h after heat-cycles of 1000 cycles and 2000 cycles, as shown in **Figs. 4.3d–f**.

4.4.2 Recrystallization mechanism

The stacking fault energy is one of the important parameters to understand the mechanism of DRX. DDRX and CDRX usually correspond to low- and high-stacking-fault-energy metals, respectively.

Additionally, some recent works have provided a new verification of the DRX mechanism, for which a transition occurs from DDRX to CDRX for high-purity Al [36, 37]. Generally, DDRX can be regarded as the unique recrystallization mechanism for high-purity face-centered-cubic (FCC) metals [10, 11]. Grain boundary migration occurs by DDRX, for which the velocity is faster than that of sub-grain growth by CDRX. In particular, the reduction of the average grain size is likely accompanied by grain boundary migration, which indicates the local dislocation density almost decreases to zero. In contrast, CDRX occurs by dynamic recovery, which is formed in sub-grains and high-dislocation density regions [12, 13]. Sub-grain boundaries distribute as low-angle grain boundaries within the recrystallized grains, which transforms into new high-angle grain boundaries.

Microstructural evolution of DRX is also affected by the forming post-process and high-temperature deformation [38–41]. During forming post-processes such as cold-rolling and ultrasonic bonding, CDRX (LAGBs) and DDRX (HAGBs) regions are formed together by dense and sparse dislocations, respectively. The CDRX region was raised by dynamic recovery, which led to sub-grain formation with an increasing harsh test period. The DDRX was partially formed after cold rolling and ultrasonic bonding and transformed into the CDRX. This phenomenon is analogously observed during thermal exposure and shock tests. However, severe CDRX transformation occurred by thermal shock test at the highest temperature. Under the most severe heat exposure at 200 °C and the most severe thermal shock up to 250 °C, CDRX easily occurred by low stress flow and was partially restored by dynamic recovery with respect to the high dislocation density. Consequently, the restoration of the elastic strain occurred within recrystallized grains by CDRX, which microstructural evolution occurs through (1) the formation of LAGBs as an outcome of dynamic recovery within the sub-grain boundaries, (2) the revolution of sub-grain boundaries into HAGBs, (3) dislocation of the recrystallized grain boundaries that consumes sub-grain boundaries locally in subsequent grain coarsening, (4) heel crack that propagates along coarsened grain boundaries. This procedure of heel crack propagation results demonstrate significantly with regard to recrystallization mechanism and grain coarsening in harsh environment.

4.4.3 Texture transition within recrystallized grains

Typical texture components in FCC metals such as Al and Cu, B, C, D, and S texture components correspond to deformed microstructure, and cube and G texture components correspond to a recrystallized microstructure [14–16]. The dominant texture components of the microstructure were different in each region of the bonded zone and the non-bonded zone within the Al layer. During the cold-rolling process, the cube texture component developed a B texture component by deformation as the volume was reduced by 50 %. During the ultrasonic bonding process, the deformed B texture component still existed within an Al layer, and a particular G texture component was partially formed in the recrystallized grains. The G texture component was generated by severe ultrasonic oscillation during the bonding process. As observed in **Fig. 4.12c**, the intensity of the B orientation decreases from 15.84 (cold rolled) to 14.62 (as-bonded). For the as-bonded specimen, the intensity of the G orientation is 1.56. However, the P orientation during the lift-up procedure was dominated by plastic deformation in the non-bonded zone, the intensity of which was 11.94. Stable orientations were developed from Y to P orientations along the β_D-fiber during plastic deformation [15, 42].

During the thermal exposure test, the α-fiber (G-B orientation) and β-fiber (B-S-C/D orientation) strongly appeared in the bonded zone regardless of the test period. However, the β_D-fiber (Y-P orientation) became predominant in the non-bonded zone even though the highest intensity value decreased from 3.83 at 1000 h to 2.69 at 2000 h. In particular, β-fiber additionally appeared after 2000 h; however, its intensity was lower than that of β_D-fiber. The β_D-fiber transformed to another orientation along the ϕ axis. Subsequently, the deformed β_D-fiber transformed to the rotated cube orientation by increasing the CDRX region during thermal exposure at 200 °C.

During the thermal shock test, in the bonded zone, the intensity of the B orientation decreased from 7.28 at 1000 cycles to 1.36 at 2000 cycles. However, the cube orientation strongly appeared upon increasing the number of cycles, the intensity of which increased from 2.7 at 1000 cycles to 3.41 at 2000 cycles, as observed in **Fig. 4.12e**. The deformed B texture component continuously transformed to the

cube texture component by CDRX. In the non-bonded zone, P and rotated cube texture components appeared together after 1000 cycles with intensity values of 2.56 and 1.37, respectively. However, the P texture component disappeared and rotated cube texture component appeared with the highest intensity of 1.84 at 2000 cycles. During the thermal shock test, the plastically deformed P texture component transformed to the rotated cube texture component. The rotated cube orientation represents the shear texture component [43–45]. Consequently, different intensity values indicated each process (ultrasonic oscillation and lift-up) and harsh environment (thermal exposure and shock tests), of which applicable textures affect the mechanical stability of Cu/Al clad ribbon wiring.

4.5 Conclusions

Cold-rolled Cu/Al clad ribbons were bonded on ENIG-finished Cu substrates using the ultrasonic bonding process. The microstructural evolution and textural transition were investigated on cold-rolled, ultrasonic-bonded, thermal-exposed, and thermal-shocked ribbons. The textural transition of the microstructure differed in each specimen. In the bonded zone after the thermal exposure test, the α-fiber and β-fiber textures were dominant, and B, C, D, and S texture components also appeared. However, the β_D-fiber texture became dominant in the non-bonded zone, and the Y and P texture components appeared as a result of plastic deformation. After severe thermal shock, a cube appeared in the bonded zone, and a rotation cube appeared in the non-bonded zone. DDRX partially occurred both by cold rolling and by ultrasonic bonding. Sub-grains were formed by dynamic recovery within an Al layer, which transformed into new grains by CDRX. Grain coarsening occurred with an increasing rate of CDRX at the highest temperature. Based on the current results, grain coarsening by CDRX was observed to be the main mechanism of heel crack propagation.

References

[1] Y. Celnikier, L. Benabou, L. Dupont, G. Coquery, Investigation of the heel crack mechanism in Al connections for power electronics modules, Microelectronics Reliability 51 (2011) 965–974.

[2] M. Li, H. Ji, C. Wang, H.S. Bang, H.S. Bang, Interdiffusion of Al–Ni system enhanced by ultrasonic vibration at ambient temperature, Ultrasonics 45 (2006) 61–65.

[3] X. Liu, G. Lu, Power Chip Interconnection: From Wirebonding to Area Bonding, The International Journal of Microcircuits and Electronic Packaging 23 (2000) 407–413.

[4] M. Ciappa, Selected failure mechanisms of modern power modules, Microelectronics Reliability 42 (2002) 653–667.

[5] Y. Yamada, Y. Takaku, Y. Yagi, I. Nakagawa, T. Atsumi, M. Shirai, I. Ohnuma, K. Ishida, Reliability of wire-bonding and solder joint for high temperature operation of power semiconductor device, Microelectronics Reliability 47 (2007) 2147–2151.

[6] V.K. Astashev, V.I. Babitsky, Ultrasonic cutting as a nonlinear (vibro-impact) process, Ultrasonics 36 (1998) 89–96.

[7] I.E. Gunduz, T. Ando, E. Shattuck, P.Y. Wong, C.C. Doumanidis, Enhanced diffusion and phase transformations during ultrasonic welding of zinc and aluminum, Scripta Materialia 52 (2005) 939–943.

[8] H. Medjahed, P.E. Vidal, B. Nogarede, Thermo-mechanical stress of bonded wires used in high power modules with alternating and direct current modes, Microelectronics Reliability 52 (2012) 1099–1104.

[9] F.J. Humphreys, M. Hatherly, Recrystallization and related annealing phenomena, second ed., Elsevier, Kidlington, 2004.

[10] S. Gourdet, F. Montheillet, An experimental study of the recrystallization mechanism during hot deformation of aluminium, Materials Science and Engineering A 283 (2000) 274–288.

[11] H.J. Mcqueen, Development of dynamic recrystallization theory, Materials Science and Engineering A 387 (2004) 203–208.

[12] H. Yamagata, Multipeak stress oscillations of five-nine-purity aluminum during a hot compression test, Scripta Metallurgica et Materialia 27 (1992) 201–203.

[13] H. Yamagata, Dynamic recrystallization and dynamic recovery in pure aluminum at 583 K, Acta Metallurgica et Materialia 43 (1995) 723–729.

[14] M. Kuroda, Effects of texture on mechanical properties of aluminum alloy sheets and texture optimization strategy, AIP Conference Proceedings 778 (2005) 445–450.

[15] S.H. Choi, J.H. Cho, K.H. Oh, K. Chung, F. Barlat, Texture evolution of FCC sheet metals during deep drawing process, International Journal of Mechanical Sciences 42 (2000) 1571–1592.

[16] J. Hirsch, K. Lucke, Mechanical of deformation and development of rolling textures in polycrystalline F.C.C. metal–I. description of rolling texture development in homogeneous CuZn alloys, Acta Metallurgica 36 (1988) 2863–2882.

[17] F.J. Humphreys, Grain and subgrain characterisation by electron backscatter diffraction, Journal of Materials Science 36 (2001) 3833–3854.

[18] K.P. Mingard, B. Roebuck, E.G. Bennett, M.G. Gee, H. Nordenstrom, G. Sweetman, P. Chan, Comparison of EBSD and conventional methods of grain size measurement of hardmetals, International Journal of Refractory Metals and Hard Materials 27 (2009) 213–223.

[19] K.P. Mingard, B. Roebuck, E.G. Bennett, M. Thomas, B.P. Wynne, E.J. Palmiere, Grain size measurement by EBSD in complex hot deformed metal alloy microstructures, Journal of Microscopy 227 (2007) 298–308.

[20] J. Wheeler, D.J. Prior, Z. Jiang, R. Spiess, P.W. Trimby, The petrological significance of misorientations between grains, Contributions to Mineralogy and Petrology 141 (2001) 109–124.

[21] K. Kunze, S.I. Wright, B.L. Adams, D.J. Dingley, Advances in automatic EBSP single orientation measurements, Textures and Microstructures 20 (1993) 41–54.

[22] S.I. Wright, M.M. Nowell, D.P. Field, A review of strain analysis using electron backscatter diffraction, Microscopy and Microanalysis 17 (2011) 316–329.

[23] M.H. Alvi, S.W. Cheong, J.P. Suni, H. Weiland, A.D. Rollett, Cube texture in hot-rolled aluminum alloy 1050 (AA1050)–nucleation and growth behavior, Acta Materialia 56 (2008) 3098–3108.

[24] S. Zaefferer, P. Romano, F. Friedel, EBSD as a tool to identify and quantify bainite and ferrite in low-alloyed Al-TRIP steels, Journal of Microscopy 230 (2008) 499–508.

[25] L. Bracke, K. Verbeken, L. Kestens, J. Penning, Microstructure and texture evolution during cold rolling and annealing of a high Mn TWIP steel, Acta Materialia 57 (2009) 1512–1524.

[26] E.J. Chun, H. Do, S. Kim, D.G. Nam, Y.H. Park, N. Kang, Effect of nanocarbides and interphase hardness deviation on stretch-flangeability in 998 MPa hot-rolled steels, Materials Chemistry and Physics 140 (2013) 307–315.

[27] K.W. Neale, L.S. Toth, J.J. Jonas, Laser strain shear and torsion of rate-sensitive FCC polycrystals, International Journal of Plasticity 6 (1990) 45–61.

[28] L.S. Toth, J.J. Jonas, P. Gilormini, B. Bacroix, Length changes during free end torsion: a rate sensitive analysis, International Journal of Plasticity 6 (1990) 83–108.

[29] R. Becker, J.F. Butler, J.H. Hu, L.A. Lalli, Analysis of an aluminum single crystal with unstable initial orientation (001) [110] in channel die compression, Metallurgial Transactions A 22 (1991) 45–58.

[30] S.H. Choi, J.H. Cho, F. Barlat, K. Chung, J.W. Kwon, K.H. Oh, Prediction of yield surfaces of textured sheet metals, Metallurgical and Materials Transactions A 30 (1999) 377–386.

[31] J. Hirsch, K. Lucke, Mechanism of deformation and development of rolling textures in polycrystalline F.C.C. metals–simulation and interpretation of experiments on the basis of taylor-type theories, Acta Metallurgica 36 (1988) 2883–2904.

[32] Y. Zhou, L.S. Toth, K.W. Neale, On the stability of the ideal orientations of rolling textures for F.C.C polycrystals, Acta Metallurgica 40 (1992) 3179–3193.

[33] C.H. Choi, J.W. Kwon, K.H. Oh, D.N. Lee, Analysis of deformation texture inhomogeneity and stability condition of shear components in f.c.c metals, Acta Materialia 45 (1997) 5119–5128.

[34] J.R. Hirsch, T.J. Rickert, Texture evolution during deep drawing in aluminum sheet, Materials Science Forum 157–162 (1994) 1979–1984.

[35] Y. Zhou, J.J. Jonas, K.W. Neale, Behaviour of initial texture components during the plane strain drawing of F.C.C sheet metals, Acta Materialia 44 (1996) 607–619.

[36] H. Yamagata, Y. Ohuchida, N. Saito, M. Otsuka, Nucleation of new grains during discontinuous dynamic recrystallization of 99.998 mass% aluminum at 453K, Scripta Materialia 45 (2011) 1055–1061.

[37] F. Montheillet, J. LeCoze, Influence of purity on the dynamic recrystallization of metals and alloys, Journal of physica status solidi (a) 189 (2002) 51–58.

[38] D. Ponge, M. Bredehoft, G. Gottstein, Dynamic recrystallization in high purity aluminum, Scripta Materialia 37 (1997) 1769–1775.

[39] S. Gourdet, F. Montheillet, A model of continuous dynamic recrystallization, Acta Materialia 51 (2003) 2685–2699.

[40] E. Mariani, J. Mecklenburgh, J. Wheeler, J.D. Prior, F. Heidelbach, Microstructure evolution and recrystallization during creep of MgO single crystals, Acta Materialia 57 (2009) 1886–1898.

[41] R.D. Doherty, D.A. Hughes, F.J. Humphreys, J.J. Jonas, D.J. Jensen, M.E. Kassner, W.E. King, T.R. McNelley, H.J. McQueen, A.D. Rollett, Current issues in recrystallization: a review, Materials Science and Engineering A 238 (1997) 219–274.

[42] P.J. Hurley, F.J. Humphreys, The application of EBSD to the study of substructural development in a cold rolled single-phase aluminium alloy, Acta Materialia 51 (2003) 1087–1102.

[43] R. Jamaati, M.R. Toroghinejad, M. Hoseini, J.A. Szpunar, Development of texture during ARB in metal matrix composite, Materials Science and Technology 28 (2012) 406–410.

[44] L. Su, C. Lu, A.A. Gazder, A.A. Saleh, G. Deng, K. Tieu, H. Li, Shear texture gradient in AA6061 aluminum alloy processed by accumulative roll bonding with high roll roughness, Journal of Alloys and Compounds 594 (2014) 12–22.

[45] Y. Saito, N. Tsuji, H. Utsunomiya, T. Sakai, R.G. Hong, Ultra-fine grained bulk aluminum produced by accumulative roll-bonding (ARB) process, Scripta Materialia 39 (1998) 1221–1227.

Chapter 5

Conclusions

Chapter 5
Conclusions

In this thesis, high-temperature reliability of metal ribbon wirings with ultrasonic bonding was investigated for the application of high-power electronic devices. The Al and Cu/Al clad ribbons were selected to wiring materials. The optimized ultrasonic bonding parameters of Al and Cu/Al clad ribbons were established by verifying of the ultrasound transmission and reflection. The mechanical stabilities were compared by pull strengths depending on each harsh environmental test period. Based on the results of both ribbon wirings, the joint stability of Cu/Al clad ribbons is always higher than that of Al ribbons.

Chapter 1 offers a literature survey that described the research trends and issues for ultrasonic wire bonding in power electronic devices. Using ribbons replacing typical wires, it can be expected to improve the joint reliability under high-current/high-temperature because ribbons have a large cross sectional area. This thesis described that the thermal and mechanical superiority of metal ribbon wirings.

In Chapter 2, 4N Al ribbons were applied in a new wiring structure instead of typical string wires because the use of rectangular ribbons is expected to improve the high-temperature degradation as the large area bonding. However, high bonding parameters such as ultrasonic power/frequency and bonding pressure/time have to require to successful manufacturing of ribbon wiring. Therefore, the ultrasonic ribbon bonding parameters were optimized to obtain the excellent bondability by pull test at each bonding condition.

In Chapter 3, a Cu/Al clad ribbon was additionally adopted in wiring material to achieve high thermal/electrical performance together with successful manufacturing. The thermo-mechanical stability of Al ribbons have compared to Cu/Al clad ribbons in a practical interconnect bonding structure under harsh environmental tests such as thermal exposure to 200 °C and thermal shock cycling at -40/250 °C. After the optimizing the ultrasonic ribbon bonding parameters, the mechanical strength of Cu/Al clad ribbons was

always higher than that of Al ribbons independent to the test conditions. Hence, the thermal and mechanical stability of ribbon wiring structures consist of Cu/Al clad ribbon is superior to those of Al.

In Chapter 4, mechanical degradation mechanism of Cu/Al clad ribbons was investigated by analysis of microstructural evolution. Wiring failures were occurred by grain coarsening, leading to heel crack propagation, which is caused by CDRX. Heel cracks were formed at boundaries between the bonded zone and non-bonded zone even in the ultrasonic ribbon bonding process. During the harsh tests, the heel cracks propagated deep into the Al layer along recrystallized grain boundaries.

In Chapter 5, this dissertation concluded that use of metal ribbon wirings can be expected to improve the thermal and mechanical interconnection stability. In particular, the mechanical stability of Cu/Al clad ribbon wirings was more superior compared to Al ribbons. These findings would contribute to secure a long-term interconnection reliability of high-power electronics packaging.

List of publications

A. Papers

1. Semin Park, Shijo Nagao, Tohru Sugahara, and Katsuaki Suganuma, "Mechanical stabilities of ultrasonic Al ribbon bonding on electroless nickel immersion gold finished Cu substrates", Japanese Journal of Applied Physics 53 (2014) 04EP06.

2. Semin Park, Shijo Nagao, Tohru Sugahara, and Katsuaki Suganuma, "Heel crack propagation mechanism of cold-rolled Cu/Al clad ribbon bonding in harsh environment", Journal of Materials Science: Materials in Electronics, xx (2015) xxx. (In press)

3. Semin Park, Shijo Nagao, Tohru Sugahara, Emi Yokoi, and Katsuaki Suganuma, "Thermal and mechanical superiority of Cu/Al clad ribbon wiring with ultrasonic bonding for high power electronic devices", Microelectronics reliability, xx (2015) xxx. (Under review)

B. Proceedings and Presentations

1. Semin Park, Shijo Nagao, Tohru Sugahara, and Katsuaki Suganuma, "Heavy Ribbon Wire Bonding for Advanced Power Module Packages", 45th International Conference on Solid State Devices and Materials (SSDM 2013), Fukuoka, Japan, September 24-27 (2013).

2. Semin Park, Shijo Nagao, and Katsuaki Suganuma, "High Temperature Compatibility of Interface between Al Ribbon and Au finished DBC Substrate", 8th International Conference on Integrated Power Electronics Systems (CIPS 2014), Nuremberg, Germany, February 25-27 (2014).

3. Semin Park, Shijo Nagao, Tohru Sugahara, Emi Yokoi, Osami Iizuka, and Katsuaki Suganuma, "Ultrasonic bonding of Cu/Al clad ribbon interconnections in power electronic modules", 67th International Institute of Welding Annual Assembly & International Conference (IIW 2014), Seoul, Korea, July 13-18 (2014).

4. Katsuaki Suganuma, Jingting Jiu, Shunsuke Kaga, Tohru Sugahara, Semin Park, Sungwon Park, Chulmin Oh, and Shijo Nagao, "Zero Stress Die-Attach for Wide Band Gap Semiconductor Power Devices", 47th International Symposium on Microelectronics (IMAPS 2014), San Diego, USA, October 13-16 (2014).

5. Katsuaki Suganuma, Shijo Nagao, Tohru Sugahara, Chulmin Oh, Hao Zhang, Shunsuke Kaga, and Semin Park, "Silver Sinter Joining and New Thin Film bonding for WBG die-attach", 2nd International conference on Nanojoining and Microjoining (NMJ 2014), Emmetten, Switzerland, December 7-10 (2014).

6. Semin Park, Shijo Nagao, Tohru Sugahara, Emi Yokoi, and Katsuaki Suganuma, "High-temperature reliability of Cu/Al clad ribbon wiring for WBG semiconductor power devices", 25th Microelectronics Symposium (MES 2015), Osaka, Japan, September 3-4 (2015).

Acknowledgements

The author would like to express my gratitude to all those who made this dissertation possible. Firstly, I would like to give my special appreciation to my research advisor, Prof. Katsuaki Suganuma at the Institute of Scientific and Industrial Research in Osaka University who provided a motivating, encouraging, and enthusiastic environment during my pursuit of doctoral research. It was his steady support and inspiring guidance that brought this dissertation to its fruition. It was a great pleasure to conduct my work under his mentoring.

I would like to thank Prof. Yoritoshi Minamino at the department of adaptive machining systems in Osaka University and Prof. Keisuke Uenishi at the department of management of industry and technology in Osaka University, for being my committee members and for their invaluable advice and encouraging comment during preparation of this thesis. I am deeply grateful to Prof. Shijo Nagao for his unlimited support on my publication activities and defense. I also would like to thank Prof. Nogi Masaya, Dr. Tohru Sugahara and Dr. Hirotaka Koga for valuable comments.

I wish to express my sincere thanks to Prof. Han-Sur Bang at Chosun University in Korea who is a great mentor for my research life. It was possible to study at Osaka University for his active support and unstinting encouragement. I also would like to thank Dr. Chang-Woo Lee, Dr. Se-Hoon Yoo, and Dr. Jung-Hwan Bang at Korea Institute of Industrial Technology in Korea for invaluable advices with career counseling.

I would like acknowledge my seniors, Dr. Chang-Jae Kim, Dr. Sung-Won Park, Dr. Soichi Sakamoto, Dr. Natsuki Komoda, Dr. Jung-Lae Jo, Dr. Young-Seok Kim, and Dr. Teppei Araki for their technical assistance and kind support during my doctoral course. I warmly thank my colleagues Inui Tetsuji, Zhang Hao, Koga Shunske, Cong Shuren, Jun Wang, Tenkyoku Go, and Sho Akutagawa for friendly help. I would like to thank Emi Yokoi, Kagami, Keiko Suzuki, Midori Fujii, and Satomi Yamawaki for their kind support.

I am deeply grateful to Dr. Min-Su Kim, Dr. Eun-Joon Chun, and Dr. Jong-Uk Park for their warm encouragement and friendly help. I was glad to meet them and will miss the time spent together at Osaka in Japan.

Lastly, I would love to thank my family for endless support and encouragement. Especially, I sincerely express my love and gratitude to my wife Ran-Hee Jung and my son Jang-Oh Park who mean more to me than anything in the world.

Osaka, Japan, 2015

Semin Park